STUDY OF ADULT STEM CELL BEHAVIOR IN THE CRYPTS OF THE SMALL INTESTINE USING ADVANCED *IN VIVO* IMAGING TECHNOLOGY

A Dissertation

Presented to the Faculty of the Graduate School

of Cornell University

In Partial Fulfillment of the Requirements for the Degree of

Doctor of Philosophy

by

Jiahn Choi

August 2018

STUDY OF ADULT STEM CELL BEHAVIOR IN THE CRYPTS OF THE SMALL INTESTINE USING ADVANCED *IN VIVO* IMAGING TECHNOLOGY

Jiahn Choi, Ph.D.

Cornell University 2018

The small intestinal epithelium is continuously replaced by a new cell from the crypts, which makes this organ the fastest regenerative organ in a body. Fast-cycling intestinal stem cells (ISCs) marked with leucine-rich repeat-containing G-protein coupled receptor 5 (Lgr5) are located at the bottom of the crypts and proliferate once every day to provide new cells. Despite the continuous renewal and turnover of the small intestinal epithelium, the intestinal crypt maintains a 'soccer ball-like', alternating pattern of stem and Paneth cells at the base of the crypt. To study the robustness of the alternating pattern, we used intravital two-photon microscopy in mice with fluorescently-labeled Lgr5+ ISCs and precisely perturbed the mosaic pattern with femtosecond laser ablation. The work presented in this dissertation provides a new type of behavior of Lgr5+ ISCs in addition to the proliferation and self-renewal, which is critical to maintain integrity of small intestinal epithelium in homeostasis.

BIOGRAPHICAL SKATCH

Jiahn Choi was born in Daegu, South Korea in 1986. She majored in Oriental Pharmacy at Kyung Hee University, where she started her journey as a researcher. She joined the Pharmacognosy laboratory in her junior year and worked on characterization of a newly invented mass spectrometry method to demonstrate its advantages over a conventional method. She aimed to increase her experience in a broader yet integrated field of study for her graduate studies. Therefore, she subsequently enrolled in a graduate program in Bio and Brain Engineering at the Korea Advanced Institute of Science and Technology (KAIST). For her master's thesis, she developed alternative way to inhibit tumor growth *in vivo* by selective disruption of tumor-associated vasculature using femtosecond laser ablation. The results showed the feasibility of laser ablation as an alternative version of photodynamic therapy. After she complete her master's program in Korea, she decided to study abroad, which led her to enroll in a Master of Engineering program in Biomedical Engineering at Cornell University during Fall 2012. She joined Schaffer-Nishimura Lab in 2012, and under guidance of Prof. Nishimura, she has developed an advanced imaging platform to study stem cell dynamics *in vivo* which allows the study of stem cell behavior at a cellular level. In 2014, she started her Ph.D. program and continued her work on studying the cellular behavior in the stem cell niche after local injury in her doctorate study.

누구보다 이 논문을 기다렸을 사랑하는 나의 할머니께

ACKNOWLEDGMENTS

This dissertation is dedicated to the people who gave me endless support throughout my Ph.D. program in Cornell. It would not be possible to complete this journey without their love, encouragement, and prayers. Although these couple sentences would not be enough to return their support, I would like to express my sincere, deep gratitude to them.

First, I would like to give my immense gratitude toward my advisor, Dr. Nozomi Nishimura, for making the Ph.D. journey a great learning and growing experience in my career. She taught me how to design and perform experiments and trained me with critical thinking skills. She has always been supportive to my scientific curiosity and encouraged me to explore in many directions. Each trial gave me a valuable knowledge and lesson even though not all generated a successful result. I also want to thank to Dr. Chris Schaffer. From him, I learned technical skills and a way to communicate effectively. He is also an indispensable troubleshooter who fixes a problem on ablation laser in a minute. His delicate touch on laser made the system up and running, which saved majority of my time otherwise waisted. I sincerely thank to Dr. Xiling Shen, who gave productive guidance during early days in Cornell. I would also like to thank to my committee members, Dr. Alexander Nikitin, and Dr. Warren Zipfel for their thoughtful feedback and advises which directed my thesis to a right path. I convey my gratitude to Dr. Derek Huffman, our precious collaborator, for his interesting idea which made my thesis more fascinating story. He has supported me in many ways and helped my career development.

All people I met in Schaffer-Nishimura lab made my time in lab enjoyable and productive. I would like to thank Dr. Sung Ji Ahn, my good friend and colleague. The time we spent together helped me to survive in this isolated, suburban area. I miss those time with drinks and laughter and

hope we can reunite in big city soon. I thank Dr. Oliver Bracko, and Dr. David Small, our beloved postdocs, who have provided me scientific guidance and helped me to overcome challenges. Dr. Chi-Yong Eom, who already calls me as Dr. Choi, cheered me up whenever I lose my confidence and provided me fruitful discussion. I thank Dr. Poornima Gadamsetty, who taught me how to use microscope and helped me to successfully start my project in early days. Yu-Ting, who is my excellent conversation partner, you entertained my time in lab and fulfilled it with so much fun. I also thank Dennis Nyanyo, my undergraduate student. He has achieved so much more than I expected. I also like to convey my gratitude to my funding source, NYSTEM trainee grant. The financial support allows us to conduct critical experiments and made possible our scientific finding.

I would also like to thank the members of the Korean Tennis Club, who spent their time with me, played with me which released my stress and pressure, helped me well-balanced and maintained my mental health.

I would like to express my greatest thank to my family. I cannot be at where I am now without the love and care from my parents, grandparents, and close relatives. Their endless support and prayers made this journey possible. I would like to express special thanks to my grandmother, who always showed me a solid belief and endless love. It is great sorrow that she could not witness the end of my journey, but I am sure she is the one who will be pleased the most. My heart will always be with her.

To my dearest Nackchun, I am truly and deeply thankful for your encouragement and love. Thank you for standing by me through this journey. You have been always the source of my courage, strength, and passion for living.

TABLE OF CONTENTS

LIST OF FIGURES

LIST OF TABLES

LIST OF ABBREVIATIONS

2PEFM	two-photon excitation fluorescent microscopy
3D	three-dimensional
2PEF	two-photon excitation fluorescence
3PEF	three-photon excitation fluorescence
MPEF	multi-photon excitation fluorescence
SHG	second harmonic generation
THG	third harmonic generation
MPEFM	multi-photon excitation fluorescent microscopy
TA	transit-amplifying
Lgr5	leucin-rich repeat-containing G protein-coupled receptor 5
ISC	intestinal stem cell
CSC	cancer stem cell
GFP	green fluorescence protein
DNA	deoxyribonucleic acid
PI	propidium iodide
ROCK	Rho-associated protein kinase
IFN	interferon
ND	neutral density
PBS	phosphate-buffered saline
PFA	paraformaldehyde

YAP	yes-associated protein
TAZ	transcriptional coactivator with PDZ-binding
DBZ	dibenzazipene
ENS	enteric nervous system
RFP	red fluorescence protein
GI	gastrointestinal
AP	action potential
IP	intra peritoneal
FITC	fluorescein isothiocyanate
TTX	tetrodotoxin
NOS	nitric oxide synthase
VIP	vasoactive intestinal peptide
CRC	colorectal cancer
CCR9	chemokine receptor 9
CTC	circulating tumor cell

CHAPTER ONE

INTRODUCTION AND ORGANIZATION OF THE DISSERTATION

The work described in this dissertation involves the technical development of an *in vivo* imaging window for multiphoton microscopy as a tool to address various questions in studies of physiology and pathology. The intestinal stem cell niche and the enteric nervous system are of particular focus. Each chapter can be read independently.

Chapter Two provides fundamental background on two critical tools, *in vivo* multiphoton microscopy and femtosecond laser ablation. The nonlinear optical absorption effect is a shared principal for both techniques and the basic physics and characteristics are discussed for each technique.

Chapter Three provides background on the physiology and pathology of adult stem cells in the small intestine. It begins with normal physiology of the small intestine and the role of stem cells in maintaining homeostasis. It continues by describing stem cell niche and its impact on stem cell function. Then, I discuss pathological consequences after stem cell function is dysregulated and conclude the chapter by discussing remaining questions on stem cell biology.

Chapter Four is a complete manuscript published in the journal *Scientific Report*. It presents the technical innovations which are used to study robustness of alternating pattern found

at the base of the intestinal crypt, and the discovery of stem cell behavior after local injury. We believe this knowledge about stem cell behavior has been missed due to lack of methodology, highlighting the strength of our technique.

Chapter Five includes exploratory, uncomplete stories and discusses our future directions based on the new finding. This chapter aims to provide ideas that we are pursuing and shares preliminary data which will lead future projects. It presents the preliminary results of a study that explored cellular interactions between stem cells and resident macrophages. It also includes the results that explore the underlying mechanisms of the recovery process, and studies on epithelial integrity and stem cell phenotype.

Chapter Six is a complete manuscript published in *Nature Communication*. It provides an example application and successful modification of the abdominal window to study the enteric nervous system. I co-authored the paper and contributed by developing and modifying the abdominal window for neuronal study, in addition to generating a figure.

Chapter Seven provides an example application of the abdominal window used to study colorectal cancer *in vivo*. The importance of using chronic window is described as well as the current strategy and future direction of the abdominal imaging window for tumor studies.

Chapter Eight summarizes the work presented in this thesis. Technical accomplishments and its significance on other studies are discussed. The influence of our novel finding on stem cell behavior is also discussed along with the future directions.

CHAPTER TWO

NONLINEAR OPTICAL TECHNOLOGY TO VISUALIZE AND MANIPULATE BIOLOGICAL TISSUE

Over the past decades, optical imaging has been emerged as one of the crucial tools both in basic biological science and clinical diagnostics [1]. Optical imaging in biomedical research allows us to acquire real-time information about events happening inside of living organisms by a minimally or non-invasive assessment. The combination of multiphoton microscopy and femtosecond laser ablation enables imaging and manipulation at the micrometer spatial scale, deep within living samples. This enables work in whole animals, including mice, that can resolve the behaviors of single cells.

2.1 Multiphoton microscopy for biomedical science

The development of two-photon excitation fluorescence microscopy (2PEFM) opened an era of *in vivo* applications with high-resolution optical imaging [2]. This type of microscopy has enhanced penetration depth in scattering tissue compared to confocal microscopy, which enables the imaging of fluorescent structures within living samples. Since the first demonstration in 1990, 2PEFM has been extensively broaden the scope of biological questions that can be addressed *in vivo,* and has now become a technique of choice to study cellular interactions in biological and pathological conditions *in vivo* [1]. For example, the use of 2PEFM into cancer research enabled researchers to understand the steps of angiogenesis and cancer metastasis by visually identifying cellular key players during tumorigenesis [3]. In neuroscience, scientists were able to investigate neurovascular coupling and structural changes in Alzheimer's disease [4]. Nowadays, 2PEFM is a go-to technique for biological questions that involve cell-cell interactions or morphological and functional changes during disease development.

Three-photon excitation fluorescence microscopy has been introduced for deeper penetration of highly scattering biological tissues and higher signal-to-background ratio which can overcome many of the limitations of 2PEFM [5].

2.1.1 Multiphoton excitation fluorescence

When a fluorophore absorbs a photon, an electron is raised to an excited energy state, undergoes a non-radiative transition to an intermediate state, then is released back to ground state, emitting a lower energy photon. The energy of a laser photon must be equal to or greater than the energy difference between the ground and excited states in order to cause absorption by a fluorophore [6]. Two- or three-photon excitation is a nonlinear absorption process, in which a single fluorophore absorbs two or three photons simultaneously. Since it requires absorption of multiple photons by a single fluorescent molecule, excitation can only happen at a confined, sub-micrometer focus of the microscope objective in three dimensions, which enables optical sectioning in a highly scattering biological tissue. Optical sectioning is the ability to generate in-focus images of a plane in a three-dimensional (3D) sample, without physically cutting the tissue into pieces [7]. Multiphoton microscopy excites the fluorophore only at a tightly focused volume, so it inherently avoids excitation of fluorophores throughout the entire sample as occurs in confocal microscopy. In addition, multiphoton excitation fluorescence reduces phototoxicity significantly. To generate multiphoton excitation, a high peak power laser source is used in pulses which are normally shorter than a picosecond. This keeps the average power at a moderate level to avoid tissue damage [6].

Although 2PEF overcomes many challenges for *in vivo* imaging such as photobleaching and phototoxicity, the signal-to-background ratio still decreases in depth-dependent manner in a scattering biological tissue, which limits its use deep inside the tissue [5]. An effective strategy to increase penetration depth is using a longer excitation wavelength to reduce the attenuation of the excitation light by tissue. However, simply using a longer wavelength does not solve the problem since it requires fluorophores that excite at these wavelengths. Instead, researchers started to pay attention to 3PEF again which was also introduced in 1990s [8]. The use of 3PEF dramatically increases penetration depth in a highly scattering biological tissue with markedly improved signal-to-background ratio [9]. A significant advantage of 3PEF is that it not only uses longer excitation wavelength which travels deeper with less scattering, but it also localizes photoexcitation to the focal volume even tighter. 3PEF falls off as $\sim 1/z^4$ (where z is the distance from the focal plane), whereas 2PEF falls off as $\sim 1/z^2$. Therefore, 3PEF significantly increases signal-to-background ratio by orders of magnitude compared to 2PEF, which reduces background noise and enhances overall resolution in a deeper tissue [5]. For example, typical two-photon microscopy can image brain vasculature up to ~700 μm deep, but with three-photon microscopy, we can image the same structure up to ~1300 μm deep inside of a brain [5]. In addition, most fluorescent dyes frequently used in two-photon microscopy can be used under three-photon microscopy making three-photon microscopy even practical for *in vivo* imaging.

2.1.2 Harmonic generation

MPEF can also generate signal emission based on harmonic generation. Harmonic generation is a coherent process that interacts with non-centrosymmetric structures which provides

structural information of intrinsic molecule by producing radiation at exactly half of the exciting wavelength without need for an external fluorophore [1]. Since it does not require a fluorophore to be excited, it gives additional information in the living tissue without extra labeling. Harmonic generation has been frequently used in variety of biological studies *in vivo*. For example, in a tumor study, harmonic generation used to study changes in extracellular matrix structure along with tumor growth since collagen generates strong second harmonic generation (SHG) under two-photon excitation fluorescence microscopy [3]. Third harmonic generation (THG) also has been used for imaging myelin in central nervous system *in vivo* and for imaging atherosclerotic plaque [10, 11].

2.2 Femtosecond laser ablation

Similar to MPEF, high-energy pulsed lasers can deposit enough energy at a focused spot that can exceed the energy level required to ionize a molecule. Although each pulse has high peak power, the duration is limited to less than a picosecond so that the total energy is not enough to create thermal damage. Therefore, highly confined damage on a biological material can be used as a tool to precisely disrupt biological tissue [12, 13]. In previous research, this precise manipulation method using femtosecond laser was used as a tool to disrupt vessels to induce microhemorrhage without extra damage on surrounding tissue [14].

The work presented in this thesis used multiphoton excitation fluorescence microscopy and femtosecond laser ablation as tools to discover biological phenomenon. By using these two optical tools simultaneously, we were able to monitor cellular response after local injuries in real-time.

REFERENCES

[1] R.M. Williams, W.R. Zipfel, W.W. Webb, Multiphoton microscopy in biological research, Curr Opin Chem Biol 5(5) (2001) 603-8.

[2] W. Denk, J.H. Strickler, W.W. Webb, Two-photon laser scanning fluorescence microscopy, Science 248(4951) (1990) 73-6.

[3] W. Wang, J.B. Wyckoff, V.C. Frohlich, Y. Oleynikov, S. Huttelmaier, J. Zavadil, L. Cermak, E.P. Bottinger, R.H. Singer, J.G. White, J.E. Segall, J.S. Condeelis, Single cell behavior in metastatic primary mammary tumors correlated with gene expression patterns revealed by molecular profiling, Cancer Res 62(21) (2002) 6278-88.

[4] J.D. D'Amore, S.T. Kajdasz, M.E. McLellan, B.J. Bacskai, E.A. Stern, B.T. Hyman, In vivo multiphoton imaging of a transgenic mouse model of Alzheimer disease reveals marked thioflavine-S-associated alterations in neurite trajectories, J Neuropathol Exp Neurol 62(2) (2003) 137-45.

[5] N.G. Horton, K. Wang, D. Kobat, C.G. Clark, F.W. Wise, C.B. Schaffer, C. Xu, In vivo three-photon microscopy of subcortical structures within an intact mouse brain, Nat Photonics 7(3) (2013).

[6] W.R. Zipfel, R.M. Williams, W.W. Webb, Nonlinear magic: multiphoton microscopy in the biosciences, Nat Biotechnol 21(11) (2003) 1369-77.

[7] P.J. Campagnola, H.A. Clark, W.A. Mohler, A. Lewis, L.M. Loew, Second-harmonic imaging microscopy of living cells, J Biomed Opt 6(3) (2001) 277-86.

[8] C. Xu, W. Zipfel, J.B. Shear, R.M. Williams, W.W. Webb, Multiphoton fluorescence excitation: new spectral windows for biological nonlinear microscopy, Proc Natl Acad Sci U S A 93(20) (1996) 10763-8.

[9] D.G. Ouzounov, T. Wang, M. Wang, D.D. Feng, N.G. Horton, J.C. Cruz-Hernandez, Y.T. Cheng, J. Reimer, A.S. Tolias, N. Nishimura, C. Xu, In vivo three-photon imaging of activity of GCaMP6-labeled neurons deep in intact mouse brain, Nat Methods 14(4) (2017) 388-390.

[10] M.J. Farrar, F.W. Wise, J.R. Fetcho, C.B. Schaffer, In vivo imaging of myelin in the vertebrate central nervous system using third harmonic generation microscopy, Biophys J 100(5) (2011) 1362-71.

[11] D.M. Small, J.S. Jones, Tendler, II, P.E. Miller, A. Ghetti, N. Nishimura, Label-free imaging of atherosclerotic plaques using third-harmonic generation microscopy, Biomed Opt Express 9(1) (2018) 214-229.

[12] C.B. Schaffer, A. Brodeur, E. Mazur, Laser-induced breakdown and damage in bulk transparent materials induced by tightly focused femtosecond laser pulses, Measurement Science And Technology 12(11) (2001) 1784-1794.

[13] A. Vogel, V. Venugopalan, Mechanisms of pulsed laser ablation of biological tissues, Chem Rev 103 (2003) 577-644.

[14] N. Nishimura, C.B. Schaffer, B. Friedman, P.S. Tsai, P.D. Lyden, D. Kleinfeld, Targeted insult to subsurface cortical blood vessels using ultrashort laser pulses: three models of stroke, Nat Methods 3(2) (2006) 99-108.

CHAPTER THREE

BIOLOGY AND PATHOLOGY OF ADULT STEM CELLS IN THE SMALL INTESTINE

3.1 Small intestinal epithelium

The small intestine is a major organ for digestion and nutrition absorption for living organisms [1]. In addition to nutrition uptake, small intestinal epithelium provides a barrier function to protect the organs from external pathogens and bacteria. The inner epithelial lining of the small intestine consists of various cell types including enteroendocrine cells, goblet cells and enterocytes [2]. Epithelial cells exposed to the harsh luminal environment die at the tip of villus and are replaced by newly migrating cells from the crypt. This continuous regeneration is conducted by stem cells at the base of the crypt, also known as fast-cycling stem cells, which undergo cell division almost every day to maintain healthy epithelium [3]. Quiescent stem cells, another type of stem cell, are found above the stem cell niche (+4 position from the base of the crypt). Quiescent stem cells rarely divide under homeostasis but it is known to be activated upon tissue injury [1]. Progenitor cells leave the crypts and migrate up to transit-amplifying (TA) zone where cells undergo differentiation. From TA cells, all three major cell types (enterocytes, goblet cells and enteroendocrine cells) are formed and continue to differentiate during their migration along the crypt-villus axis. A fourth cell type, found at the base of the crypt, is the Paneth cell which is involved in defense against pathogens (Fig. 3.1) [4].

3.2. Stem cells in the small intestine

Stem cells are characterized by their ability to generate multiple cell lineages as well as maintain self-renewal capacity. The Clevers group first demonstrated that leucin-rich repeat-containing G protein-coupled receptor 5 (Lgr5) is an exclusive marker for actively cycling stem cells found at the base of the crypt in 2007 [4]. Since then, extensive research has been

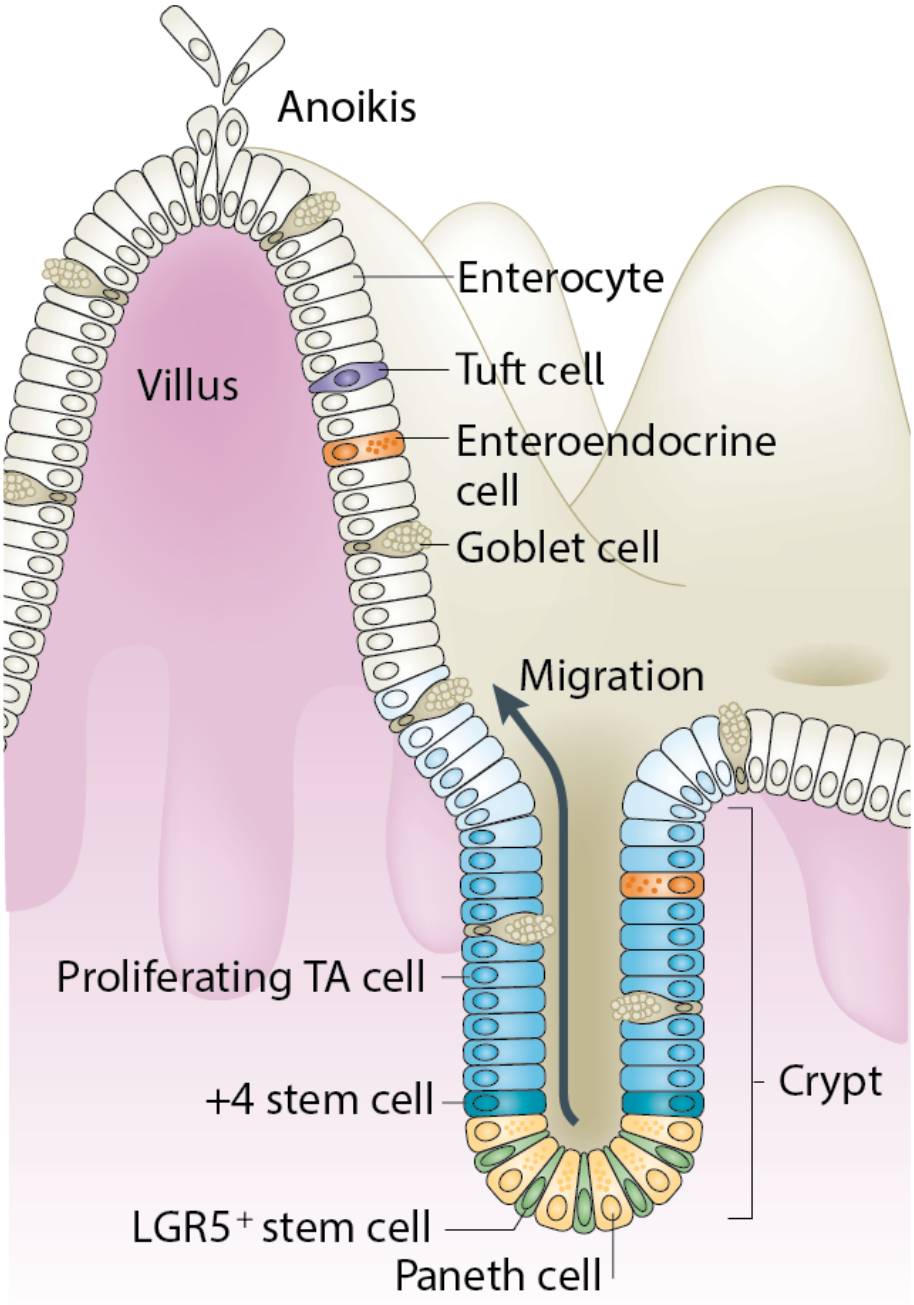

Figure 3.1 Crypt architecture of the small intestinal epithelium.
Lgr5+ stem cells constantly divide at the base of the crypt. Newly divided cells either migrate up towards TA zone where cells actively proliferate or reside in the crypt depending on niche factors provided from surrounding cells such as Paneth cells. TA cells are further differentiated into their designated cell types along with the migration up toward villus. At +4 position, there is another type of stem cell, quiescent stem cell, which rarely proliferates during homeostasis but is activated upon tissue injury. Figure is adapted with permission from the reference [1].

conducted on the characterization of $Lgr5^+$ intestinal stem cells (ISCs) in biological and pathological conditions. Lineage tracing experiments proved Lgr5+ ISCs have the stem cell capability of regenerating the complete crypt-villus axis from a single Lgr5+ ISC [4]. Complete epithelial turnover occurs every 3-5 days in a mouse and constant division of Lgr5+ ISCs provides sufficient progenitor cells to compensate for loss of cells at the tip of villus. Continual proliferation of Lgr5+ ISCs not only provides new cells for regeneration, but also for self-renewal at the base of the crypt to sustain the stem cell population. Therefore, maintaining a balance between differentiation and self-renewal is critical to maintain homeostasis. Asymmetric division of stem cells is a possible mechanism that could fulfill confined space and high-needs for progenitor cells. However, a study suggests that all Lgr5+ ISCs are equipotent meaning they divide symmetrically and neutral competition determines their fate after cell division [5]. This result emphasized the importance of the niche surrounding Lgr5+ ISCs, suggesting the importance of communication between stem cells and neighboring cells in determining the fate of newly divided cells as opposed to an inherently designated hierarchy.

3.3 Stem cell niche

The stem cell niche defines a microenvironment that supports the stem cells to sustain their stemness and enables them to maintain tissue homeostasis [6]. The niche cells provide cellular, physical and biochemical signals essential for maintaining stem cell properties. The intestinal stem cell niche comprises both epithelial cells, in particular the Paneth cells, and the mesenchyme compartment surrounding the crypts, which directly regulates stem cell behavior through signaling factors [2, 7]. Paneth cells, which are found in close association with the Lgr5+ ISCs at the crypt

base, are an important source of various niche factors, including Wnt and Notch ligands [6, 8]. Loss of Paneth cells *in vivo* decreased numbers of Lgr5+ ISCs, whereas the addition of Paneth cells to *in vitro* cultures substantially increased numbers of 'mini guts' generated from a Lgr5+ ISC, suggesting the importance of existence of Paneth cell in supporting Lgr5+ ISCs [6]. It is important to maintain tight control on stem cell behavior since misregulation can lead to cancerous tissue growth.

3.4 Lgr5+ ISCs in colorectal cancer development

It is widely accepted that cancer stem cells (CSCs), a small population in a tumor mass with stem cell properties, can initiate tumorigenesis and facilitate tumor progression. Many studies claim that Lgr5+ ISCs initiates cancerous tissue formation in intestine. Lineage tracing in a mouse model which developed intestinal adenoma showed that a small population (5-10 %) of cells with Lgr5+ showed similar abilities to normal Lgr5+ ISCs by generating all cell types found in adenoma [9]. Moreover, Lgr5 was also expressed at high levels in human metastatic colon cancer lines, further confirming Lgr5 as a marker of both normal and cancer stem cells [10]. Lgr5+ CSCs have a significant role in driving metastasis. Recent research suggests that elimination of Lgr5+ cells inhibited tumor growth but did not induce regression of tumor. Lgr5- cancer cells reacquired Lgr5 gene activity upon treatment cessation and initiated liver metastasis, suggesting that Lgr5+ CSCs are critical to develop malignancy [11].

3.5 Remaining questions in adult stem cell biology

Technical developments such as lineage tracing, selective ablation of a specific cell lineage, and development of a multicolor expressing mouse expanded our knowledge of adult stem cell biology significantly [4, 5]. There are two different types of stem cells at the crypt, which have distinct roles in different circumstances [12]. A complete deletion of $Lgr5^{+}$ ISCs can be rescued by dedifferentiation from other epithelial cells such as quiescent stem cells, and enteroendocrine cells, which demonstrated high plasticity of epithelial cells in the small intestine [13, 14]. However, the importance of the architecture only found in the stem cell niche of the small intestine is not fully understood yet. For example, it is unknown why Lgr5+ ISCs are positioned side by side with Paneth cells, how they recognize their position, and how the niche structure is related to stem cell function.

REFERENCES

[1] N. Barker, Adult intestinal stem cells: critical drivers of epithelial homeostasis and regeneration, Nat Rev Mol Cell Biol 15(1) (2014) 19-33.

[2] S. Tan, N. Barker, Epithelial stem cells and intestinal cancer, Semin Cancer Biol 32 (2015) 40-53.

[3] B.D. Simons, H. Clevers, Stem cell self-renewal in intestinal crypt, Exp Cell Res 317(19) (2011) 2719-24.

[4] N. Barker, J.H. van Es, J. Kuipers, P. Kujala, M. van den Born, M. Cozijnsen, A. Haegebarth, J. Korving, H. Begthel, P.J. Peters, H. Clevers, Identification of stem cells in small intestine and colon by marker gene Lgr5, Nature 449(7165) (2007) 1003-7.

[5] H.J. Snippert, L.G. van der Flier, T. Sato, J.H. van Es, M. van den Born, C. Kroon-Veenboer, N. Barker, A.M. Klein, J. van Rheenen, B.D. Simons, H. Clevers, Intestinal crypt homeostasis results from neutral competition between symmetrically dividing Lgr5 stem cells, Cell 143(1) (2010) 134-44.

[6] T. Sato, J.H. van Es, H.J. Snippert, D.E. Stange, R.G. Vries, M. van den Born, N. Barker, N.F. Shroyer, M. van de Wetering, H. Clevers, Paneth cells constitute the niche for Lgr5 stem cells in intestinal crypts, Nature 469(7330) (2011) 415-8.

[7] S.J. Morrison, A.C. Spradling, Stem cells and niches: mechanisms that promote stem cell maintenance throughout life, Cell 132(4) (2008) 598-611.

[8] K.Y. Chen, T. Srinivasan, K.L. Tung, J.M. Belmonte, L. Wang, P.K.L. Murthy, J. Choi, N. Rakhilin, S. King, A.K. Varanko, M. Witherspoon, N. Nishimura, J.A. Glazier, S.M. Lipkin, P. Bu, X. Shen, A Notch positive feedback in the intestinal stem cell niche is essential for stem cell self-renewal, Mol Syst Biol 13(4) (2017) 927.

[9] A.G. Schepers, H.J. Snippert, D.E. Stange, M. van den Born, J.H. van Es, M. van de Wetering, H. Clevers, Lineage tracing reveals Lgr5+ stem cell activity in mouse intestinal adenomas, Science 337(6095) (2012) 730-5.

[10] H. Uchida, K. Yamazaki, M. Fukuma, T. Yamada, T. Hayashida, H. Hasegawa, M. Kitajima, Y. Kitagawa, M. Sakamoto, Overexpression of leucine-rich repeat-containing G protein-coupled receptor 5 in colorectal cancer, Cancer Sci 101(7) (2010) 1731-7.

[11] F. de Sousa e Melo, A.V. Kurtova, J.M. Harnoss, N. Kljavin, J.D. Hoeck, J. Hung, J.E. Anderson, E.E. Storm, Z. Modrusan, H. Koeppen, G.J. Dijkgraaf, R. Piskol, F.J. de Sauvage, A distinct role for Lgr5(+) stem cells in primary and metastatic colon cancer, Nature 543(7647) (2017) 676-680.

[12] K.S. Yan, L.A. Chia, X. Li, A. Ootani, J. Su, J.Y. Lee, N. Su, Y. Luo, S.C. Heilshorn, M.R. Amieva, E. Sangiorgi, M.R. Capecchi, C.J. Kuo, The intestinal stem cell markers Bmi1 and Lgr5 identify two functionally distinct populations, Proc Natl Acad Sci U S A 109(2) (2012) 466-71.

[13] K.S. Yan, O. Gevaert, G.X.Y. Zheng, B. Anchang, C.S. Probert, K.A. Larkin, P.S. Davies, Z.F. Cheng, J.S. Kaddis, A. Han, K. Roelf, R.I. Calderon, E. Cynn, X. Hu, K. Mandleywala, J. Wilhelmy, S.M. Grimes, D.C. Corney, S.C. Boutet, J.M. Terry, P. Belgrader, S.B. Ziraldo, T.S. Mikkelsen, F. Wang, R.J. von Furstenberg, N.R. Smith, P. Chandrakesan, R. May, M.A.S. Chrissy, R. Jain, C.A. Cartwright, J.C. Niland, Y.K. Hong, J. Carrington, D.T. Breault, J. Epstein, C.W. Houchen, J.P. Lynch, M.G. Martin,

S.K. Plevritis, C. Curtis, H.P. Ji, L. Li, S.J. Henning, M.H. Wong, C.J. Kuo, Intestinal Enteroendocrine Lineage Cells Possess Homeostatic and Injury-Inducible Stem Cell Activity, Cell Stem Cell 21(1) (2017) 78-90 e6.

[14] H. Tian, B. Biehs, S. Warming, K.G. Leong, L. Rangell, O.D. Klein, F.J. de Sauvage, A reserve stem cell population in small intestine renders Lgr5-positive cells dispensable, Nature 478(7368) (2011) 255-9.

CHAPTER FOUR

INTESTINAL CRYPTS RECOVER RAPIDLY FROM FOCAL DAMAGE WITH COORDINATED MOTION OF STEM CELLS THAT IS IMPAIRED BY AGING

This chapter introduces the custom-built abdominal imaging window and its application for the study of adult stem cell behavior in the small intestinal crypts after small injury. In this work, we used two techniques introduced in chapter two. To visualize cellular dynamics, we used multiphoton microscopy and used femtosecond laser ablation to manipulate tissue precisely. This is a complete manuscript published in the journal *Scientific Reports*.

4.1 Abstract

Despite the continuous renewal and turnover of the small intestinal epithelium, the intestinal crypt maintains a 'soccer ball-like', alternating pattern of stem and Paneth cells at the base of the crypt. To study the robustness of the alternating pattern, we used intravital two-photon microscopy in mice with fluorescently-labeled Lgr5+ intestinal stem cells and precisely perturbed the mosaic pattern with femtosecond laser ablation. Ablation of one to three cells initiated rapid motion of crypt cells that restored the alternation in the pattern within about two hours with only the rearrangement of pre-existing cells, without any cell division. Crypt cells then performed a coordinated dilation of the crypt lumen, which resulted in peristalsis-like motion that forced damaged cells out of the crypt. Crypt cell motion was reduced with inhibition of the ROCK pathway and attenuated with old age, and both resulted in incomplete pattern recovery. This suggests that in addition to proliferation and self-renewal, motility of stem cells is critical for maintaining homeostasis. Reduction of this newly-identified behavior of stem cells could contribute to disease and age-related changes.

4.2 Introduction

The rapid regeneration of the intestinal epithelium is enabled by fast-cycling Lgr5+ intestinal stem cells (ISCs) crowded into the base of the crypt [1-4]. ISCs are not only limited in number and location, but also arranged in a specific pattern. ISCs expressing Lgr5 are intercalated between Paneth cells, which are secretory cells with antibacterial functions. This organization results in a 'soccer ball-like', mosaic pattern in which Lgr5+ ISCs form a continuous network that surrounds each Paneth cell [5]. In the healthy crypt, this alternating pattern is persistent despite

frequent cell division and migration [3, 6], but the dynamics of how this architecture is maintained is unknown. Aging is one of critical factors which gradually decreases the functionality of stem cells, including diminishing the self-renewal ability of stem cells, which impairs the balance between stem and differentiated cells. Aging also weakens cellular functions, such as mitigating reactive oxygen species and DNA damage [7]. However, how aging affects specific behaviors such as the patterning of intestinal crypt still not known.

To investigate the robustness of the patterning and its maintenance *in vivo*, we ablated individual cells in the crypt with high-pulse-energy femtosecond (fs) laser ablation and imaged the real-time dynamics of recovery with multiphoton microscopy [8, 9]. Such accurate manipulation is not achieved by current methods of radiation, chemical treatment, or genetic ablation of specified lineages [10, 11]. Surprisingly, after ablation of a small number of cells, migration of neighboring cells was sufficient to reestablish cellular contacts and the alternating pattern in the crypt base within hours, before any cells divided. In addition, we observed coordinated motion of the cells at the edge of the crypt base that expelled debris out towards the lumen. The repair movements were impaired by both inhibition of cellular movement and aging, highlighting the importance of this dynamic response for the integrity of the niche.

4.3 Results

4.3.1 Two-photon microscopy enables visualization of alternating pattern in the crypt

To understand how the crypt spatiotemporally maintains homeostasis *in vivo*, we modified previously demonstrated abdominal imaging windows [12, 13] with a 3D printed insert that sits under a portion of the small intestine to minimize movement without blocking normal digestive

functions (Fig. 4.1a, b). For imaging, animals were anesthetized, and the window frame was fixed with a clamp under the objective of a two-photon microscope with ablation capabilities (Fig. 4.1c). Lgr5+ crypt cells were visualized in mice expressing green fluorescent protein driven by the Lgr5 promoter (Lgr5-GFP) [4], while Paneth cells appeared dark (Fig. 4.1d). The vasculature was labeled by retro-orbital injection of Texas Red dextran (Fig. 4.1d). Blood vessels were stable over weeks, enabling us to use them as a roadmap to image the same areas repeatedly (Suppl. Fig. 4.1a). We injected Hoechst under the window to label nuclei. Time-lapse images show that the pattern of GFP and the number of Hoechst-labeled nuclei within a crypt was stable over the course of several hours (Fig. 4.1e, Suppl. Fig. 4.1b).

4.3.2 Cells damaged by femtosecond laser ablation are expelled from the crypt base

Cells were ablated selectively during imaging with photodisruption [14, 15] by pulses from a Ti:Sapphire regenerative amplifier. The damage was largely confined to the focal volume while neighboring cells and adjacent crypts were not affected (Suppl. Fig. 4.1c, d). In contrast, attempted ablation with the imaging beam at high power resulted in damage in a large region (Suppl. Fig. 4.1e). We first targeted a single Lgr5+ ISC in the crypt base. The GFP fluorescence from the targeted cell quickly dissipated, but nuclear labeling was still detected at the ablated site. Over the next 10-30 minutes, the nucleus of the ablated ISC disappeared from the base of the crypt and moved through the crypt lumen in the direction of the villi. Nuclei of the remaining cells appeared intact for the duration of the imaging time, up to 2 hours after ablation (Fig. 4.1g, h; Suppl. Fig. 4.1f). The ablation debris, still labeled with Hoechst, then gradually passed through the lumen until it was beyond the 50-μm field of view. Once the damaged cells were pushed out into the lumen,

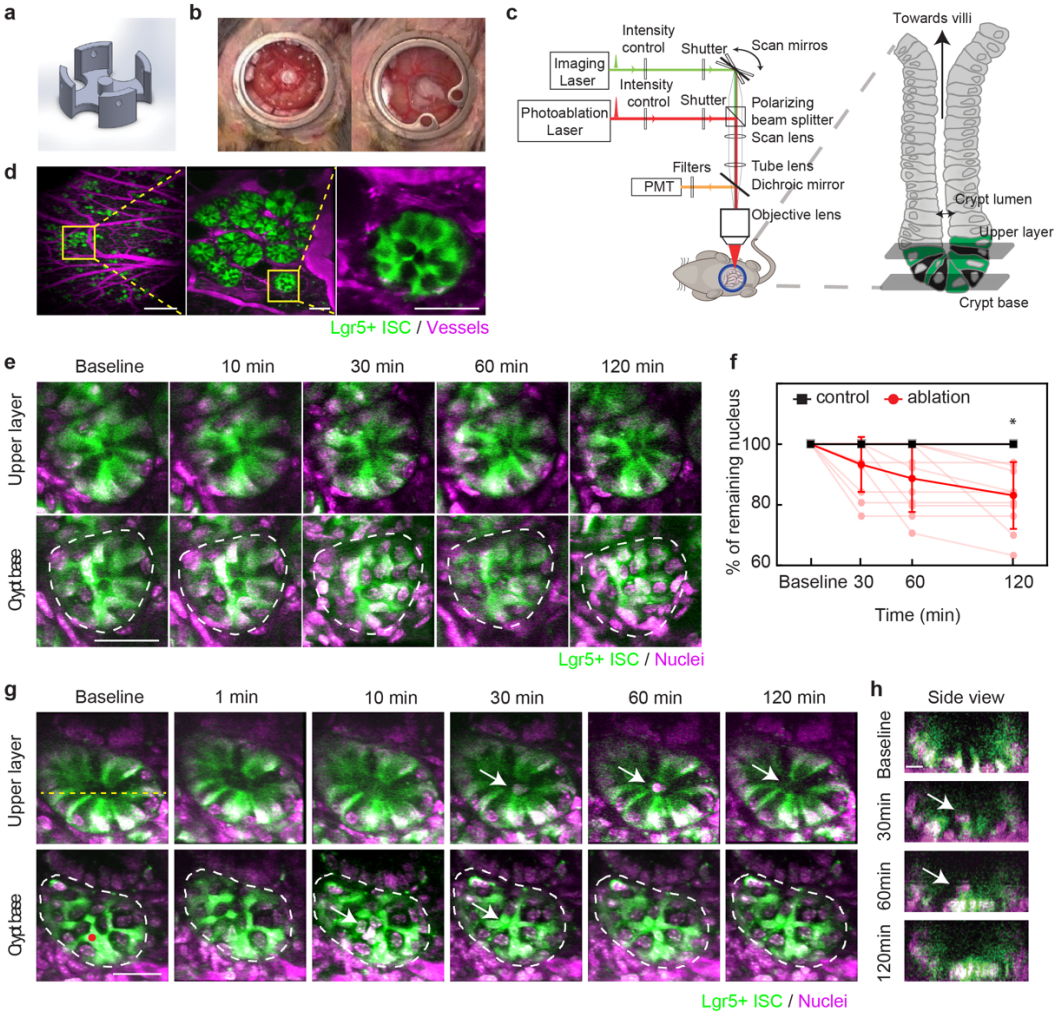

Figure 4.1 Rapid clearance of local damage after femtosecond laser ablation in a mouse small intestinal crypt (**a**) Schematic of 3D-printed insert that supports intestine in abdominal window. (**b**) Photos of abdominal window before (left) and after (right) closing with cover glass in a mouse. (**c**) Schematic (modified from Chen et al.[21]) of two-photon microscope showing two different laser paths used for both imaging and ablation. (**d**) In vivo two-photon microscopy images of a crypt at different magnifications in Lgr5-GFP mice expressing GFP in stem cells at the crypt base (green). Vessels are labeled with injected Texas Red dextran (magenta). Yellow boxes indicate magnified areas. Scale bars: 500 µm (left), 50 µm (middle and right). (**e**) Time-lapse images showing two different imaging planes in a crypt over 2 hours. Green indicates GFP. To label nuclei, Hoechst (magenta) was injected topically. Dashed white lines indicates the border of the crypt base. Scale bar: 30 µm. (**f**) Number of nuclei in crypt base after ablation (red, 11 crypts) and control (black, 5 crypts). Individual (light points) and averaged numbers displayed as a percentage of initial number. * multiple t-tests with Holm-Šídák, p = 0.005. (**g**) Time-lapse images of femtosecond laser ablation of one Lgr5-GFP cell in a crypt at two image planes. Red dot indicates position of ablation laser focus. White arrow indicates cellular debris from the ablation which moved from crypt base towards the villi. Scale bar: 30 µm. **(h)** Side view at line indicated in (g). Scale bar: 10 µm.

the number of remaining Hoechst-labeled nuclei at the base of the crypt did not change. In adjacent control crypts without ablation, the number did not change for two hours (Fig. 4.1f). No new nuclei appeared in either the control or ablated crypts within the two hours (Fig. 4.1f). Regardless of targeted cell type and number, ablation debris always moved up towards the villi and never towards the lamina propria of the intestine (74/74 crypts).

4.3.3 Pattern recovery is accomplished by Lgr5+ and Paneth cells already residing in the crypt

To further investigate the observation that there were no new nuclei during the first two hours of recovery, we used alternate visualization strategies to identify cells that did not express GFP. We used a variant of multiphoton microscopy, three-photon microscopy, which efficiently produces third harmonic generation (THG) with high peak-power lasers [16-20]. With 1,300 nm wavelength excitation, the cells without GFP in the crypt showed strong THG signals in granule-like clusters and resembled Paneth cells at the base of the crypt (bottom row) and at the upper layer (top row) (Fig. 4.2a). After ablation of a single ISC, we tracked cells at the crypt base over 2 hours and found that THG positive, GFP-negative cells neither appeared nor disappeared in the crypts (Fig. 4.2a, Suppl. Fig. 4.2, 13 crypts in 4 mice). We measured the fraction of cells without GFP in the crypt base with THG at baseline and post ablation and found that over 98% of the dark cells had THG (Suppl. Table 1). To confirm the THG signal was from a Paneth cell, we fixed the tissue and performed immunofluorescence for lysozyme (Fig. 4.2b). We found more than 98% of GFP-negative cells at the crypt base showed THG *ex vivo*, while more than 75% of these GFP-negative cells at the crypt were double-labeled with both THG and anti-lysozyme antibody. There were less

than 1% of cells which did not have THG nor the anti-lysozyme staining at the crypt base (Suppl. Table 4.1). These data suggest that the GFP-negative cells are Paneth cells.

4.3.4 Alternating pattern of intestinal stem and Paneth cells is rapidly restored by cell motion

Using two-photon microscopy for imaging, we studied how varying the number and type of ablated cells affected the crypt. Laser ablation of a Paneth cell resulted in a disruption and recovery similar to ablation of Lgr5+ ISCs (Fig. 4.3a, Suppl. Fig. 4.3b). At the base of the crypt, neighboring Lgr5+ ISCs moved towards the damaged area and restored a spatial configuration in which Paneth cells were separated from other Paneth cells by Lgr5-GFP cells within 2 hours. At 24 hours, the crypt was intact and had an alternating cell pattern (Fig. 4.3a, control crypt in Suppl. Fig. 4.3a). More extensive disruption was produced by ablating three ISCs (Fig. 4.3b) or three Paneth cells (Suppl. Fig. 4.3c), but these crypts were also able to re-establish the intercalating pattern by rearrangement within 2 hours. We quantified the change in the alternating ISC and Paneth cell pattern between baseline and 1 day after ablation of 1 to 3 ISCs or Paneth cells by calculating a rearrangement score that describes the change in alternating positions between ISCs and Paneth cells (Fig. 4.3c). Ablated crypts showed greater disparity from the baseline pattern than without ablation (Fig. 4.3d). We also looked at whether different types of ablation have different effects on rearrangement by separating the result based on ablation types (Suppl. Fig. 4.3d). Although targeting Paneth cells showed slightly greater rearrangement score than targeting ISCs, the result did not reach statistical significance. We next aimed to determine whether this observed pattern change resulted from loss of Lgr5+ ISC identity as reported by Lgr5-GFP, so we measured the intensity of fluorescence from GFP near the ablated site as a function of time after ablation of 1-3 cells (Fig. 4.3e). Although

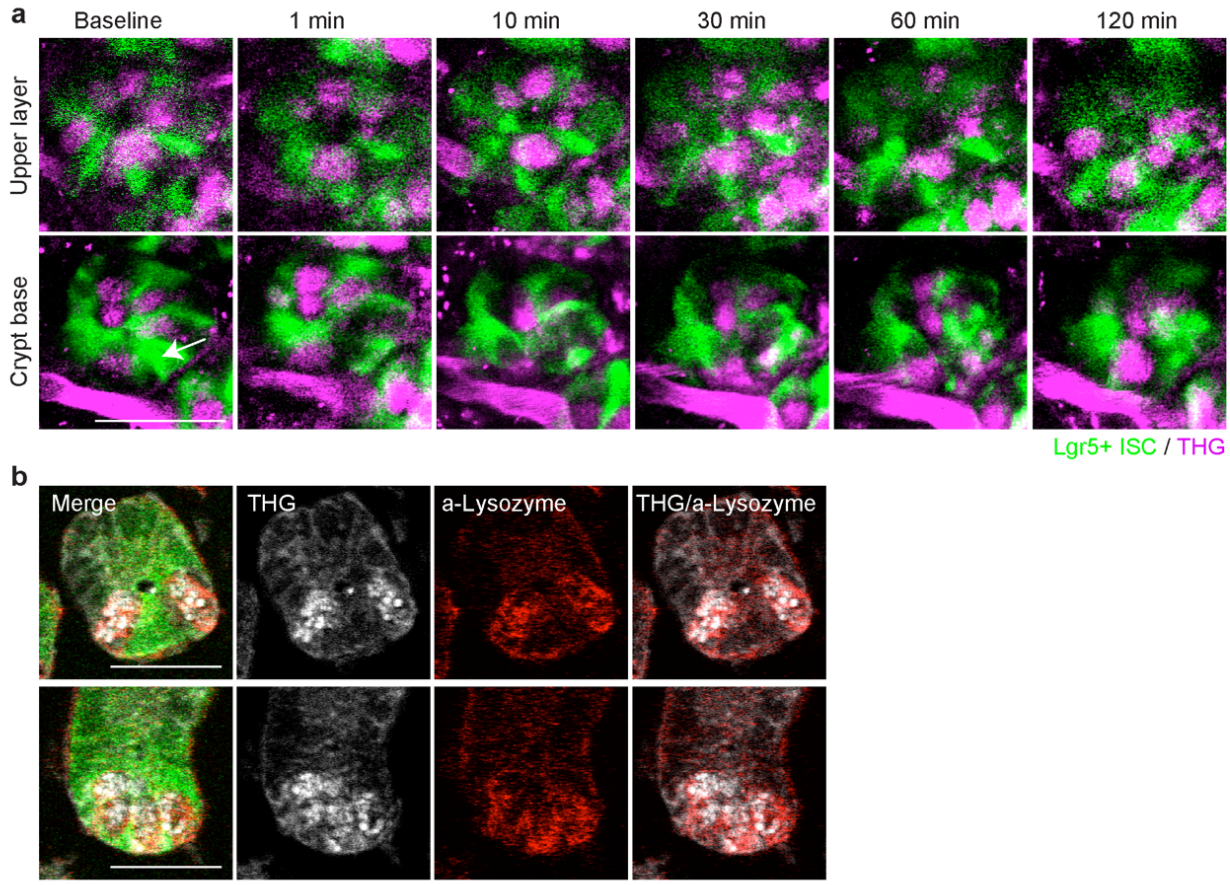

Figure 4.2 Pattern recovery at the base of the crypt is accomplished by cells residing in the crypt (**a**) Time-lapse images using three-photon microscopy after ablation of a single Lgr5+ ISC in the crypt with Lgr5+ ISC (green) and third harmonic generation (THG, magenta). THG image was taken with 1,300 nm wavelength laser excitation and Lgr5+ GFP image was acquired with 880 nm wavelength laser excitation. Red blood cells produce THG in the vasculature just outside the crypt. Images were overlapped via post-processing. White arrow indicates an ablated cell. Scale bar: 30 μm (**b**) Examples of two different crypts showing visualization of Paneth cells with THG and α-lysozyme staining in fixed tissue. THG signal was acquired under three-photon microscopy and α-lysozyme immunofluorescence was imaged under two-photon microscopy. Images were overlapped via post-processing. Scale bar: 30 μm.

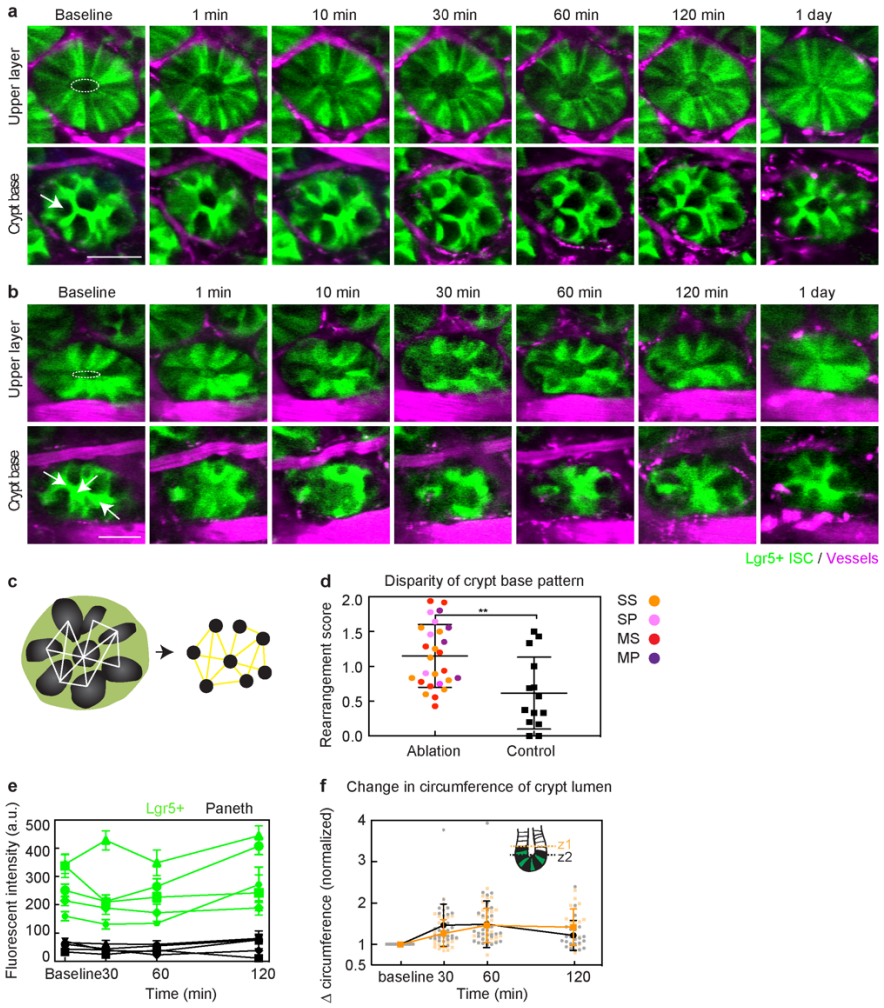

Figure 4.3 Perturbation of the crypt base pattern was followed by coordinated motion which restored the crypt base pattern and removed the debris from ablation (**a**) Time-lapse, two-photon microscopy images of ablation of a single Paneth cell showing two imaging planes. White arrow indicates the position of the ablation laser focus. In the upper layer, the white dashed ellipse indicates the circumference of crypt lumen at baseline. Scale bar: 30 μm. (**b**) Time-lapse images of ablation of multiple stem cells by focusing laser in three positions indicated by white arrows. White dotted ellipse shows the inner circumference at the baseline. Scale bar: 30 μm. (**c**) Schematic showing the strategy for describing the alternating pattern using network graphs. Each Paneth cell is a node (black). Edges were defined when nearest Paneth cells were separated by Lgr5+ ISCs. (**d**) Quantification of change in alternating ISC and Paneth cell pattern at crypt base using rearrangement score based on adjacency matrices calculated from networks defined in (**c**). ** p=0.0051, unpaired t-test. Orange indicates ablation of single stem cell, pink is of single Paneth cell, red is of multiple stem cells and purple is multiple Paneth cells. (**e**) Mean and standard deviation of fluorescent intensity from regions manually chosen in Lgr5+ ISCs and Paneth cells over time. (**f**) Measurement of inner circumferential change over time at different depths along the crypt lumen. Each value was normalized to the baseline. Mean and SD are plotted with dots representing individual crypts.

there were small fluctuations, the intensity of bright, Lgr5+ ISCs and dark, Paneth cells remained distinct.

4.3.5 Dilation and contraction of the crypt lumen pushes debris towards villi

During the rearrangement of the cells located at the crypt base after ablation, the diameter of the crypt lumen measured 15-20 μm above the crypt base, enlarged over 2 hours (Top rows in Fig. 4.3a, b). However, the outer diameter of the crypt stayed relatively constant during this time. We measured the inner circumference of the crypt lumen at the top of the crypt and just above the base cells at two different depths (average depth difference: ~13 μm, Fig. 4.3f). Dilation of the inner lumen occurred first nearer to the crypt base (z2) and reached a maximum by one hour, while the lumen closer to the villi (z1) continued to expand after one hour after ablation and remain enlarged at two hours. The lumen diameter closer to the crypt base (z2) at two hours was smaller than the maximum reached earlier (Fig. 4.3f). To label damaged cells, we injected propidium iodide (PI, retro-orbital) immediately before imaging, which enters cells only if the cellular membrane is disrupted and emits red fluorescence when bounds to DNA [22]. In unperturbed crypts, PI labeling was rarely observed, but red fluorescence was readily detected within several minutes at the targeted site following ablation. PI labeling clearly demonstrated that damaged cells were expelled towards the crypt lumen within an hour and then upward through the lumen toward the villi (Fig. 4.4a). The motion of the PI-labeled debris coincided with the crypt lumen dilation.

4.3.6 Crypt cell motion is dependent on the ROCK pathway

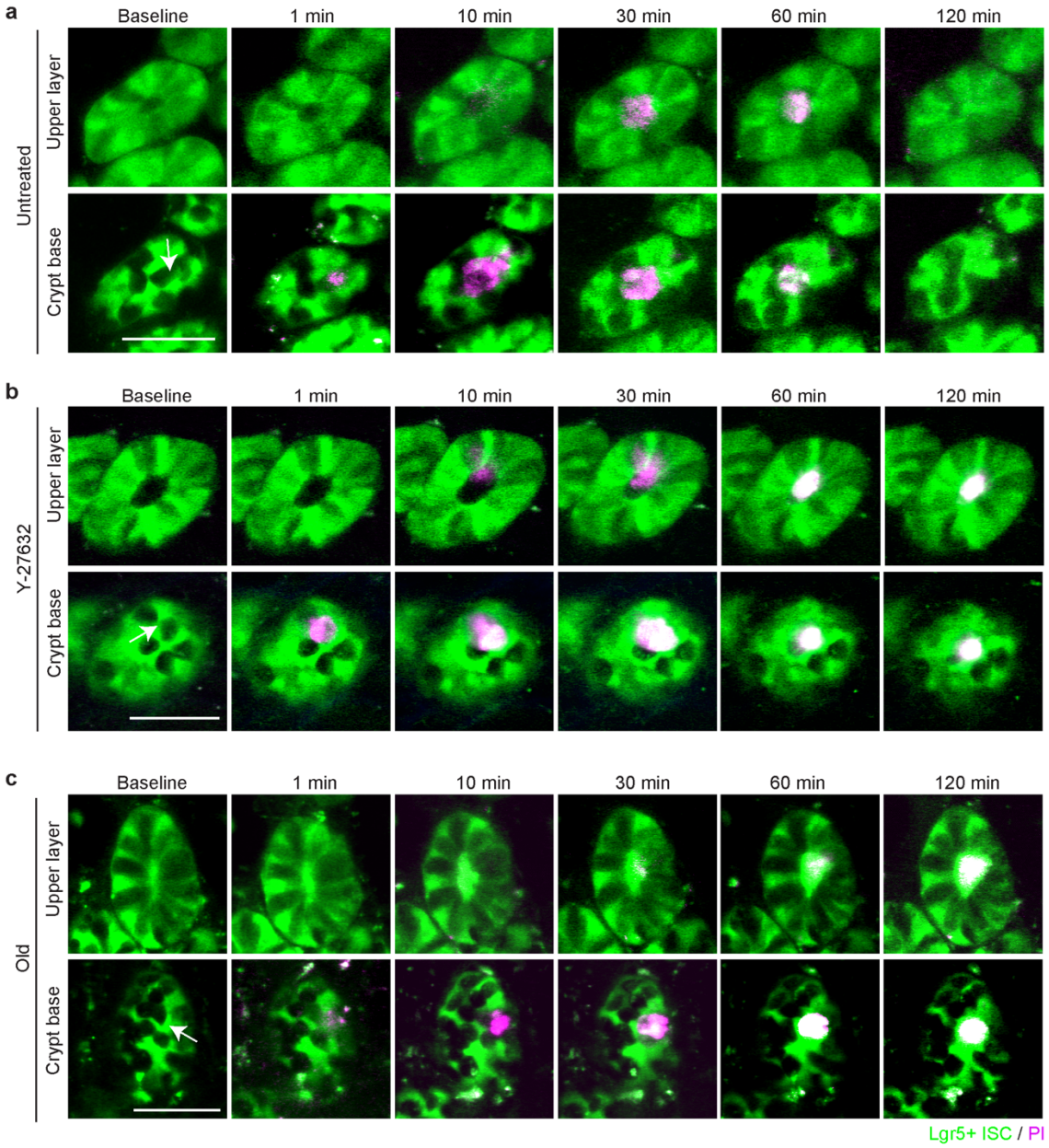

Figure 4.4 Cell motions after ablation are reduced after inhibition of ROCK signaling and in aged mice (**a**) Time-lapse images after ablation of one Paneth cell in crypt with Lgr5+ ISC (green) and propidium iodide (PI) (magenta) indicating damaged cells in a young mouse (6-month old) at crypt base and at lumen (15 µm apart). White arrow indicates the position of ablation laser focus. Scale bar: 50 µm. (**b**) Time-lapse images of ablation of one Lgr5+ ISC in crypt in an inhibitor-treated, young mouse (4-month old) at crypt base and at lumen (15 µm apart). To inhibit the cellular motility, Y-27632, was topically administered. A white arrow indicates the focus of ablation laser. Scale bar: 50 µm. (**c**) Time-lapse images of ablation of one Lgr5+ ISC at crypt base and at lumen (15 µm apart) in an aged mouse (17-month old) with PI injection. A white arrow indicates the focus of laser ablation. Scale bar: 50 µm.

To test whether this process was due to actin-mediated cell motion, as opposed to a passive reaction to external forces, we inhibited the ROCK pathway with topical application of Y-27632 [23]. ROCK inhibition did not noticeably change the baseline patterns, but reduced motion of the crypt cells, which resulted in an incomplete crypt base pattern at 1 day after ablation (Suppl. Fig. 4.4). The PI-labeled damaged cells remained at the base and elimination of the debris was incomplete after two hours (Fig. 4.4b). ROCK inhibition also affected crypt lumen dilation. In the crypt treated with Y-27632, the lumen did not change in size and the debris was detected in the lumen for an extended time period.

4.3.7 Cellular motion is impaired in aging crypts

Functional decline is a hallmark of aging in multiple tissues, including the gut, and this process is thought to be driven in part by deterioration in resident stem cell function [24, 25]. Therefore, we tested how the aged crypt cells respond to local damage by comparing young (2-6 months) with old (17-23 months) Lgr5-GFP mice. After ablation of a single Paneth cell, the aged crypt showed a response that was similar to an inhibitor-treated crypt. Cells at the crypt base did not show noticeable rearrangement after ablation, and PI-labeled damaged cells were remained at the base of the crypt for 2 hours, while at the upper layer, the crypt lumen had minimal dilation (Fig. 4.4c).

4.3.8 Area of damage is increased in aged and ROCK-inhibited crypts

To quantitatively compare damage in young animals with and without Y-27632, and old animals, we used the area of PI labeling at and just above the base after ablation of a single cell

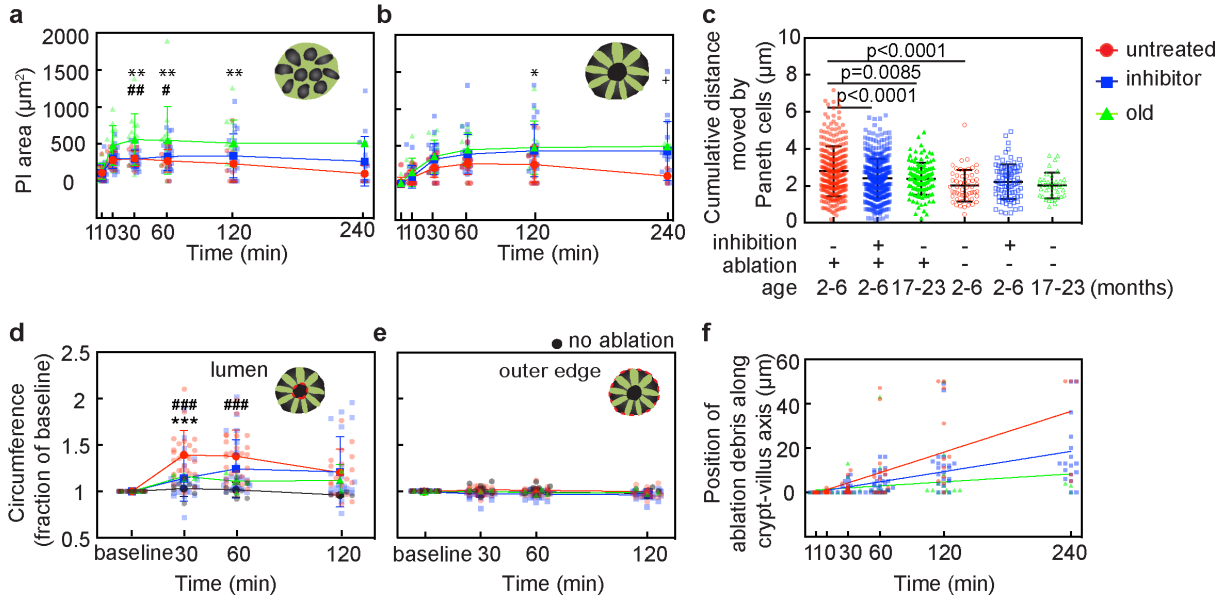

Figure 4.5 Comparisons of damage and crypt cell motion after single cell ablation in young mice with and without Y-27632, and aged mice (**a-f**) Comparison of crypt cell behavior in untreated, inhibited, and old mice. Red color indicates untreated, young mice, blue color is young, Y-27632 treated mice, and green color indicates old mice with no treatment. At each measurement time, dots are spaced for visual clarity. (**a-b**) Area labeled with propidium iodide (PI) after ablation at the crypt base (**a**) and at the upper layer (**b**). Mean and SD are plotted at each time point and dots represent individual crypts. * indicates comparison between untreated, young mice and old mice, # between Y-27632 treated, young mice and old mice, and + between untreated young mice and Y-27632 treated, young mice. **, ##, ++ indicates $p<0.01$, and *, #, + indicates $p<0.05$ (2-way ANOVA with Tukey's multiple comparisons). (**c**) Sum of distance moved by Paneth cells at the crypt base between baseline and one hour after ablation. Mean and SD are plotted with dots representing individual Paneth cells. Significance calculated with ANOVA with Tukey's multiple comparisons. (**d-e**) Measurement of inner lumen (**d**) and outer circumference (**e**) at the crypt at each time point after ablation. Each value was normalized to the baseline. Mean and SD are plotted with dots representing individual crypts. Black indicates measurements in control crypts adjacent to ablated crypts. * indicates comparison between untreated, young mice and Y-27632 treated, young mice, and # indicates comparison between untreated, young, ablated mice and untreated, young, unablated mice. ***, ### indicates $p=0.0003$ (2-way ANOVA with Tukey's multiple comparisons). (**f**) Position of cellular debris along the crypt lumen. Dots represent individual crypts at each time point. Lines represent linear regression.

(both ablation of single ISC and single Paneth cell were included). Immediately after ablation, the PI-labeled area at the base was the same across all groups, but the old group increased the most over time. In young, untreated mice, the PI-labeled area at and just above the crypt base increased and then decreased as the debris moved towards the villi (Fig. 4.5a, b). The peak value of the area was slightly delayed at the upper plane relative to the crypt base. Neither the young, treated group nor the old group showed decrease in PI area over two hours. In the old mice, the PI-labeling at the base was consistently larger than both young groups. In the upper plane, the PI-area in the old group was similar to the young, treated group. A linear regression to the PI area in the base of the crypt between 30 and 240 minutes (time after peak area) showed that only the young, untreated group had a negative slope ($R^2 = 0.99$, $p = 0.0052$), while in young, treated and old mice the slopes suggest PI area remains constant. At the upper level, the young, untreated group was also the only group to have a negative slope, but this did not reach significance.

4.3.9 Both rearrangement and peristalsis are reduced by age and ROCK inhibition

To compare the amount of rearrangement of base cells after ablation quantitatively, we measured the distance of Paneth cell movement summed over time points for the first one hour after ablation (Fig. 4.5c, Suppl. Fig. 4.3e). In young, untreated mice, Paneth cells in the damaged crypts moved on average about 135% further than those in adjacent, unablated, control crypts (Fig. 4.5c). After ablation, Paneth cells in young, Y-27632-treated mice and old mice moved only about 86% as far as in young, untreated mice.

ROCK inhibition and aging decreased dilation of the crypt lumen relative to the young, untreated group (Fig. 4.5d). After ablation, the inner circumference of untreated crypts in young

mice increased up to 142% of baseline at one hour and then decreased back towards baseline by 2 hours. In adjacent, unablated crypts, there was no change in either the inner or outer diameter. Y-27632 treatment reduced the increase of the inner circumference to only 125% of baseline and in old animals, the inner circumference only increased up to 110% of baseline. The outer circumference remained unchanged in all groups (Fig. 4.5e).

We next measured the average speed of debris clearance by tracking the position of PI-labeled cellular debris as it moved toward the villi after ablation (Fig. 4.5f). Untreated crypts in young animals showed the fastest speed, estimated from the slope of the position measured over 4 hours at 14 μm/hour, while inhibitor-treated and aged crypts had markedly slower elimination speed (7 μm/hour and 1 μm/hour, respectively). Using linear regression analysis, the slope of the untreated group showed a significant difference from Y-27632 treated, and the old group (R^2=0.9665, p=0.0023 for untreated vs inhibitor, p<0.0001 for untreated vs old).

Collectively, our findings suggest that the recovery process accompanied by coordinated cellular motion is a regulated process whose dynamics are impaired with aging (Fig. 4.6).

4.4 Discussion

How and why the crypt niche maintains the precise spatial arrangement of Paneth and Lgr5+ cells during the constant division of ISCs is still a perplexing question [21, 26-28]. In this study, *in vivo* time-lapse imaging and femtosecond laser photodisruption revealed that the response to localized ablation of a few crypt cells is immediate (Fig. 4.6). Surrounding cells quickly mobilize to extrude the debris. Cell migration fills the vacancy in the epithelium and restores the alternating pattern within hours, well before stem cells proliferate. The debris from ablated cells is

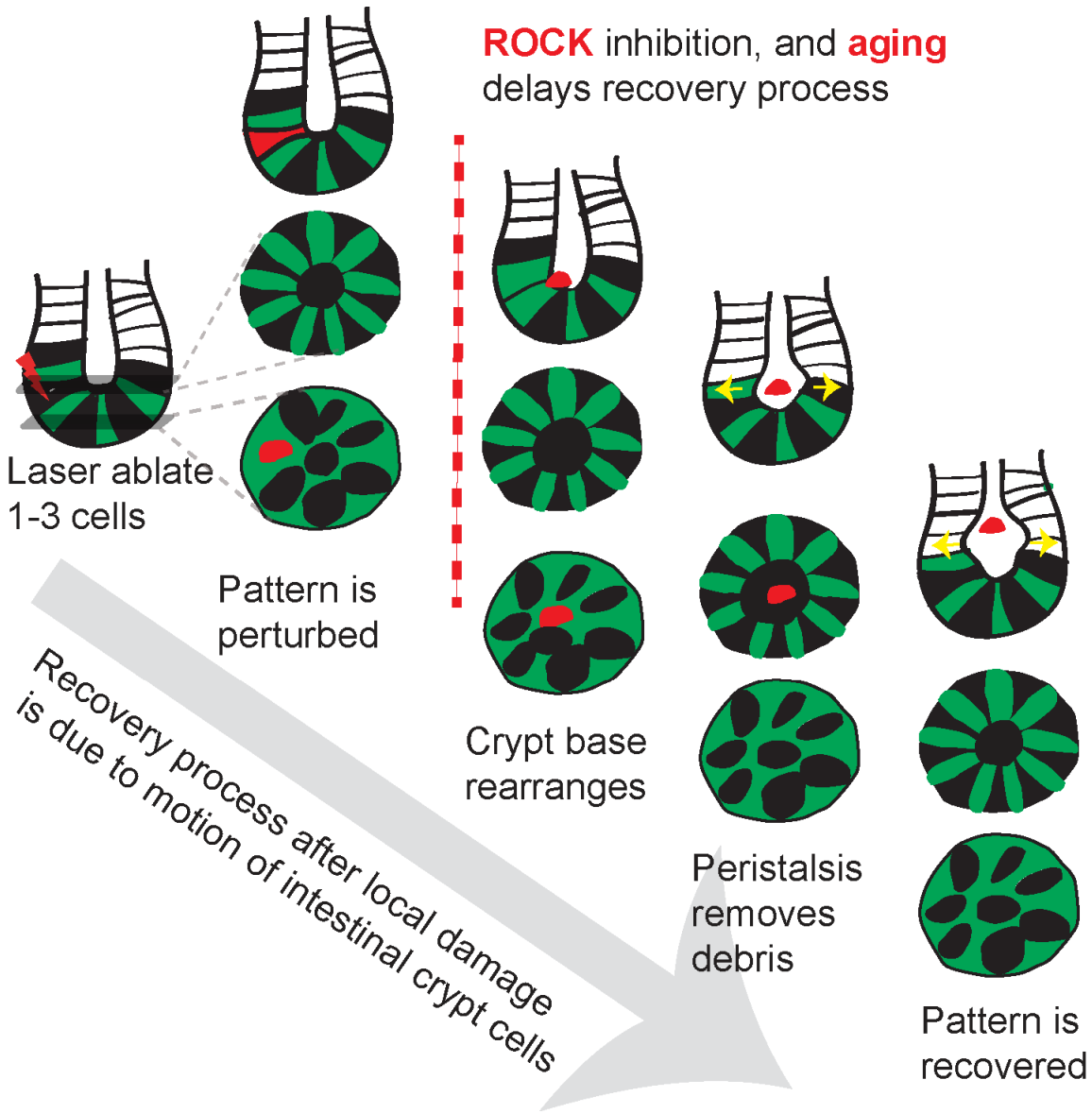

Figure 4.6 Coordinated cellular motion facilitates rapid recovery of crypt patterns after focal damage Schematic summarizing the recovery process after pattern disruption by ablation of crypt cells with laser ablation. Orchestrated motion of crypt cells restores the alternating pattern while pushing the cellular debris out toward the villi. These motions are attenuated with ROCK inhibition and aging resulting in a disrupted crypt pattern.

pushed out of the plane of the crypt base, in a manner similar to the removal of damaged cells in cultured epithelial monolayers, chick embryonic epithelium, *Drosophila* and developing brain of *Xenopus laevis* [29-32]. The speed of this expulsion was reduced by a ROCK inhibitor, suggesting that the mechanism in crypts could be similar to these other systems, in which dying cells activated neighboring cells to form a contractile actin ring. Even when different numbers of the two cells types were ablated (Fig. 4.3a, b; Suppl. Fig. 4.3b, c), the remaining cells still migrated to restore alternation in the cell pattern within 2 hours. The final patterns differed from those prior to ablation, suggesting that the arrangement is defined by interactions between the Paneth and stem cells, rather than dictated by the underlying mesenchymal cells. Signaling, such as Wnt/Notch, involved in maintaining stemness may also play a role in regulating this dynamic positioning [5, 21, 33, 34]. Lgr5-GFP labeling remained consistently bright through two hours (Fig. 4.3e) and was also bright the next day, which suggests, although not confirmative, that the process of rearrangement does not require loss or gain of the stem cell phenotype. Although conversion of other cells to the stem cell phenotypes is known to occur with certain types of injury and stimuli [10, 35], it is likely that the death of only a few cells with laser ablation is insufficient to trigger such a response.

In the intestinal crypt, the stem cells are at the end of a narrow tube, so that even after the expulsion from the crypt base, the cellular debris is trapped near the stem cells. The crypt cells performed a second type of motion, a peristalsis-like dilation of crypt lumen that appears to push the debris up the crypt towards the intestine interior. The dilation of the crypt lumen is likely crucial for effective extrusion of debris from the crypt base because it coincided with the arrival of debris in the crypt lumen. The peak dilation is earliest at the base of the crypt and later towards the villi, consistent with peristaltic pumping (Fig. 4.5a, b, f). The outer diameter does not change

(Fig. 4.5e), suggesting that the changes of inner circumference resulted from contraction of crypt cells rather than from forces exerted by the myofibroblasts surrounding the crypt or muscle cells of the muscular mucosae. Such a coordinated response has been observed in neural progenitor cells in the developing neuroepithelium after laser ablation [30], but has not been previously observed in adult stem cells. Activation of ROCK is a fundamental to regulate actin cytoskeletal activities and, although inhibition of ROCK pathway is a promising therapeutic target to alleviate with fibrosis in various organs [36, 37], consistent inhibition of such pathway could impair integrity of epithelium in pathophysiological conditions [38, 39].

Sporadic cell death, similar in sparsity to the carefully-controlled damage from femtosecond laser ablation, occurs in several biological processes. Most of the apoptosis in the intestinal epithelium that maintains constant cell numbers occurs at the villi, but occasional apoptosis does occur in the crypt [40, 41], suggesting that the rearrangement and peristalsis may play a role in normal function. In infection or IFN-γ stimulation, Paneth cells degranulate and then disappear from the stem cell niche [42-44]. In such instances, it is not only critical that fast cycling Lgr5+ ISCs can renew the epithelium with functioning cells, but that dead and damaged cells can be quickly and efficiently cleared from the cryptal microenvironment. Impaired clearance of damage in the stem cell niche can result in unnecessary inflammation [45]. Therefore, rapid removal of dying cells is important not only for pattern recovery, but also for limiting exposure to a dangerous environment.

Time-lapse imaging showed that the alternating pattern was restored within several hours, suggesting that the niche starts the repair process without waiting for ISCs to divide to replace the lost cells. Nevertheless, the stem cells will eventually divide to restore the total number of cells. It

has been previously shown that the "central" ISCs have a survival advantage over border ISCs, which may be pushed into the trans-amplifying compartment to start differentiation [46]. Future studies using intravital abdominal imaging may reveal how cell proliferation and plasticity contributes to the repopulation of the crypt. These novel observations could shed insights into previously unappreciated contributors to intestinal function and dysfunction in the context of intestinal diseases, infection and normal aging.

Aging is known to alter the number, rejuvenative capacity and senescence of stem cells [24, 47], but we have identified an additional function of ISC and Paneth cell that declines with aging, their motion dynamics in response to a perturbation. In other types of cells, aging is associated with a decrease in cellular function that results in less effective cytoskeletal remodeling and slower motion [48]. Extrinsic factors, such as increased tissue stiffness with aging, could in part underlie this alteration in cell contractility and motion [49-51]. Here, we found that the motion of neighboring cells was dramatically impaired, and cell debris 'lingered' in the crypts of old animals. Importantly, the observation that the aged crypt harbors reduced capacity to expel dead cells, thereby aggravating the local inflammatory response, could have important implications for the maintenance of intestinal homeostasis.

4.5 Materials and methods

4.5.1 Animals

To visualize stem cells in the crypt we used *Lgr5* $^{tm1(cre/ERT2)Cle}$*/J* mice (Lgr5-GFP) bred at Cornell University from breeders originally purchased from the Jackson Laboratory (Stock No. 008875). Some Lgr5-GFP mice were crossed with *Gt(ROSA)26Sor*$^{tm1(EYFP)Cos/J}$ mouse purchased

from the Jackson Laboratory (Srinivas, 2001 #108; Stock No. 006148). Other Lgr5-mice were bred with C57BL/6J mice (Stock No. 000664). No clear differences in labeling or phenotype were observed between these two breeding schemes, so all data has been pooled. For aging studies, old and young mice were bred at Albert Einstein College of Medicine and shipped to Cornell where they were housed for at least 3 weeks before imaging studies. No differences were apparent between the young mice from the Cornell and Einstein colonies, so data from both colonies were combined. All animals were housed at standard temperature (72 °F) and humidity-controlled conditions under a light cycle of 14 light and 10 dark hours with most imaging performed during the light hours. Mice were provided *ad libitum* access to water and a regular chow diet (Teklad 7912). Age and sex of subjects in each graph is provided in the supplementary table. All animal care and experimental procedures were approved by the Institutional Animal Care and Use Committee of Cornell University and were conducted in accordance with relevant guidelines and regulations.

4.5.2 Abdominal window preparation

Mice were anesthetized with 4% isoflurane in oxygen and maintained at ~2%. At the beginning of the surgery, animals received an anticholinergic, 0.05 mg per 100 g of mouse weight of glycopyrrolate or 0.005 mg/100 g of atropine subcutaneously, to assist in keeping the airways clear of fluid build-up. Body temperature was kept at 37 °C using a heating blanket controlled by a rectal thermometer. All areas to be incised were shaved and cleaned with 70% ethanol, and betadine, and were numbed with a 100 µL subcutaneous injection of 0.125% bupivacaine. Eyes were covered with veterinary eye ointment to prevent drying. The animals were hydrated with

subcutaneous injections of 5% glucose in saline for isotonic fluid replacement. Abdominal skin was removed in a circular shape to fit a titanium window frame (Brain Titanium Chamber Kit, 12 mm in inner diameter, APJ trading, CA). The frame was put on top of the abdominal muscle. The outer edge of the frame was covered by skin and secured with cyanoacrylate adhesive (Loctite 406, Henkel). The abdominal muscles within the inner circle were incised with scissors to expose the small intestine. Custom-designed scaffold to stabilize the intestine were 3D-printed (UPrint) out of ABSplus. The insert was placed under the small intestine so that a portion of the small intestine looped around the center post, entering and exiting the insert at the same gap between the supports. The insert was sutured to the skin outside of the frame by threading sutures through the holes in the four supports. The window was closed with a 12-mm diameter cover glass held on by the frame's retaining ring. Window and insert was placed in the abdominal area 1-1.5 cm below the rib cage. Dexamethasone (0.025 mg/100 g) and ketoprofen (0.5 mg/100 g) were injected intraperitoneally to help recovery after surgery and then daily for 2 days. Animals were returned to their home cage after recovery. Imaging was performed at least 24-48 hours after implantation to allow the position of the intestine in the window to settle and to minimize the effects of the surgery.

4.5.3 *In vivo* two-photon and three-photon excited fluorescence microscopy

Animals with abdominal window were imaged using a custom-built two-photon excited fluorescence (2PEF) microscope. All animals were anesthetized with isoflurane (1-2% in medical air) which was adjusted to maintain constant breathing rate during imaging time. To visualize vasculature, 50 µl of 2.5% Texas Red dextran (Molecular weight: 70,000; Thermo Fisher Scientific,

NY) in saline was injected retro-orbitally. Images were acquired using a Ti:Sapphire laser (Chameleon; Coherent, Santa Clara, CA) with wavelength centered at 880 nm for two-photon excitation and an optical parametric amplifier (OPA) (Coherent, Opera-F) seeded by a diode-pumped femtosecond laser (60 μJ/pulse at 1 MHz; Coherent, Monaco) with wavelength centered at 1,300 nm for three-photon excitation and third harmonic generation. Either a 20x, 1.0-NA (Zeiss, Thornwood, NY) or 25x, 1.05-NA (Olympus) water-immersion microscope objective was used for imaging and ablation. A 4X, 0.28-NA objective lens (Zeiss, Thornwood, NY) was used for low-resolution mapping. A 494-nm bandpass filter with 41-nm bandwidth, a 641-nm bandpass filter with a 75-nm bandwidth, and a 433-nm bandpass filter with 24-nm bandwidth was used for green fluorescent protein (GFP), Texas Red dextran dye, and THG, respectively. For Hoechst-labeled crypt imaging, we tuned the Ti:Sapphire laser to 830 nm. A 458-nm bandpass filter was used to detect Hoechst. Image stacks were acquired before and after laser ablation at 1.44 frames/s, with 1-μm spacing in the axial direction.

4.5.4 Disruption of cellular contact using femtosecond laser photodisruption

Selective disruption of cells was performed using a low-repetition-rate, high-pulse-energy Ti:Sapphire regenerative amplifier with 50-fs pulse duration, 1-kHz repetition rate, and 800-nm central wavelength (Legend-USP; Coherent, Santa Clara, CA). A polarizing beamsplitter cube was used to introduce this beam into the 2PEF microscope so that the pulses were focused at the center of the imaging field and in the 2PEF imaging plane, enabling real-time monitoring (Fig. 4.1c). Laser energy incident on the cells was controlled by neutral density (ND) filters, and a fast, mechanical shutter limited the number of pulses (2-5) incident on each cell. We started ablation

with lower power by using highest ND filter, and then gradually increased the power until we saw the formation of a small hole in the cytoplasm (Suppl. Fig. 4.1c). Incident laser energy to remove a single cell was typically about 50 nJ per pulse and did not exceeded 100 nJ.

4.5.5 Addition of chemical compounds

To label all nuclei in the crypt base, Hoechst-33342 (Thermo Fisher, Watham, MA; 2mg/kg) was injected under the window 1 hour before imaging. To inhibit ROCK protein signaling, Y-27632 (Sigma Aldrich, St. Luis, MO; 5mg/kg mouse weight in saline) was injected under the window before the start of imaging. This dosage was selected as the highest dose which did not alter crypt structure or change GFP expression patterns over one day (data not shown). Saline (0.9 %) (Phoenix Pharmaceutics, Burlingame, CA) was injected for the sham-treated group. To label damaged cells, propidium iodide (Cayman Chemical Company, Ann Arbor, MI; 100 µl of 1 mg/ml in PBS) was injected retro-orbitally.

4.5.6 Immunofluorescence

Animals were perfused with phosphate-buffered saline (PBS) and 4% paraformaldehyde (PFA) in PBS. Small intestine was fixed in 4% PFA overnight and stored in 30% sucrose. A small piece of small intestine embedded in optimal cutting temperature (OCT) compound and sectioned with 7 µm thickness for immunofluorescence. Tissue sections were placed on glass slides and washed with PBS for 5 min. 1% sodium dodecyl sulfate in PBS was used for antigen retrieval for 5 min. and then tissues were placed in blocking solution (mixture of 3 % bovine serum albumin, 10 % goat serum, and 0.1% triton-X 100 dissolved in PBS) for 1 hour. Tissue was treated with for

anti-lysozyme antibody (Abcam (ab108508), 1:50 in blocking solution) overnight and 1 hour with the secondary antibody (Alexa594, Life Science, 1:100 in blocking solution).

4.5.7 Image processing

All images were processed using ImageJ [51]. Frames that contained abrupt movement from respiration or peristalsis were deleted manually (approximately 20% of frames). To enhance signal/noise ratio, we applied a median filter with 1~2-pixel radius depending on the noise. Images within the stack was registered using a macro function called Stackreg [52]. For quantitative analysis, we used either an average projection of one to five frames at the base of the crypt or at an upper layer about 15 μm closer to the villi. This upper layer was at approximate at the +3 cell position in the crypt [4]. Unless otherwise noted, displayed images are average projections of five frames and intensity adjustment was limited to linear scaling.

4.5.8 Quantification of number of nuclei

In crypts labeled with Hoechst, we used image stacks of the crypt base region processed as above. To avoid possible bias in manual counting, the number of nuclei was counted in each image stack by an individual who was blinded to the order in which the images for a particular crypt were acquired. The average number of nuclei counted at the bottom of the crypt was 28. Statistical significance determined using t-tests with the Holm-Sidak method for multiple comparisons, with alpha=0.05. Each time point was analyzed individually, without assuming a consistent standard deviation.

4.5.9 Tracking of THG-positive cells

Image stacks of the crypts from *in vivo* and ex vivo images were processed as above. Each unlabeled cell in the crypt was first counted and assigned an identifier number, then cross referenced with THG image. Additionally, to ensure that we did not bias the analysis, we also recounted THG positive regions in the crypt first, and then quantified whether these regions were co-localized with unlabeled cells.

4.5.10 Rearrangement score for pattern disparity

To describe the alternating patterns of Paneth and Lgr5 cells, we devised a network graph representation using images of the crypt base. We manually defined nodes as the center of each Paneth cell. Two nodes were connected by edges if the two Paneth cells did not touch each other and a straight line between the two nodes did not touch any other Paneth cells. Edges represent the separation of Paneth cells by Lgr5 cells (Fig. 4.2c). The resulting network graph was used to calculate for a crypt with n Paneth cells an adjacency matrix at baseline, $M_{baseline}$, and 1 day after ablation, M_1. A rearrangement score that increases with more disparity between two patterns was defined as

$$score = \frac{1}{2n}\sum_{j=1}^{n}\sum_{i=1}^{n}(M_{baseline}(i,j) - M_1(i,j))^2$$

4.5.11 Measurement of fluorescence intensity

To assess stability of Lgr5-GFP signals, we used processed and projected image (2-5 frames in average). Mean fluorescence intensity was measured from manually selected areas from

same Lgr5-ISC and Paneth cell near the ablation at each time point. The analysis regions were selected by a user blinded to the treatment (control versus DBZ) and the timing of each image to reduce possible bias.

4.5.12 PI label quantification and tracking

In animals injected with PI, projected images (2-7 frames average projection) from the processed stack were used from the crypt based and the upper layer. The area of PI-labeling was measured in ImageJ by manually drawing an outline of PI signal. To track the position of the PI-labeled ablation debris along the crypt-villus axis as it moved into the crypt lumen, each image in the stack of images was processed with median filter to reduce noise. In order to maintain consistency in spacing, we did not delete moving frames. The first frame of the crypt base was used as the reference to align the different time points. The position of the lowest edge of the PI signal was recorded at each time. Linear regression was performed and plotted for each group.

4.5.13 Tracking of Paneth cell movement within crypt base

To measure the movement of Paneth cells, we used images of the crypt base processed as above with both projections and single frames. Each Paneth cell at the crypt base was numbered and individually tracked. Using image J, the X-Y coordinates of the center of the Paneth cells were manually measured at baseline, 10, 30, 60 minutes after ablation. To align images between time points, we matched the position of center of the crypt so that the trajectory of each Paneth cell was identified (Suppl. Fig. 4.2e). The sum of the total distance moved by each Paneth cell was plotted using Graphpad software. The untreated group includes animals that were injected with saline as

a sham treatment and animals with no injection, because saline injected, young mice resulted in similar dynamics as young, un-injected mice.

4.5.14 Measurement of crypt lumen and outer circumference

The inner and outer circumference of the crypt was measured in single processed image frames. The circumference was measured by manual tracing along the lumen edge and the outer edge of Lgr5 labeling in ImageJ. Inner and outer circumference was measured from same image frame. Since crypts in animals with no injection did not show significant difference from sham, saline-injected animals, both data were included and displayed as the untreated group.

4.5.15 Statistics

Graphpad Prism was used to prepare all graphs and for statistical analysis. Unless otherwise stated, to test for differences at various points in time, we used 2-way ANOVA with Tukey's multiple comparison test and other tests are noted in text and captions.

4.6 Acknowledgements

This study was supported by the Empire State Stem Cell Fund through New York State Department of Health Contract # C30293GG and NIH R01 GM114254. DMH is supported by NIA R56AG052981, P30AG038072 and the American Federation for Aging Research (AFAR). We thank Dennis Nyanyo for technical assistance with histology.

4.7 Author Contributions

J.C. developed methods, conducted experiments, wrote the manuscript and performed analysis. N.R., P.G., D.J.J. performed experiments and developed methods. S.M.L., T.T., D.M.H., X.S. and N.N. edited the manuscript and designed the experiments. N.N. supervised, designed experiments and wrote the manuscript.

4.8 Additional Information

Competing Interests: The authors declare that there is no competing interests.

4.9 Supplementary Figures and Tables

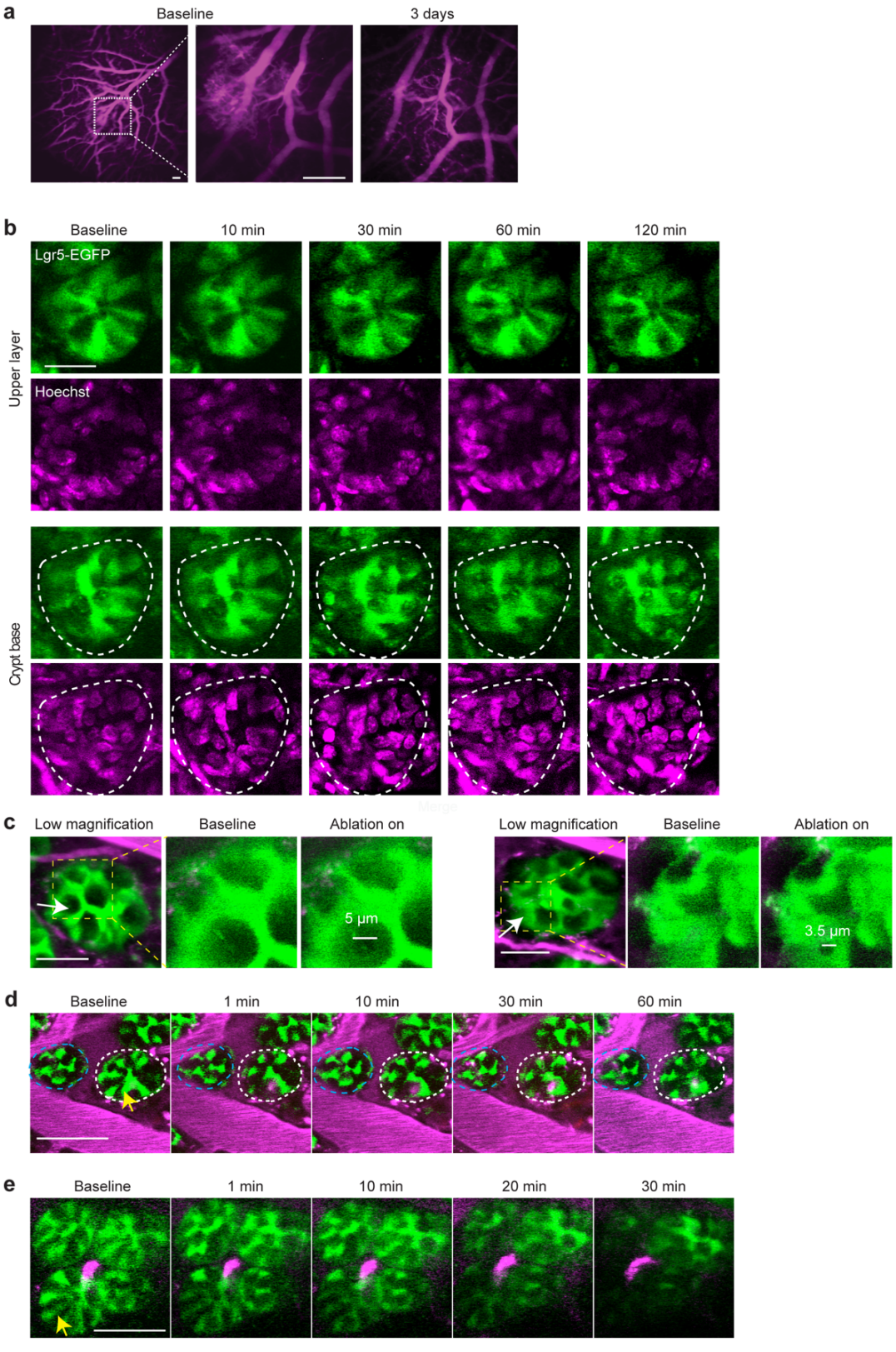
a
Baseline
3 days
b
Baseline
10 min
30 min
60 min
120 min
Lgr5-EGFP
Hoechst
Upper layer
Crypt base
Merge
c
Low magnification
Baseline
Ablation on
5 μm
Low magnification
Baseline
Ablation on
3.5 μm
d
Baseline
1 min
10 min
30 min
60 min
e
Baseline
1 min
10 min
20 min
30 min

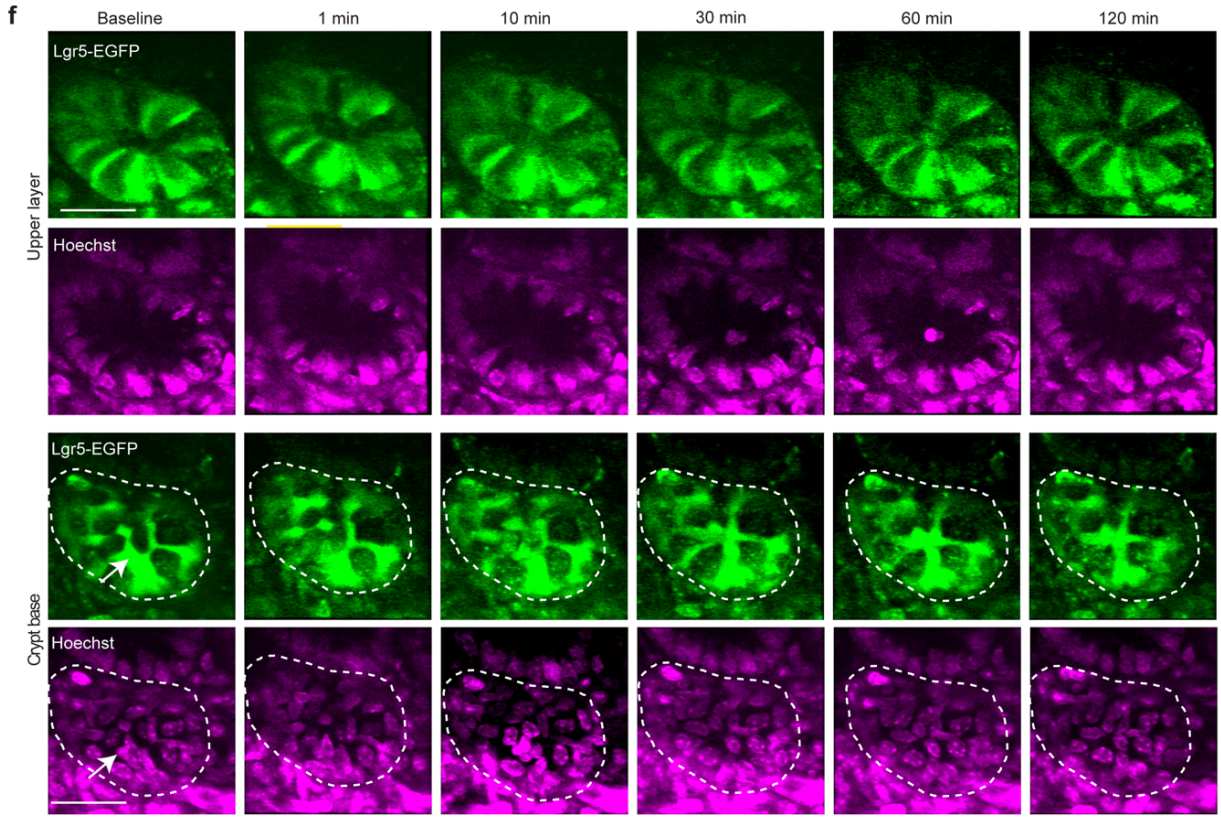

Suppl. Fig. 4.1. **The alternating pattern of the crypt base was rapidly restored after local damage due to femtosecond laser ablation.** (**a**) Time-lapse images of small intestinal vasculature at baseline and 3 days showing stability of vasculature over time. To visualize the intestinal vasculature, FITC-dextran (magenta) was injected retro-orbitally. Scale bar: 100 µm. (**b**) Time-lapse images of a crypt in a young mouse labeled with Hoechst with no ablation. This is the same example as Fig. 1e, but the images are separated into two channels to show Lgr5-GFP (green) and Hoechst (magenta). White dash line indicates crypt border. Scale bar: 30 µm. (**c**) Images of crypts during ablation. Yellow dashed line marks the magnified area. When the ablation laser hits, it creates a small hole in the cytoplasm (left: Paneth cell, right: ISC). Green is GFP and magenta shows dye in vasculature. Scale bar: 30 µm. (**d**) Time-lapse images of two adjacent crypts in a Lgr5-GFP mouse. Dashed line indicates each crypt. A yellow arrow indicates focus of laser ablation. Scale bar: 50 µm. (**e**) Attempted ablation with two-photon imaging beam (50s irradiation time, 80-MHz, ~4nJ, 880 nm). Yellow arrow indicates the region scanned by imaging beam at high power. Decline of fluorescent intensity was observed at the targeted crypt and adjacent crypts. This effect is likely both due to the motion of tissue over the long irradiation time as well as the photochemical or thermal nature of the damage. Magenta shows vascular dye. Scale bar: 20 µm. (**f**) Time-lapse images of ablation of one ISC in a Lgr5-GFP mouse displayed with fluorescence channels separated to show Lgr5-GFP (green) and Hoechst (magenta). This is the same example as Fig. 4.1G and H. White dashed line indicates outline of the crypt. Scale bar: 30 µm.

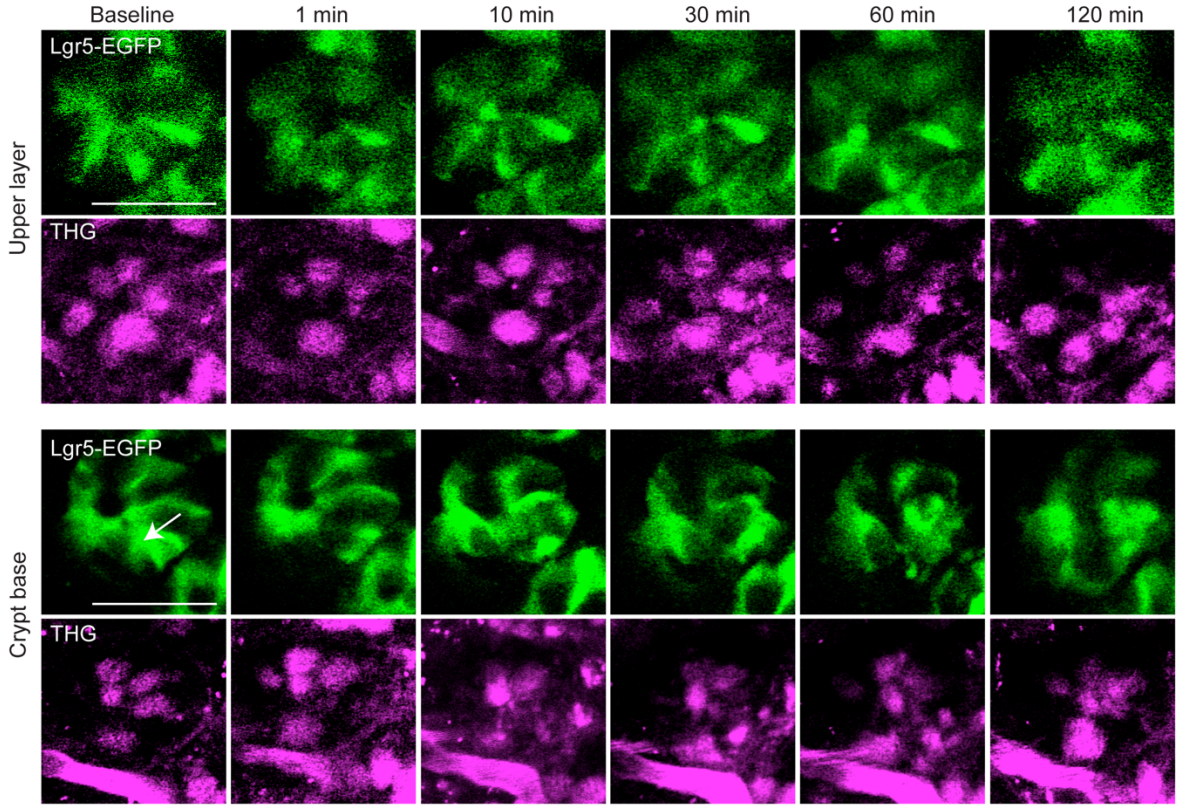

Suppl. Fig. 4.2. Pattern recovery at the base of the crypt is accomplished by cells residing in the crypt. This is the same example as Fig. 2 shown here with channels separated for clarity. Time-lapse images after ablation of a Lgr5+ ISC in crypt with Lgr5+ ISC (green) and third harmonic generation (THG, magenta). The THG image was taken with 1300 nm wavelength laser excitation and the Lgr5+ GFP image was acquired at 880 nm wavelength. White arrow indicates the area laser focused. Scale bar: 30 µm

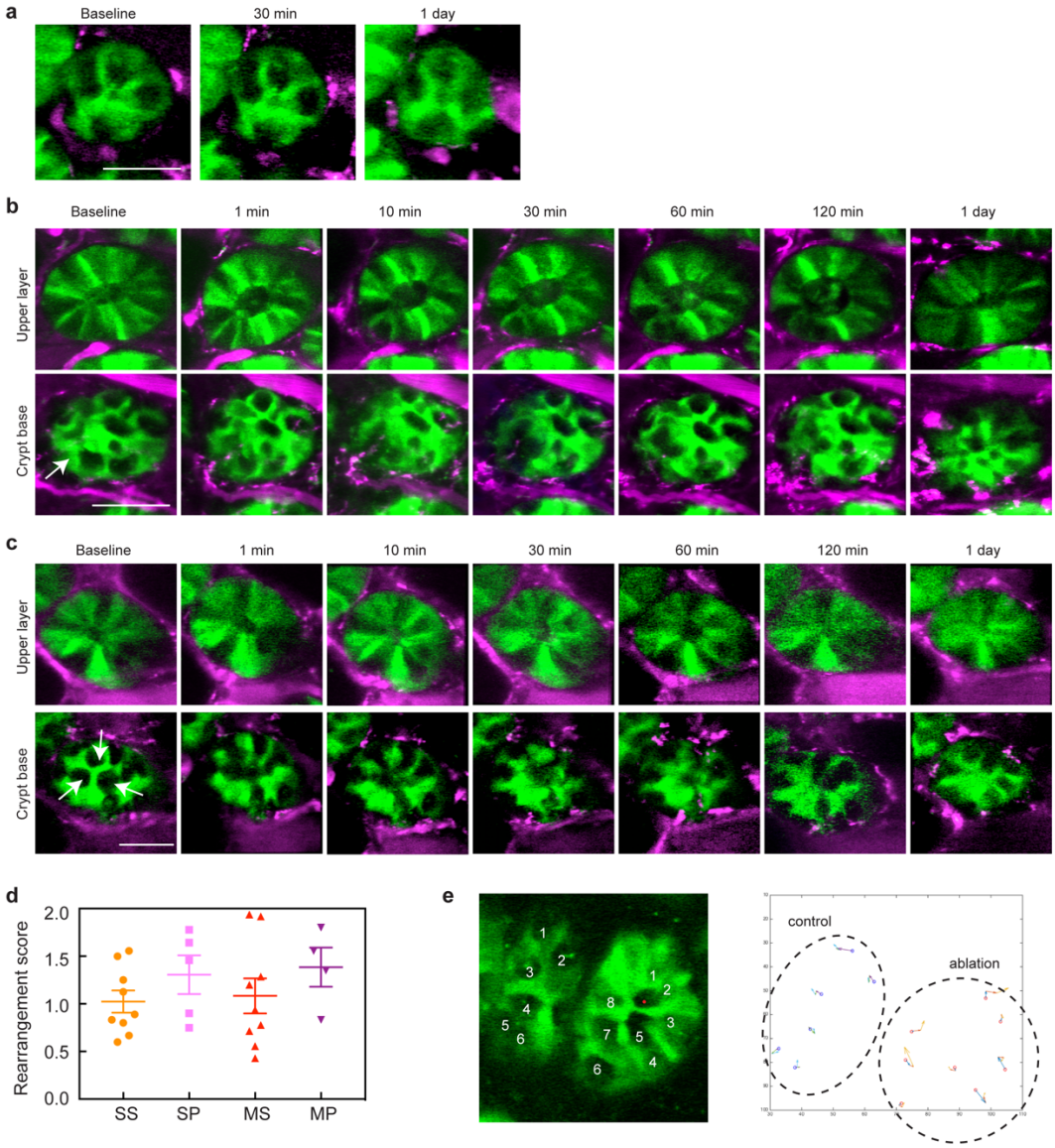

Suppl. Fig. 4.3. **Pattern recovery was accomplished by coordinated motion of crypt cells.** (**a**) *In vivo* two-photon microscopy images of a crypt over one day in Lgr5-GFP mouse. Green is GFP. Magenta shows Texas Red in blood vessels and autofluorescence. Scale bar: 20 µm. (**b**) Time-lapse images of crypt with single intestinal stem cell (ISC) ablation. A white arrow indicates ablated Paneth cell. Scale bar: 30 µm. (**c**) Time-lapse images of a crypt with ablation of multiple Paneth cells. White arrows indicate Paneth cells ablated. Scale bar: 30 µm. (**d**) Individual plot of rearrangement score depending on the different types of ablation from Fig. 2d. SS stands for single ISC, SP stands for single Paneth cells, MS stands for multiple ISCs, and MP stands for multiple Paneth cells. (**e**) Representative example of tracking Paneth cell movement at the crypt base. We numbered each Paneth cell and then got the x-y coordinate from each time point up to 1 hour. The trajectory of Paneth cells in two crypts are shown with open circles representing the starting position at baseline, and vectors representing the new positions at 10, 30 and 60 minutes after ablation.

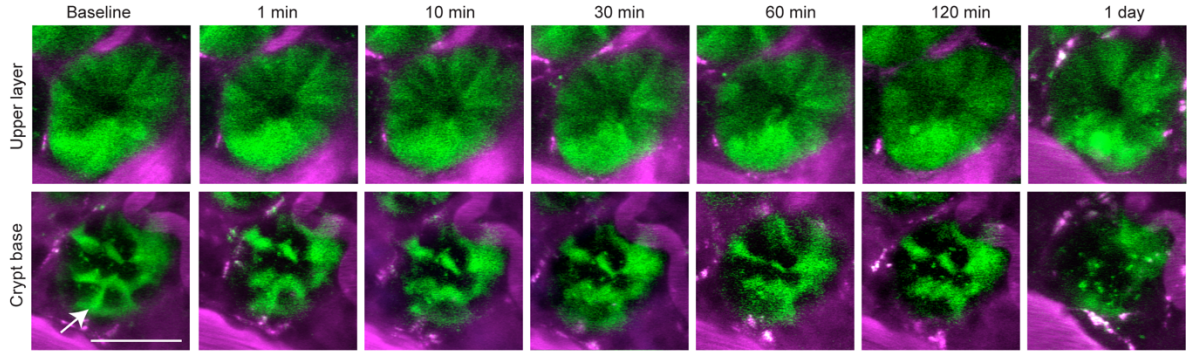

Suppl. Fig. 4.4. **Crypt cell motion is dependent on the ROCK pathway.** Time-lapse images of crypt with ablation of single ISC. To inhibit the cellular motility, Y-27632 was topically administered. White arrow indicates a ISC ablated. Green shows GFP and magenta shows dye injected into vasculature as well as some autofluorescence. Scale bar: 30 μm.

Suppl. Table 4.1. Third harmonic generation imaging and immunohistology.
THG signal was collected with three-photon microscopy at 1,300 nm wavelength after ablation of 1 to 3 Lgr5+ ISCs or Paneth cells. 13 crypts in 4 mice was tracked for *in vivo* measurement. For *ex vivo* staining, 16 crypts from 10 different sectioned tissues were examined.

***In vivo* imaging**	**Ablation**		**Control**	
Baseline	Unlabeled	THG labeled	Unlabeled	THG labeled
	1.45%	98.55%	1.72%	98.28%
After 2 hours	Unlabeled	THG labeled	Unlabeled	THG labeled
	1.22%	98.78%	0%	100%

***Ex vivo* staining**	Unlabeled	a-Lysozyme labeled	THG labeled	Dual labeled
	0.93%	0.93%	22.22%	75.92%

Suppl. Table 4.2. Age and sex of animals used in statistical analysis.

Fig. 4.1f	**Ablation**		**Control**	
crypts (number)	11		5	
mice (number)	4		3	
age	3-10m		3-6m	
sex	F	M	F	M
	3	1	2	1

Fig. 4.3d, Suppl. Fig. 4.3d	**Ablation**		**Control**	
crypts (number)	28		15	
mice (number)	9		5	
age	2-5m		2-5m	
sex	F	M	F	M
	4	5	2	3

Fig. 4.3e	**Ablation**		**Fig. 4.3f**	**Untreated**	
crypts (number)	5		crypts (number)	34	
mice (number)	2		mice (number)	17	
age	3m		age	2-6m	
sex	F	M	sex	F	M
	2	0		10	7

Fig. 4.5a, b, f	**untreated**		**inhibitor**		**aged**	
crypts (number)	14		24		13	
mice (number)	6		6		5	
age	2-6m		2-6m		17-23m	
sex	F	M	F	M	F	M
	5	1	4	2	0	5

Fig. 4.5c	**untreated**		**inhibitor**		**aged**	
crypts (number)	22		31		7	
mice (number)	9		9		3	
age	2-6m		2-6m		17-23m	
sex	F	M	F	M	F	M
	9	0	5	4	0	3

Fig. 4.5d, e	**untreated**		**inhibitor**		**aged**	
crypts (number)	29		28		4	
mice (number)	15		9		3	
age	2-6m		2-6m		17-23m	
sex	F	M	F	M	F	M
	9	6	5	4	0	3

REFERENCES

[1] C.P. Leblond, C.E. Stevens, The constant renewal of the intestinal epithelium in the albino rat, The Anatomical Record 100(3) (1948) 357-377.

[2] O.J. Sansom, K.R. Reed, A.J. Hayes, H. Ireland, H. Brinkmann, I.P. Newton, E. Batlle, P. Simon-Assmann, H. Clevers, I.S. Nathke, A.R. Clarke, D.J. Winton, Loss of Apc in vivo immediately perturbs Wnt signaling, differentiation, and migration, Genes Dev 18(12) (2004) 1385-90.

[3] N. Barker, J.H. van Es, J. Kuipers, P. Kujala, M. van den Born, M. Cozijnsen, A. Haegebarth, J. Korving, H. Begthel, P.J. Peters, H. Clevers, Identification of stem cells in small intestine and colon by marker gene Lgr5, Nature 449(7165) (2007) 1003-7.

[4] T. Sato, J.H. van Es, H.J. Snippert, D.E. Stange, R.G. Vries, M. van den Born, N. Barker, N.F. Shroyer, M. van de Wetering, H. Clevers, Paneth cells constitute the niche for Lgr5 stem cells in intestinal crypts, Nature 469(7330) (2011) 415-8.

[5] C.S. Potten, J.W. Wilson, C. Booth, Regulation and significance of apoptosis in the stem cells of the gastrointestinal epithelium, Stem Cells 15(2) (1997) 82-93.

[6] L. Liu, T.A. Rando, Manifestations and mechanisms of stem cell aging, J Cell Biol 193(2) (2011) 257-66.

[7] M. Koyama, F. Minale, J. Shum, N. Nishimura, C.B. Schaffer, J.R. Fetcho, A circuit motif in the zebrafish hindbrain for a two alternative behavioral choice to turn left or right, Elife 5 (2016).

[8] N. Nishimura, C.B. Schaffer, B. Friedman, P.S. Tsai, P.D. Lyden, D. Kleinfeld, Targeted insult to subsurface cortical blood vessels using ultrashort laser pulses: three models of stroke, Nature methods 3(2) (2006) 99-108.

[9] H. Tian, B. Biehs, S. Warming, K.G. Leong, L. Rangell, O.D. Klein, F.J. de Sauvage, A reserve stem cell population in small intestine renders Lgr5-positive cells dispensable, Nature 478(7368) (2011) 255-9.

[10] C. Metcalfe, N.M. Kljavin, R. Ybarra, F.J. de Sauvage, Lgr5+ stem cells are indispensable for radiation-induced intestinal regeneration, Cell Stem Cell 14(2) (2014) 149-59.

[11] N. Rakhilin, B. Barth, J. Choi, N.L. Munoz, S. Kulkarni, J.S. Jones, D.M. Small, Y.T. Cheng, Y. Cao, C. LaVinka, E. Kan, X. Dong, M. Spencer, P. Pasricha, N. Nishimura, X. Shen, Simultaneous optical and electrical in vivo analysis of the enteric nervous system, Nature communications 7 (2016) 11800.

[12] L. Ritsma, E.J. Steller, E. Beerling, C.J. Loomans, A. Zomer, C. Gerlach, N. Vrisekoop, D. Seinstra, L. van Gurp, R. Schafer, D.A. Raats, A. de Graaff, T.N. Schumacher, E.J. de Koning, I.H. Rinkes, O. Kranenburg, J. van Rheenen, Intravital microscopy through an abdominal imaging window reveals a pre-micrometastasis stage during liver metastasis, Sci Transl Med 4(158) (2012) 158ra145.

[13] C.B. Schaffer, A. Brodeur, E. Mazur, Laser-induced breakdown and damage in bulk transparent materials induced by tightly focused femtosecond laser pulses, Measurement Science And Technology 12(11) (2001) 1784-1794.

[14] A. Vogel, V. Venugopalan, Mechanisms of pulsed laser ablation of biological tissues, Chem Rev 103 (2003) 577-644.
[15] S.W. Chu, S.P. Tai, C.L. Ho, C.H. Lin, C.K. Sun, High-resolution simultaneous three-photon fluorescence and third-harmonic-generation microscopy, Microsc Res Tech 66(4) (2005) 193-7.
[16] M.J. Farrar, F.W. Wise, J.R. Fetcho, C.B. Schaffer, In vivo imaging of myelin in the vertebrate central nervous system using third harmonic generation microscopy, Biophys J 100(5) (2011) 1362-71.
[17] N.G. Horton, K. Wang, D. Kobat, C.G. Clark, F.W. Wise, C.B. Schaffer, C. Xu, In vivo three-photon microscopy of subcortical structures within an intact mouse brain, Nat Photonics 7(3) (2013).
[18] C.H. Wu, T.D. Wang, C.H. Hsieh, S.H. Huang, J.W. Lin, S.C. Hsu, H.T. Wu, Y.M. Wu, T.M. Liu, Imaging Cytometry of Human Leukocytes with Third Harmonic Generation Microscopy, Sci Rep 6 (2016) 37210.
[19] D.M. Small, J.S. Jones, Tendler, II, P.E. Miller, A. Ghetti, N. Nishimura, Label-free imaging of atherosclerotic plaques using third-harmonic generation microscopy, Biomed Opt Express 9(1) (2018) 214-229.
[20] K.Y. Chen, T. Srinivasan, K.L. Tung, J.M. Belmonte, L. Wang, P.K.L. Murthy, J. Choi, N. Rakhilin, S. King, A.K. Varanko, M. Witherspoon, N. Nishimura, J.A. Glazier, S.M. Lipkin, P. Bu, X. Shen, A Notch positive feedback in the intestinal stem cell niche is essential for stem cell self-renewal, Mol Syst Biol 13(4) (2017) 927.
[21] G.J.C. Wilde, L.E. Sundstrm, F. Iannotti, Propidium iodide in vivo: an early marker of neuronal damage in rat hippocampus, Neuroscience Letters 180(2) (1994) 223–226.
[22] M. Maekawa, T. Ishizaki, S. Boku, N. Watanabe, A. Fujita, A. Iwamatsu, T. Obinata, K. Ohashi, K. Mizuno, S. Narumiya, Signaling from rho to the actin cytoskeleton through protein kinases ROCK and LIM-kinase, Science 285(5429) (1999) 895-898.
[23] M.J. Peffers, K. Goljanek-Whysall, J. Collins, Y. Fang, M. Rushton, J. Loughlin, C. Proctor, P.D. Clegg, Decoding the Regulatory Landscape of Ageing in Musculoskeletal Engineered Tissues Using Genome-Wide DNA Methylation and RNASeq, PLoS One 11(8) (2016) e0160517.
[24] D.L. Jones, T.A. Rando, Emerging models and paradigms for stem cell ageing, Nat Cell Biol 13(5) (2011) 506-12.
[25] H.J. Snippert, L.G. van der Flier, T. Sato, J.H. van Es, M. van den Born, C. Kroon-Veenboer, N. Barker, A.M. Klein, J. van Rheenen, B.D. Simons, H. Clevers, Intestinal crypt homeostasis results from neutral competition between symmetrically dividing Lgr5 stem cells, Cell 143(1) (2010) 134-44.
[26] T.H. Kim, S. Escudero, R.A. Shivdasani, Intact function of Lgr5 receptor-expressing intestinal stem cells in the absence of Paneth cells, Proc Natl Acad Sci U S A 109(10) (2012) 3932-7.
[27] A. Durand, B. Donahue, G. Peignon, F. Letourneur, N. Cagnard, C. Slomianny, C. Perret, N.F. Shroyer, B. Romagnolo, Functional intestinal stem cells after Paneth cell ablation induced by the loss of transcription factor Math1 (Atoh1), Proc Natl Acad Sci U S A 109(23) (2012) 8965-70.

[28] J.M. Russo, P. Florian, L. Shen, W.V. Graham, M.S. Tretiakova, A.H. Gitter, R.J. Mrsny, J.R. Turner, Distinct temporal-spatial roles for rho kinase and myosin light chain kinase in epithelial purse-string wound closure, Gastroenterology 128(4) (2005) 987-1001.
[29] L. Herrgen, O.P. Voss, C.J. Akerman, Calcium-dependent neuroepithelial contractions expel damaged cells from the developing brain, Dev Cell 31(5) (2014) 599-613.
[30] J. Rosenblatt, M.C. Raff, L.P. Cramer, An epithelial cell destined for apoptosis signals its neighbors to extrude it by an actin- and myosin-dependent mechanism, Curr Biol 11(23) (2001) 1847-1857.
[31] C. Meghana, N. Ramdas, F.M. Hameed, M. Rao, G.V. Shivashankar, M. Narasimha, Integrin adhesion drives the emergent polarization of active cytoskeletal stresses to pattern cell delamination, Proc Natl Acad Sci 108(22) (2012) 9107-9112.
[32] J.H. van Es, M.E. van Gijn, O. Riccio, M. van den Born, M. Vooijs, H. Begthel, M. Cozijnsen, S. Robine, D.J. Winton, F. Radtke, H. Clevers, Notch/gamma-secretase inhibition turns proliferative cells in intestinal crypts and adenomas into goblet cells, Nature 435(7044) (2005) 959-963.
[33] T. Reya, H. Clevers, Wnt signalling in stem cells and cancer, Nature 434(7035) (2005) 843-50.
[34] K.S. Yan, O. Gevaert, G.X.Y. Zheng, B. Anchang, C.S. Probert, K.A. Larkin, P.S. Davies, Z.F. Cheng, J.S. Kaddis, A. Han, K. Roelf, R.I. Calderon, E. Cynn, X. Hu, K. Mandleywala, J. Wilhelmy, S.M. Grimes, D.C. Corney, S.C. Boutet, J.M. Terry, P. Belgrader, S.B. Ziraldo, T.S. Mikkelsen, F. Wang, R.J. von Furstenberg, N.R. Smith, P. Chandrakesan, R. May, M.A.S. Chrissy, R. Jain, C.A. Cartwright, J.C. Niland, Y.K. Hong, J. Carrington, D.T. Breault, J. Epstein, C.W. Houchen, J.P. Lynch, M.G. Martin, S.K. Plevritis, C. Curtis, H.P. Ji, L. Li, S.J. Henning, M.H. Wong, C.J. Kuo, Intestinal Enteroendocrine Lineage Cells Possess Homeostatic and Injury-Inducible Stem Cell Activity, Cell stem cell 21(1) (2017) 78-90 e6.
[35] M.F. Olson, Applications for ROCK kinase inhibition, Curr Opin Cell Biol 20(2) (2008) 242-8.
[36] X.J. Qi, W. Ning, F. Xu, H.X. Dang, F. Fang, J. Li, Fasudil, an inhibitor of Rho-associated coiled-coil kinase, attenuates hyperoxia-induced pulmonary fibrosis in neonatal rats, Int J Clin Exp Pathol 8(10) (2015) 12140-50.
[37] Y. Kangawa, T. Yoshida, Y. Yonezawa, K. Maruyama, S.M. Hayashi, M. Shibutani, Suppression of epithelial restitution using an inhibitor against Rho-associated coiled-coil containing protein kinase aggravates colitis through reduced epithelial expression of A-kinase anchor protein 13, Exp Toxicol Pathol 69(8) (2017) 557-563.
[38] A.M. Marchiando, L. Shen, W.V. Graham, K.L. Edelblum, C.A. Duckworth, Y. Guan, M.H. Montrose, J.R. Turner, A.J. Watson, The epithelial barrier is maintained by in vivo tight junction expansion during pathologic intestinal epithelial shedding, Gastroenterology 140(4) (2011) 1208-1218 e1-2.
[39] C.S. Potten, The Significance of Spontaneous and Induced Apoptosis in the Gastrointestinal-Tract of Mice, Cancer Metast Rev 11(2) (1992) 179-195.
[40] A.G. Renehan, S.P. Bach, C.S. Potten, The relevance of apoptosis for cellular homeostasis and tumorigenesis in the intestine, Can J Gastroenterol 15(3) (2001) 166-76.

[41] M. Raetz, S.H. Hwang, C.L. Wilhelm, D. Kirkland, A. Benson, C.R. Sturge, J. Mirpuri, S. Vaishnava, B. Hou, A.L. Defranco, C.J. Gilpin, L.V. Hooper, F. Yarovinsky, Parasite-induced TH1 cells and intestinal dysbiosis cooperate in IFN-gamma-dependent elimination of Paneth cells, Nat Immunol 14(2) (2013) 136-42.
[42] M. Sawada, K. Takahashi, S. Sawada, O. Midorikawa, Selective killing of Paneth cells by intravenous administration of dithizone in rats, Int J Exp Path 72 (1991) 407-421.
[43] H.F. Farin, W.R. Karthaus, P. Kujala, M. Rakhshandehroo, G. Schwank, R.G.J. Vries, E. Kalkhoven, E.E.S. Nieuwenhuis, H. Clevers, Paneth cell extrusion and release of antimicrobial products is directly controlled by immune cell-derived IFN-gamma, J Exp Med 211(7) (2014) 1388-1400.
[44] L.E. Munoz, K. Lauber, M. Schiller, A.A. Manfredi, M. Herrmann, The role of defective clearance of apoptotic cells in systemic autoimmunity, Nat Rev Rheumatol 6(5) (2010) 280-9.
[45] L. Ritsma, S.I.J. Ellenbroek, A. Zomer, H.J. Snippert, F.J. de Sauvage, B.D. Simons, H. Clevers, J. van Rheenen, Intestinal crypt homeostasis revealed at single-stem-cell level by in vivo live imaging, Nature 507(7492) (2014) 362-365.
[46] C. Lopez-Otin, M.A. Blasco, L. Partridge, M. Serrano, G. Kroemer, The hallmarks of aging, Cell 153(6) (2013) 1194-217.
[47] P. Hook, V. Sriramoju, L. Larsson, Effects of aging on actin sliding speed on myosin from single skeletal muscle cells of mice, rats, and humans, Am J Physiol Cell Physiol 280(4) (2001) C782-8.
[48] C. Gao, J. Pedersen, L. Arendt-Nielsen, A.M. Drewes, H. Gregersen, Age-related variation in mechanical and sensory function of the human duodenum, The Journal of Applied Research 4(1) (2004) 99-110.
[49] J. Zhao, H. Gregersen, Morphometric and biomechanical remodeling of the small intestine during aging in rats, J Biomech 48(16) (2015) 4271-8.
[50] J. Huynh, N. Nishimura, K. Rana, J.M. Peloquin, J.P. Califano, C.R. Montague, M.R. King, C.B. Schaffer, C.A. Reinhart-King, Age-related intimal stiffening enhances endothelial permeability and leukocyte transmigration, Science translational medicine 3(112) (2011) 112ra122.
[51] Schneider, C. A., Rasband, W. S. & Eliceiri, K. W. NIH Image to ImageJ: 25 years of image analysis. Nature methods 9, 671–675 (2012).
[52] P. Thevenaz, U.E. Ruttimann, M. Unser, A pyramid approach to subpixel registration based on intensity, IEEE Trans Image Process 7(1) (1998) 27-41.

CHAPTER FIVE

UNDERSTANDING DYNAMIC PHYSIOLOGY OF THE STEM CELL NICHE

In the previous chapter, we introduced a new type of behavior of Lgr5+ ISCs which we discovered. Here, we want to share some exploratory, preliminary results that we are currently investigating. We found several interesting results, and these will serve as a basis to investigate new biological questions in stem cell biology.

5.1 Cellular interactions between stem cells and surrounding niche cells

5.1.1 Resident macrophages in the small intestinal epithelium

As briefly mentioned, there are variety of cell types surrounding crypts providing niche factors that maintain the local microenvironment of the stem cell niche. Immune cells are mostly found at the lamina propria, a layer surrounding the crypts, and contribute to keeping the epithelial barrier function intact [1]. Using multiphoton microscopy through implanted abdominal windows, we observed that cells expressing green fluorescent protein driven by the Cx3Cr1 promoter, expressed in resident macrophages and dendritic cells [2], are found in close proximity of the crypt wall and surround each crypt (Fig. 5.1). Macrophages are the first responders to injury in a tissue or cell death in other organs such as the brain where they and rapidly extend processes and migrate towards laser-induced lesions [3]. Therefore, we wanted to examine whether resident macrophages surrounding crypts are involved in recovery process as well.

5.1.2 Response of Cx3Cr1^{+}-GFP macrophages to injury inside of the crypts is limited

We ablated multiple cells inside crypts and monitored the resulting dynamics in the macrophages and Paneth cells (visualized by third harmonic generation). Surprisingly, macrophages did not show remarkable changes either in their organization or in their density (Fig. 5.2a). An autofluorescence region appeared at the ablation site in the Cx3Cr1^{+}-GFP channel, consistent with other studies, but this is not related to the GFP in the surrounding macrophages. Even with increased levels of damage (more than 10 ablation locations at the crypt base), macrophages did not show substantial change in morphology. Both the cell bodies and the cell

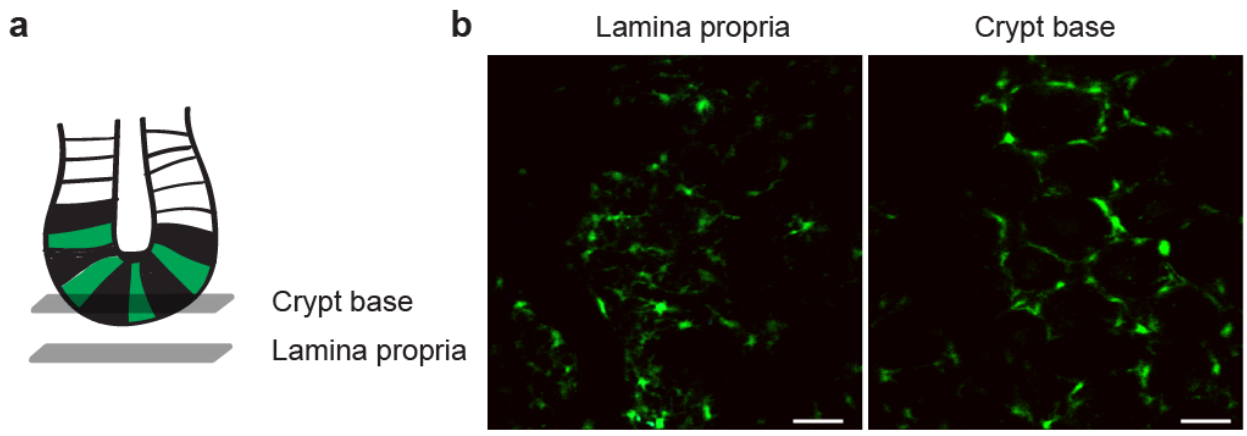

Figure 5.1 *In vivo* images of Cx3Cr1^{+}-GFP Macrophages
(a) A schematic shows the two different imaging planes. (b) Organization of Cx3Cr1^{+}-GFP cells at crypt base and lamina propria. Scale bar: 30 μm.

processes remained outside the crypt during the two-hour imaging period. In order to explore whether macrophages have an alternate response to damage occurring outside of the crypt, we induced a small region of damage at lamina propria ~10 μm outside a crypt. After a single ablation, we saw dramatic changes in the GFP-expressing cells, which increased in density around the ablated region between 10 to 60 minutes and then almost completely disappeared from the damaged area at two hours (Fig. 5.2b). We also found that round cells strongly expressing THG signal filled the area where GFP-expressing cells existed previous, a finding which needs further investigation.

Although it is still early to draw any conclusion from this preliminary result, we are interested in why the crypts seem to exclude an innate immune response even under conditions of injury. Based on these results, we will further investigate the roles of innate immune cells during recovery process.

5.2 Mechanistic study to understand molecular pathways that initiate recovery process

In our previous study, we identified that motility of stem cells plays a major role in the recovery process after crypt damage. The rapid migration of crypt base cells and peristaltic motion of crypt lumen require activation of the ROCK pathway. ROCK is a family member of small GTPases and can activate various downstream pathways involved in cytoskeletal organization [4]. YAP/TAZ, also known as co-effectors of hippo pathway, is one of the downstream molecules of the ROCK pathway, which can induce cytoskeletal remodeling. Activation of ROCK inhibits Last1/2 activity, which hinders translocation of YAP/TAZ to nucleus. Thus, ROCK activation

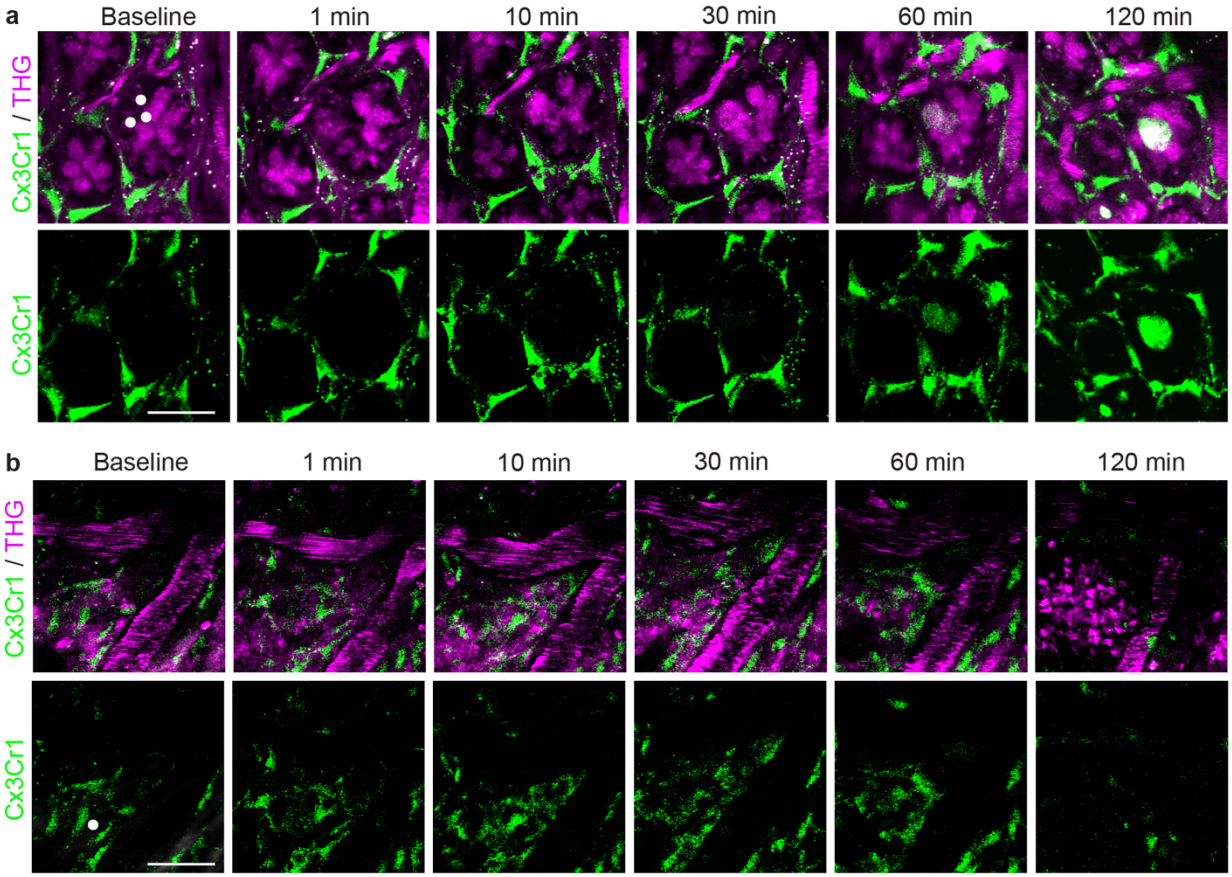

Figure 5.2 Resident macrophages surrounding crypts are merely responsive after small injury inside of the crypt. (a) Time-lapse images of macrophages after ablation at the base of the crypt. We used three-photon microscopy to generate THG from Paneth cells (magenta). Red blood cells in vessels can also be seen with THG (magenta). Green indicates $Cx3Cr1^{+}$ resident macrophages and autofluoresence due to laser damage. (b) Time-lapse images of macrophages after ablation at the lamina propria. Magenta indicates THG signal from cells inside and outside of vessels. At 120 minutes after ablation, we saw dramatic populational changes at the damaged area where $Cx3Cr1^{+}$ macrophages disappeared and THG-positive round-shaped cells appeared. Scale bar: 30 μm.

results in nuclear translocation of YAP/TAZ, which induces cytoskeletal rearrangement (Fig. 5.3) [5]. Therefore, we hypothesized that the YAP/TAZ could be a downstream signal to induce stem cell motility through ROCK activation. To test whether activation of YAP/TAZ is also necessary to trigger the recovery process, we used verteporfin, an inhibitor specifically blocking translocation of YAP/TAZ into a nucleus [5].

5.2.1 YAP/TAZ activation is required to induce stem cell motility

In order to investigate the role of YAP/TAZ during recovery process, the mouse was treated with verteporfin (100 mg/kg) via intra peritoneally. We performed single-point ablation 6 hours after treatment and found that the damaged cells were not removed from the crypt base within two hours. The surrounding cells did not migrate towards the damaged site, which suggests that YAP/TAZ inhibition impaired stem cell motion similar to ROCK inhibition (Fig. 5.4). With this preliminary data, we will further investigate the role of ROCK-YAP/TAZ pathway in recovery process by using *in vivo* and *ex vivo* assays.

5.3 Recovery process fully restores integrity of stem cell and epithelial function

Keeping the epithelium intact requires recovery of intact junctions between epithelial cells [6]. Therefore, we tested the functional integrity of the intestinal epithelium with a new assay of dye leakage. Despite the complete pattern recovery after a small injury, a question remains whether it is enough to recover the integrity of the epithelium barrier as well. Therefore, we decided to measure whether the crypt's barrier function is also restored with rapid rearrangement of niche

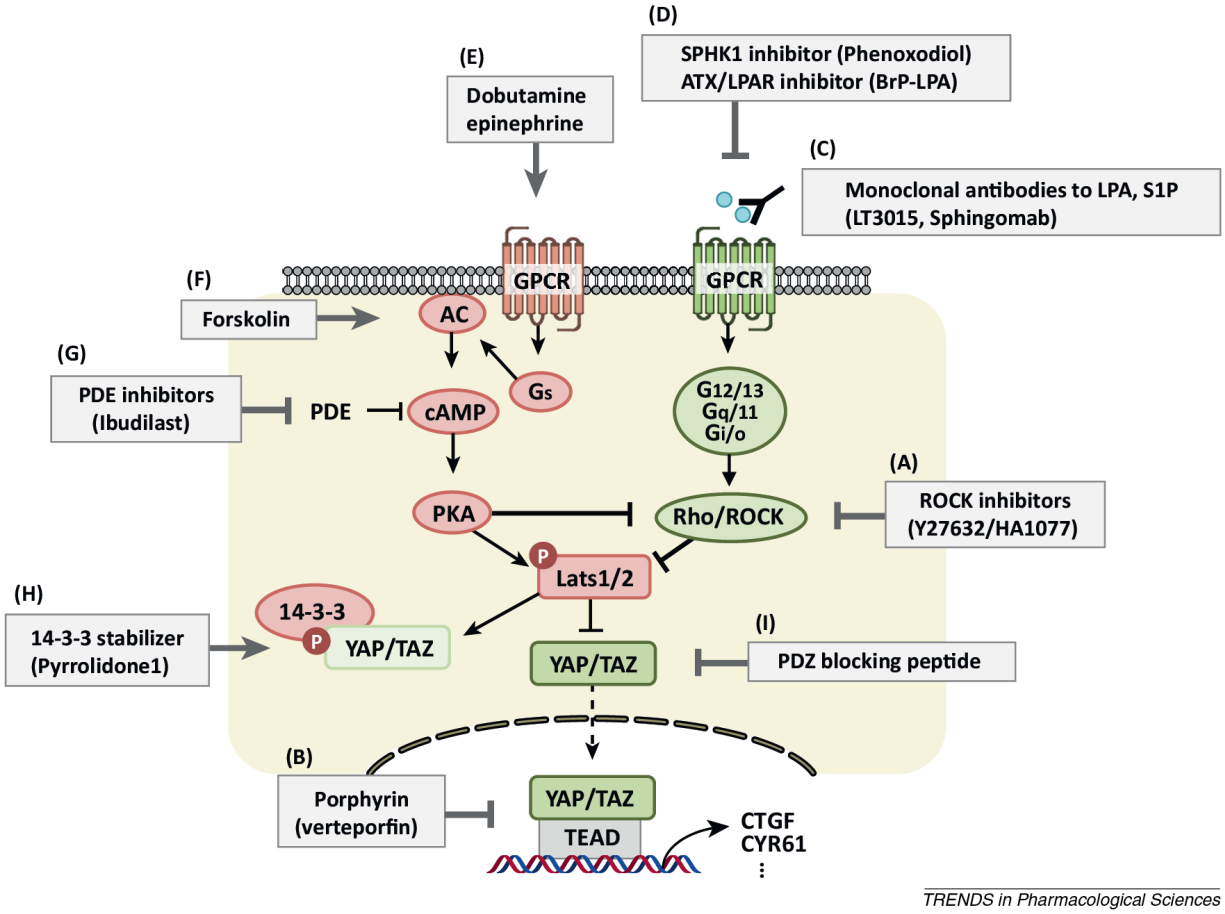

Figure 5.3 Schematic to show regulation of Hippo pathway.
Activation of Rho/ROCK acts as agonist of YAP/TAZ activity by inhibiting Lats1/2 activation. This figure is adapted from a reference [5].

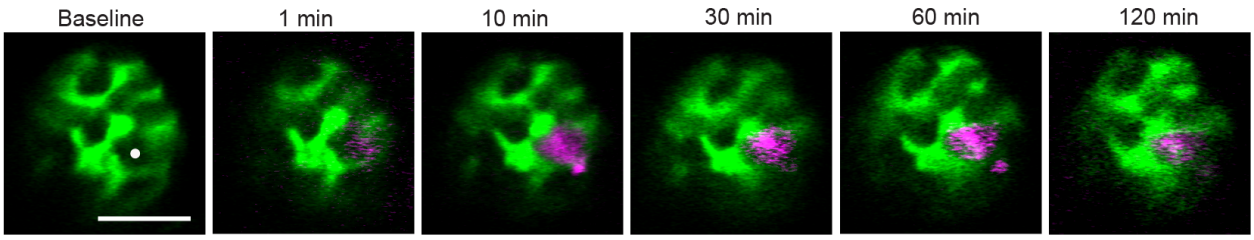

Figure 5.4 Activation of YAP/TAZ is required to induce recovery process. Time-lapse images after laser ablation. White dot indicates the focus of laser ablation. To track a damaged cell, PI (magenta) was injected retro-orbitally. Inhibition of YAP/TAZ pathway resulted in inability of damage removal from the crypt, which detected for extended period of time. Scale bar: 30 μm.

cells. By injecting fluorescent dye conjugated with a small size dextran (10 kD) into the intestinal lumen directly, we can follow how the dye diffuses into the crypt as a measure of the integrity of the epithelium. In control crypts, no dye is seen within the crypt 60 minutes after injection. After ablation, we found that blue dye leaked into the damaged area inside the crypt base and co-localized with propidium iodide (PI)-labeled dying cells, which suggests that laser ablation perturbed the barrier function (Fig. 5.5a). However, after 60 minutes when the cellular debris had been pushed out from the crypt by the neighboring cell migration, we observed that the infused dye was also gone from the crypt base and no more dye was detected inside the crypt base. Similar responses were detected after ablation at the upper layer of the crypt, suggesting that rapid migration of surrounding cells not only recovers niche patterning but restores barrier function as well (Fig. 5.5b). Future experiments can test how this barrier integrity is modified when cell motility is inhibited.

5.4 Stability of stem cell phenotype

Our finding suggests that rapid migration of neighboring cells is critical to recovery of the alternating pattern of Paneth cells and stem cells. Previously, we observed that GFP labeling remained bright during imaging over several hours after ablation. A question raised about this observation was whether GFP in Lgr5+ ISCs is an assay of Lgr5 levels and therefore, stemness. In other words, we wondered whether GFP expression is sensitive enough to represent stem cell identity after ablation. Therefore, we perturbed one of the niche factors, Notch signaling, which is critical to maintaining stemness by treating with dibenzazipene (DBZ), a chemical inhibitor that blocks Notch activity. Over two hours, crypts treated with DBZ showed loss of GFP labeling and

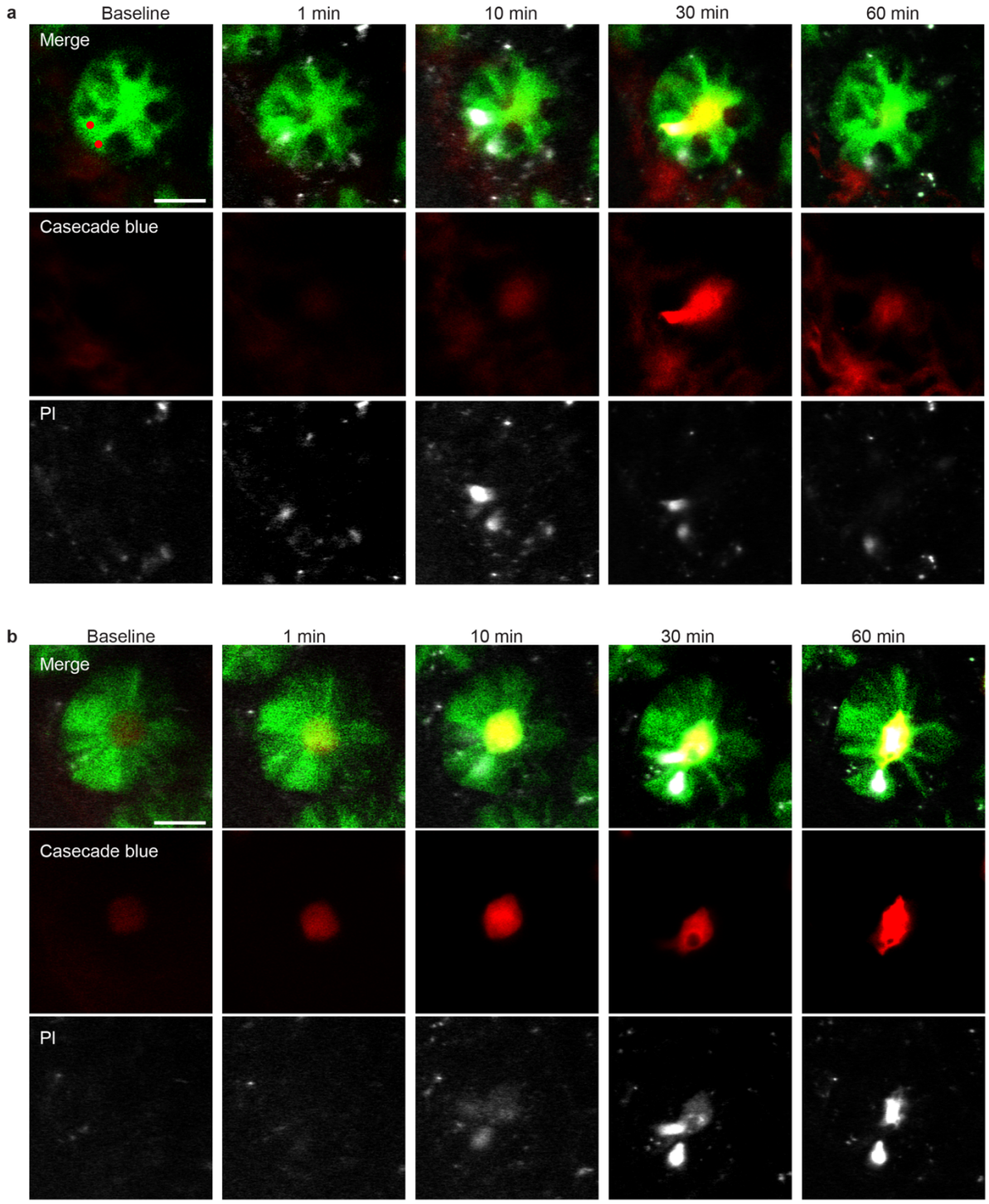

Figure 5.5 Rapid pattern recovery also helps to restore intact barrier function. Time-lapse images after laser ablation at the crypt base (a) and at cells in the upper layer (b) to investigate barrier function of intestinal epithelium. Cascade blue (red) injected into intestinal lumen leaked through ablated area into crypt base after ablation, and then cleared along with clearance of cellular debris. Propidium iodide (PI) in which shows damaged cells. Scale bar: 30 μm.

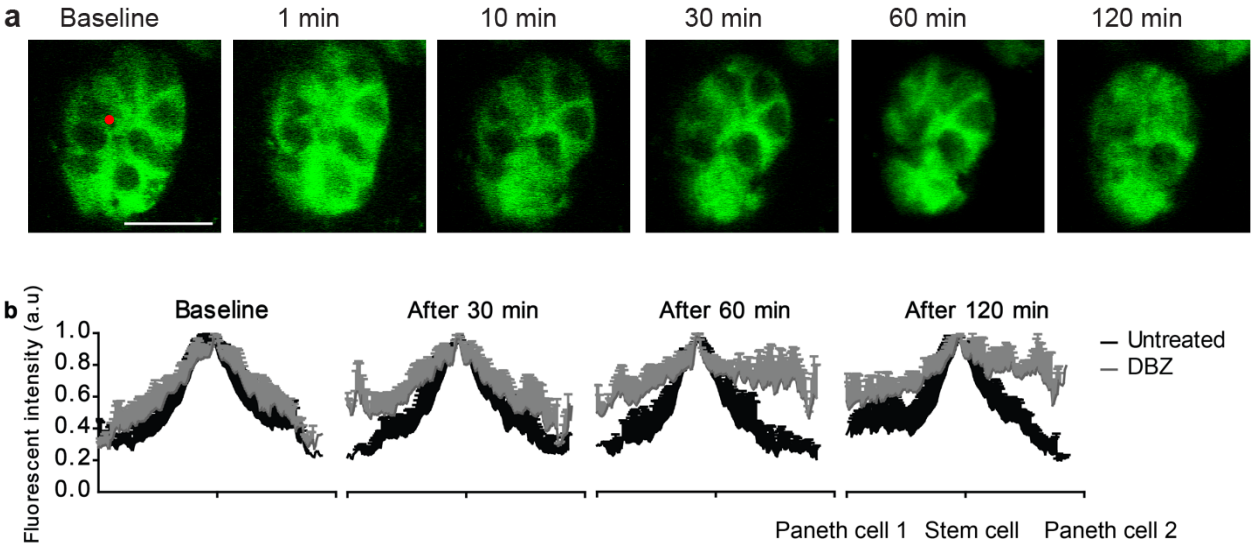

Figure 5.6 Stem cell phenotype remains stable during recovery process. (a) Time-lapse images of a crypt treated with a Notch inhibitor, dibenzazipene (DBZ). Red dot indicates the area targeted by ablation laser. Scale bar: 30 μm. (b) Measurement of intensity across the two Paneth cells in control and DBZ treated group. Straight line in between Paneth cells near the ablation area showed intensity changes over time after ablation (Untreated: black line, DBZ treated: gray line)

the clear distinction between Lgr5+ ISCs and Paneth cells, which is consistent with the loss of stem cell identity (Fig. 5.6a). We quantitatively measure the intensity change from each cell type and found when stem cell interfered with Notch signaling, the crypts were not able to recover from the damage and showed loss of stem cell phenotype quickly, as reported by $Lgr5^{+}$ GFP fluorescence changes, while control crypts treated with saline still showed clear distinction between stem cells and Paneth cells before and after damage (Fig. 5.6b). This result suggests that recovery process does not induce phenotypic change of the stem cells. This type of measurement is not a direct measurement of either stemness or Lgr5 expression, and this result would need to be followed up by other methods. However, it provides indirect support of the hypothesis that stem cell phenotype is not perturbed by small injuries.

5.5 Conclusion

Here, we discuss several future directions to study physiology of adult stem cells in the crypts based on our initial findings. The preliminary result from the study of epithelial barrier function suggests that rapid rearrangement of crypt cells not only restores the alternating pattern but also recovers the barrier function after a small injury. The ability to exclude and limit the macrophage response to crypt injury will provide information whether intestinal crypt has alternative defensive system different from general inflammation response. We also investigated signaling pathways responsible for inducing cellular motions and our preliminary data suggests YAP/TAZ protein may be involved in the recovery process. Although we need to scrutinize each aspect in depth, our preliminary data opens up diverse possibilities for future directions.

5.6 Methods

5.6.1 Animal models

To visualize stem cells in the crypt we used *Lgr5* $^{tm1(cre/ERT2)Cle}$*/J* mice (Lgr5-GFP) bred at Cornell University from breeders originally purchased from the Jackson Laboratory (Stock No. 008875). To visualize immune cells, breeders were purchased from The Jackson Laboratory (CX3CR1-GFP, Stock No. 8451). All animal experiments were conducted in strict accordance with the recommendations in the Guide for the Care and Use of Laboratory Animals published by National Institutes of Health, and all animal procedures were approved by the Cornell University Institutional Animal Care and Use Committee (protocol numbers 2009-0043 and 2015-0029).

5.6.2 Abdominal window preparation

Mice were anesthetized with 4% isoflurane in oxygen and maintained at ~2%. At the beginning of the surgery, animals received an anticholinergic, 0.05 mg per 100 g of mouse weight of glycopyrrolate or 0.005 mg/100 g of atropine subcutaneously, to assist in keeping the airways clear of fluid build-up. Body temperature was kept at 37 °C using a heating blanket controlled by a rectal thermometer. All areas to be incised were shaved and cleaned with 70% ethanol, and betadine, and were numbed with a 100 μL subcutaneous injection of 0.125% bupivacaine. Eyes were covered with veterinary eye ointment to prevent drying. The animals were hydrated with subcutaneous injections of 5% glucose in saline for isotonic fluid replacement. Abdominal skin was removed in a circular shape to fit a titanium window frame (Brain Titanium Chamber Kit, 12 mm in inner diameter, APJ trading, CA). The frame was put on top of the abdominal muscle. The outer edge of the frame was covered by skin and secured with cyanoacrylate adhesive (Loctite 406,

Henkel). The abdominal muscles within the inner circle were incised with scissors to expose the small intestine. Custom-designed scaffold to stabilize the intestine were 3D-printed (UPrint) out of ABSplus. The insert was placed under the small intestine so that a portion of the small intestine looped around the center post, entering and exiting the insert at the same gap between the supports. The insert was sutured to the skin outside of the frame by threading sutures through the holes in the four supports. The window was closed with a 12-mm diameter cover glass held on by the frame's retaining ring. Window and insert was placed in the abdominal area 1-1.5 cm below the rib cage. Dexamethasone (0.025 mg/100 g) and ketoprofen (0.5 mg/100 g) were injected intraperitoneally to help recovery after surgery and then daily for 2 days. Animals were returned to their home cage after recovery. Imaging was performed at least 24-48 hours after implantation to allow the position of the intestine in the window to settle and to minimize the effects of the surgery.

5.6.3 *In vivo* two-photon and three-photon excited fluorescence microscopy

Animals with abdominal window were imaged using a custom-built 2PEFM. All animals were anesthetized with isoflurane (1-2% in medical air) which was adjusted to maintain constant breathing rate during imaging time. To visualize vasculature, 50 µl of 2.5% Texas Red dextran (Molecular weight: 70,000; Thermo Fisher Scientific, NY) in saline was injected retro-orbitally. Images were acquired using a Ti:Sapphire laser (Chameleon; Coherent, Santa Clara, CA) with wavelength centered at 880 nm for two-photon excitation and an optical parametric amplifier (OPA) (Coherent, Opera-F) seeded by a diode-pumped femtosecond laser (60 µJ/pulse at 1 MHz; Coherent, Monaco) with wavelength centered at 1,300 nm for three-photon excitation and third

harmonic generation. Either a 20x, 1.0-NA (Zeiss, Thornwood, NY) or 25x, 1.05-NA (Olympus) water-immersion microscope objective was used for imaging and ablation. A 4X, 0.28-NA objective lens (Zeiss, Thornwood, NY) was used for low-resolution mapping. A 494-nm bandpass filter with 41-nm bandwidth, a 641-nm bandpass filter with a 75-nm bandwidth, and a 433-nm bandpass filter with 24-nm bandwidth was used for green fluorescent protein (GFP), Texas Red dextran dye, and THG, respectively. For Hoechst-labeled crypt imaging, we tuned the Ti:Sapphire laser to 830 nm. A 458-nm bandpass filter was used to detect Hoechst. Image stacks were acquired before and after laser ablation at 1.44 frames/s, with 1-μm spacing in the axial direction.

5.6.4 Disruption of cellular contact using femtosecond laser photodisruption

Selective disruption of cells was performed using a low-repetition-rate, high-pulse-energy Ti:Sapphire regenerative amplifier with 50-fs pulse duration, 1-kHz repetition rate, and 800-nm central wavelength (Legend-USP; Coherent, Santa Clara, CA). A polarizing beamsplitter cube was used to introduce this beam into the 2PEF microscope so that the pulses were focused at the center of the imaging field and in the 2PEF imaging plane, enabling real-time monitoring (Fig. 4.1c). Laser energy incident on the cells was controlled by neutral density (ND) filters, and a fast, mechanical shutter limited the number of pulses (2-5) incident on each cell. We started ablation with lower power by using highest ND filter, and then gradually increased the power until we saw the formation of a small hole in the cytoplasm (Suppl. Fig. 4.1c). Incident laser energy to remove a single cell was typically about 50 nJ per pulse and did not exceeded 100 nJ.

5.6.5 Addition of chemical compounds

To inhibit YAP/TAZ protein signaling, verteporfin (Sigma Aldrich, St. Luis, MO; 100 mg/kg mouse weight in 10 % DMSO in saline) was injected under the window 6 hours before start of imaging. 10 % DMSO in Saline (0.9 %) (Phoenix Pharmaceutics, Burlingame, CA) was injected for the sham-treated group. To label damaged cells, propidium iodide (Cayman Chemical Company, Ann Arbor, MI; 100 µl of 1 mg/ml in PBS) was injected retro-orbitally. DBZ (Syncom, Netherlands), a small molecule gamma-secretase inhibitor, was dissolved in DMSO at final concentration of 30 µM, and locally injected into the submucosal layer of the small intestine through the implanted abdominal window on mice (15 µM/kg) 2 hours before imaging.

5.6.6 Measurement of fluorescence intensity

To assess stability of Lgr5-GFP signals, we used processed and projected image (2-5 frames in average). Mean fluorescence intensity was measured from manually selected areas from same Lgr5-ISC and Paneth cell near the ablation at each time point. The analysis regions were selected by a user blinded to the treatment (control versus DBZ) and the timing of each image to reduce possible bias.

5.6.7 Image processing

All images were processed using ImageJ. Frames that contained abrupt movement from respiration or peristalsis were deleted manually (approximately 20% of frames). To enhance signal/noise ratio, we applied a median filter with 1~2-pixel radius depending on the noise. Images within the stack was registered using a macro function called Stackreg [7]. For quantitative analysis, we used either an average projection of one to five frames at the base of the crypt or at

an upper layer about 15 μm closer to the villi. This upper layer was at approximate at the +3 cell position in the crypt[8]. Unless otherwise noted, displayed images are average projections of five frames and intensity adjustment was limited to linear scaling.

REFERENCES

[1] C. Varol, E. Zigmond, S. Jung, Securing the immune tightrope: mononuclear phagocytes in the intestinal lamina propria, Nat Rev Immunol 10(6) (2010) 415-26.

[2] S. Jung, J. Aliberti, P. Graemmel, M.J. Sunshine, G.W. Kreutzberg, A. Sher, D.R. Littman, Analysis of fractalkine receptor CX(3)CR1 function by targeted deletion and green fluorescent protein reporter gene insertion, Mol Cell Biol 20(11) (2000) 4106-14.

[3] S.J. Ahn, J. Anrather, N. Nishimura, C.B. Schaffer, Diverse Inflammatory Response After Cerebral Microbleeds Includes Coordinated Microglial Migration and Proliferation, Stroke 49(7) (2018) 1719-1726.

[4] M. Maekawa, T. Ishizaki, S. Boku, N. Watanabe, A. Fujita, A. Iwamatsu, T. Obinata, K. Ohashi, K. Mizuno, S. Narumiya, Signaling from Rho to the actin cytoskeleton through protein kinases ROCK and LIM-kinase, Science 285(5429) (1999) 895-8.

[5] H.W. Park, K.L. Guan, Regulation of the Hippo pathway and implications for anticancer drug development, Trends Pharmacol Sci 34(10) (2013) 581-9.

[6] L.W. Peterson, D. Artis, Intestinal epithelial cells: regulators of barrier function and immune homeostasis, Nat Rev Immunol 14(3) (2014) 141-53.

[7] P. Thevenaz, U.E. Ruttimann, M. Unser, A pyramid approach to subpixel registration based on intensity, IEEE Trans Image Process 7(1) (1998) 27-41.

[8] N. Barker, J.H. van Es, J. Kuipers, P. Kujala, M. van den Born, M. Cozijnsen, A. Haegebarth, J. Korving, H. Begthel, P.J. Peters, H. Clevers, Identification of stem cells in small intestine and colon by marker gene Lgr5, Nature 449(7165) (2007) 1003-7.

CHAPTER SIX

APPLICATION OF ABDOMINAL IMAGING WINDOW 1: OPTICAL STIMULATION AND RECORDING OF ENTERIC NEURON ACTIVITIES

In the chapter six and seven, I will introduce successful examples in which we applied the abdominal imaging window into other biological systems. Here, I will introduce the paper that I helped to publish in Nature Communication. In this paper, we modified abdominal imaging window for studying enteric nervous system and combined it with a graphene chip for optical and electric monitoring simultaneously. I helped to develop imaging platform, conducted chronic *in vivo* imaging and generated Figure 6.1.

6.1 Simultaneous optical and electrical *in vivo* analysis of the enteric nervous system

6.1.1 Abstract

The enteric nervous system (ENS) is a major division of the nervous system and vital to the gastrointestinal (GI) tract and its communication with the rest of the body. Unlike the brain and spinal cord, relatively little is known about the ENS in part because of the inability to directly monitor its activity in live animals. Here, we integrate a transparent graphene sensor with a customized abdominal window for simultaneous optical and electrical recording of the ENS *in vivo*. The implanted device captures ENS responses to neurotransmitters, drugs and optogenetic manipulation in real time.

6.1.2 Introduction

The enteric nervous system (ENS) contains the largest population of neurons in the peripheral nervous system, five times the amount in the spinal cord, and is often referred to as the 'second brain' due to its autonomous functions [1]. Organized into two types of ganglia, the myenteric and submucosal plexuses, the ENS is composed of motor neurons, sensory neurons and interneurons, and it is responsible for regulating vital functions such as gut motility and homeostasis [2, 3]. Damage to the ENS is associated with inflammatory bowel disease, irritable bowel syndrome and other functional GI disorders [4–6], which affect one quarter of the world's population and result in over 21.7 million hospitalizations and $141.8 billion in costs each year [7, 8]. ENS dysfunction often accompanies systemic conditions such as obesity and diabetes, and emerging evidence suggests a link between Parkinson's disease and the ENS [9–11].

Compared with the central nervous system, less is known about the ENS circuitry and its electrophysiological dynamics. For example, although ENS dysfunction is known to be associated with diseases like functional GI disorders, the exact electrophysiology is less clear [12, 13]. As opposed to the brain and spinal cord, which can be imaged via cranial and spinal windows and recorded via implantable electrodes [14–16], a major limitation in deciphering the ENS circuitry is our inability to optically image or electrically record ENS activities in live animals. Particular challenges for ENS recording include: the peristatic movements of the intestine, high background noise associated with surrounding longitudinal and circular muscles, lack of a fixed surface (for example, the skull or spine) to stabilize the device and maintain good contact, and the highly immunogenic gastrointestinal (GI) environment that interferes with ENS activities (in contrast, the central nervous system is much more immune tolerant towards foreign substrates) [17–19]. Gut movement also makes it extremely challenging to track the same groups of enteric neurons over multiple imaging sessions. Furthermore, given our limited knowledge about the ENS electrophysiology and high background noise, it is important to develop capabilities of simultaneous optical/electrical recording to take advantage of available transgenic reporter mice to validate and interpret recorded data.

The ENS has been imaged previously in an acute setup, where the intestine was brought out of the abdominal cavity, and the mouse was killed after the imaging session [20]. This method has several limitations if being applied to ENS recording: (i) the external environment and stretching the intestine out of the abdomen create artefacts due to ENS sensitivity to mechanical

and chemical stimuli; (ii) the imaging duration is limited and (iii) this setup does not allow chronic monitoring over an extended period, which is important for understanding ENS-related physiology in health and disease.

An intravital abdominal window was previously developed to image intestinal epithelial stem cells [21]. In this setup, the intestine was glued to the coverslip on the window, which was also kept in place by glue. However, the glue causes substantial local inflammation, which could interfere with ENS activity, and makes this approach ill-suited for studying ENS. Other factors also make this approach impractical for chronic (repeated) studies of the ENS. The tendency of coverslip breakage hinders repeated imaging sessions and prevents integration of electrical recording devices. Peristaltic movements often cause the intestine to break off from the glue and detach from the window. Adhering the intestine to the window can cause intestinal obstruction or chronic inflammation, leading to high-mortality rates, fibrosis and mucus buildup, preventing repeated measures of the ENS function over the course of the experiment. To overcome these limitations, a three-dimensional (3D)-printed insert is designed and surgically implanted into the animal to stabilize the intestine without blocking its motility functions. Through a customized abdominal intravital window, we manage to chronically image the same location in the mouse gut over several days and observe neuronal firing using the transgenic *Pirt-GCaMP3* mice. By further integrating a transparent graphene sensor into the window, we demonstrate the ability to perform concurrent optical and electrical recording of ENS activity, with high spatiotemporal resolution to detect waveforms of single action potentials (APs) from individual enteric neurons. We use these novel capabilities to analyze the effects of various chemical and biomolecular stimuli and

optogenetic manipulations on the gut, showing that such *in vivo*, real-time detection methods provide unique information necessary for the understanding of gut functionality *in vivo*.

6.1.3 Results

6.1.3.1 *In vivo* imaging using abdominal window

We designed a customized window to overcome the limitations found in earlier window designs. We started by surgically inserting a window into the fascia and skin layer of the mouse abdomen. The window uses thermally resistant, borosilicate glass, which is also much less susceptible to damage and less likely to break than conventional glass coverslips. Below the window, a 3D-printed insert holds the intestine in place while providing support and prevent ischemia (Supplementary Fig. 6.1). Unlike a chemical adhesive, the implant is not adhered to the intestine, minimizing inflammation. Meanwhile, it can be tightened to reduce tissue movement without blocking proper digestion functions and peristalsis, extending the lifetime of the mouse. In other applications, such as intravital cranial and spinal windows, implants are placed at locations inaccessible to the mice, but abdominal windows are subject to constant scratching. We therefore developed a protocol using vet wrap to prevent the mouse from damaging the window, which substantially prolonged mouse survival and avoided inflammation. The mice implanted with the window consistently live up to 3 months, until they are killed for humane reasons.

We demonstrated that it is possible to image the ENS in vivo using this setup. *Wnt1-cre:tdTomato* mice were chronically imaged with inverted multiphoton microscopy (Fig. 6.1a). In this transgenic strain, enteric neurons and other neural crest progeny are labelled with tdTomato [22, 23]. The grid-like myenteric plexus formed by individual neurons is clearly visible through

the transplanted abdominal window. To track the same set of enteric neurons on different days, fluorescein isothiocyanate (FITC)-dextran was injected retro-orbitally into the mouse to stain the vasculature, which served as a reference roadmap to locate the same region of the ENS (Fig. 6.1b–e and Supplementary Fig. 6.2). During subsequent imaging sessions, we were able to identify the same neurons using this vasculature roadmap. The plexus and vasculature morphology remained largely unchanged 11 days after the implantation surgery.

6.1.3.2 Detection of ENS activity via graphene electrodes.

To perform simultaneous electrical recording, we needed to integrate electrodes onto the abdominal window. The electrical recording device needs to be: (i) transparent to allow imaging through the device, (ii) inert and biocompatible to minimize fibrosis and inflammation, (iii) highly sensitive to detect ENS APs from background noise and (iv) durable for long-term chronic monitoring. To meet these stringent requirements, we developed a graphene-based electrode array that can be integrated onto the abdominal window to measure electrical activities in the ENS.

Consisting of a carbon sheet one atom thick, graphene offers unique advantages as a transparent material with superb conductivity (zero bandgap), biocompatibility (an inert surface) and strength (Young's modulus higher than diamond and 207 times stronger than steel by weight) [24, 25]. The chip contains nine graphene electrodes, ranging from 50 μm by 50 μm to 500 μm by 500 μm. Graphene was grown on a copper substrate via a vertical cold-wall chemical vapour deposition system and was transferred onto a transparent quartz surface. Gold interconnects, 150 nm thick, were evaporated onto the surface and protected by insulating photoresist that left the contact pads exposed (Supplementary Fig. 6.3). To integrate the graphene sensor onto the

abdominal window for surgical implantation, a piece of borosilicate glass, containing eight via-holes, 250 μm diameter, was inserted into a titanium ring and fixed in place by a horseshoe spring. The graphene chip was then secured to the borosilicate glass using transparent, insulating epoxy. Wires were threaded through the glass and secured to the connection pads using silver epoxy. The glass via-holes and connection pads were sealed using transparent insulating epoxy to protect the connection (Supplementary Fig. 6.4). The integration of graphene sensor and abdominal window provides us with the capability of simultaneous optical imaging and electrical recording in live mice. We surgically implanted the device into *Pirt-GCaMP3* mice such that the customized 3D-insert held the small intestine in contact with the exposed graphene electrodes without disrupting digestive and motility functions (Fig. 6.2a–d).

Through the transparent graphene sensor, the inverted multiphoton microscope was able to track activation of individual neurons in the myenteric plexus, which were fluorescently labelled via their genetically encoded GCaMP3 indicator for Ca^{2+} ion flux [26] (Supplementary Fig. 6.5).

We then performed simultaneous optical and electrical recording to track activated neurons in the myenteric plexus of *Pirt-GCaMP3* mice. The timing of multiphoton microscopy and the electrical recording apparatus are synchronized by a timing gate. Bursts of activity in GCaMP3 fluorescence (measured by multiphoton microscopy) and in electrical potential (measured by the graphene sensor) maintained high synchrony *in vivo* (Fig. 6.2e). The synchrony between electrical recording and optical imaging validates the mutual dependence between electrical potential spikes and the GCaMP fluorescence associated with APs. The combined optical/electrical measurements confirmed that our integrated abdominal device was indeed capable of capturing ENS APs, which

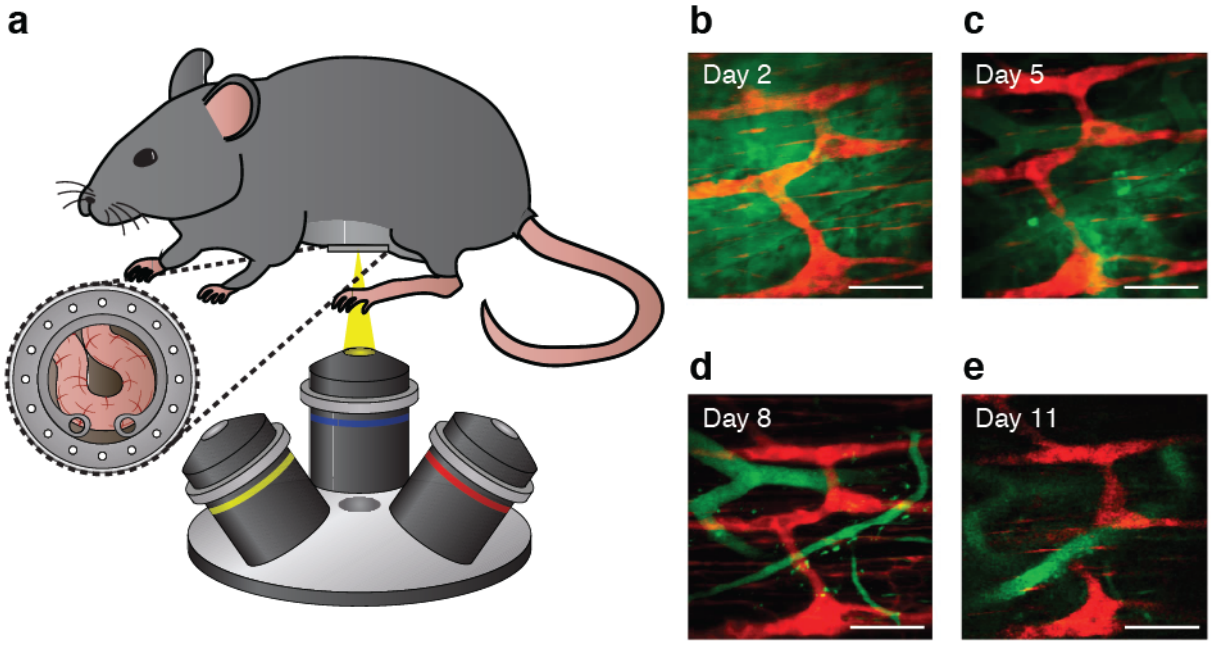

Figure 6.1. ***In vivo*** **chronic multiphoton microscopy of ENS with abdominal window.** (a) Schematic of in vivo multiphoton microscopy. (b–e) Days 2, 5,8 and 11 after abdominal surgery, respectively, of in vivo multiphoton imaging in *Wnt1-cre:tdTomato* mice. The ENS is labelled with tdTomato (red), and the vasculature is labelled with FITC-dextran (green). Scale bar, 100 μm.

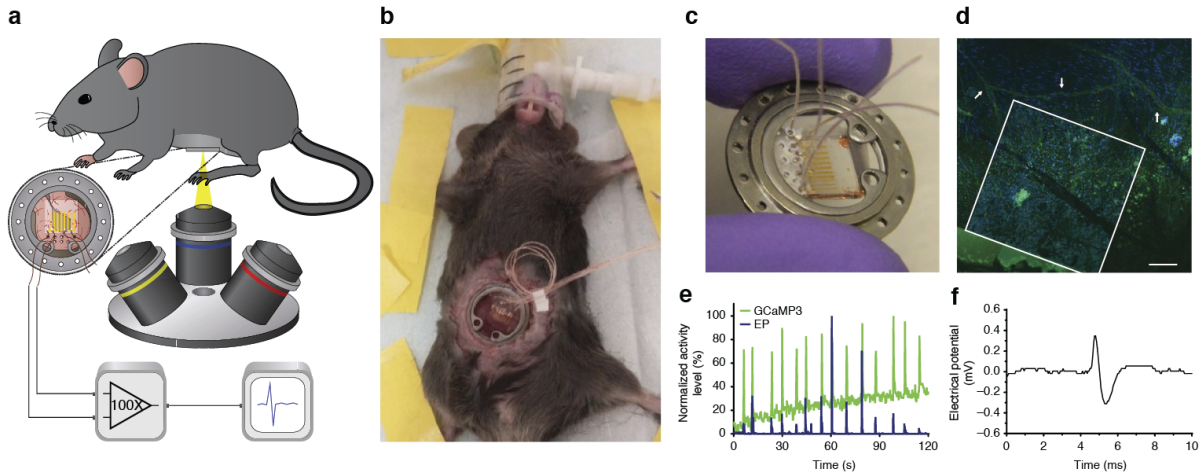

Figure 6.2. Simultaneous optical/electrical recording *in vivo* using integrated graphene sensor and abdominal window. (a) Schematic of *in vivo* optical/electrical recording. The graphene sensor is in close proximity to the small intestine, within the titanium ring of the surgical implant. (b) Mouse with integrated graphene sensor and abdominal window, several days after abdominal window implantation surgery. (c) The implantable abdominal window integrated with the graphene sensor. (d) Graphene electrode implanted in Pirt-GCaMP3 mouse. One graphene electrode (500 µm by 500 µm, white box) in contact with the surrounding nerves (green, identified with white arrows) and surrounding collagen tissue (blue). Scale bar, 100 µm. (e) Simultaneous multiphoton microscopy and electrical potential (EP) recording in vivo, in Pirt-GCaMP3 mouse. GCaMP3 fluorescence (green) and electrical potential (blue) are plotted, with absolute value of each signal normalized to 100%. (f) A high-temporal resolution waveform of an *in vivo* recorded AP.

is important given our limited knowledge about the ENS and the noise from the surrounding muscle layers. Compared with optical imaging, the sensitive graphene sensor provides much higher temporal resolution with greater signal-to-noise ratio, which allowed us to examine the detailed biphasic waveforms of ENS APs (Fig. 6.2f).

6.1.3.3 ENS activity in response to chemical stimulations.

ENS activities are spatiotemporally regulated by various neurotransmitters. For instance, the majority of the serotonin in the human body is produced in the GI tract to regulate intestinal movements [27, 28]. However, there was previously no means of studying real-time ENS response to these neurotransmitters *in vivo*. As proof-of-concept, we used the integrated device to study ENS response to acetylcholine and serotonin. Repeated optical imaging and electrical recording in distinct animals demonstrated that GCaMP3 fluorescence and electrical potential consistently followed the same trend upon delivery of acetylcholine or serotonin, consistent with activation of enteric neurons (Fig. 6.3a–d). The electrical potential measured by the graphene sensor showed a faster deactivation rate than GCaMP3 fluorescence, highlighting the relative slow response kinetics of GCaMP relative to electrical potential. Our data suggest that optical imaging with GCaMP3 technology provides better spatial resolution for tracking AP location, whereas electrical measurement provides higher temporal resolution to track AP dynamics. The integrated device combines both to provide a more comprehensive picture of ENS spatiotemporal activities in real time in live animals.

There are a range of Food and Drug Administration-approved small-molecule drugs that act via acetylcholine and serotonin receptors. Bethanechol targets muscarinic acetylcholine

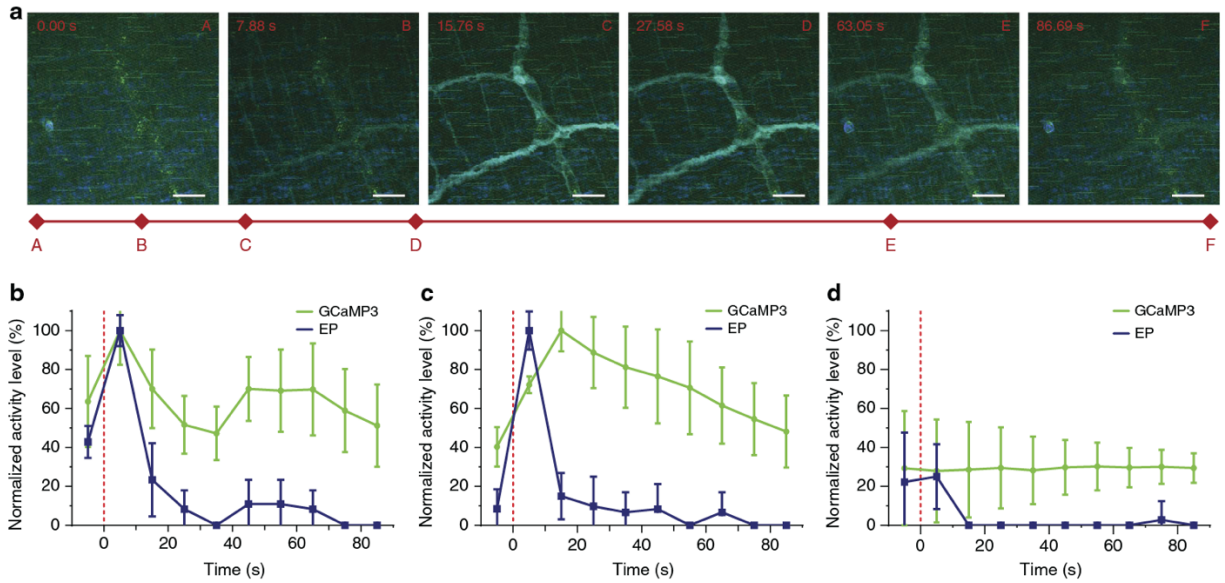

Figure 6.3. Unpaired analysis of fluorescent and electrical potential response to chemical stimuli. (a) Frames from time-lapse recording of GCaMP3-expressing nerves during serotonin stimulation. The activated nerves fluoresce (green) due to stimulation, before fading back to low fluorescence levels. Scale bar, 50 μm. (b–d) Average GCaMP3 fluorescence (green) and average percentage of electrical recording (blue), after (b) acetylcholine, (c) serotonin or (d) PBS stimulations plotted relative to the time of stimulation (n=3 and 5 for GCaMP3 and electrical potential respectively; error bars show standard deviation (s.d.)). Stimulus was applied at time 0 (red dashed line).

receptors, which can increase GI muscular tone and urinary retention [29, 30]. Tegaserod is an agonist for the serotonin receptor 5-HT_4 to stimulate GI motility and peristatic reflexes, which could relieve bloating and constipation associated with irritable bowel syndrome [31]. However, acetylcholine and serotonin also activate other receptors that the drugs do not target (for example, nicotinic acetylcholine receptors). We compared ENS responses with acetylcholine, bethanechol, serotonin and tegaserod, which were delivered via intraperitoneal (IP) injections. Experiments were designed to record 2 min of unperturbed activity before the chemical stimulation and an additional 2 min to observe post-stimulus activity. Compared with the phosphate-buffered saline control, both native transmitters and the drugs were capable of increasing activity in the ENS (Fig. 6.4a–d). The graphene sensor captured detailed waveforms of the activated APs (Fig. 6.4e-h). Quantification of repeated recordings in different mice confirmed an increase in the number of spikes when stimulated by either neurotransmitter or agonist drug (Fig. 6.4i, Supplementary Figs 6.6, 6.7 and Supplementary Table 6.1). Chronic recordings of the same ENS regions over 5 days showed that activities of enteric neurons were either consistently responsive or non-responsive to the serotonin stimuli (Supplementary Fig. 6.8). Application of tetrodotoxin (TTX), which blocks voltage-gated sodium channels, consistently suppressed measured ENS activities *in vivo* (Supplementary Fig. 6.9). 200 ml of 133 μM Tegaserod was also delivered via oral gavage, which was sufficient to stimulate ENS activities (Supplementary Fig. 6.10).

6.1.3.4 ENS activity in response to 470 nm light stimulations

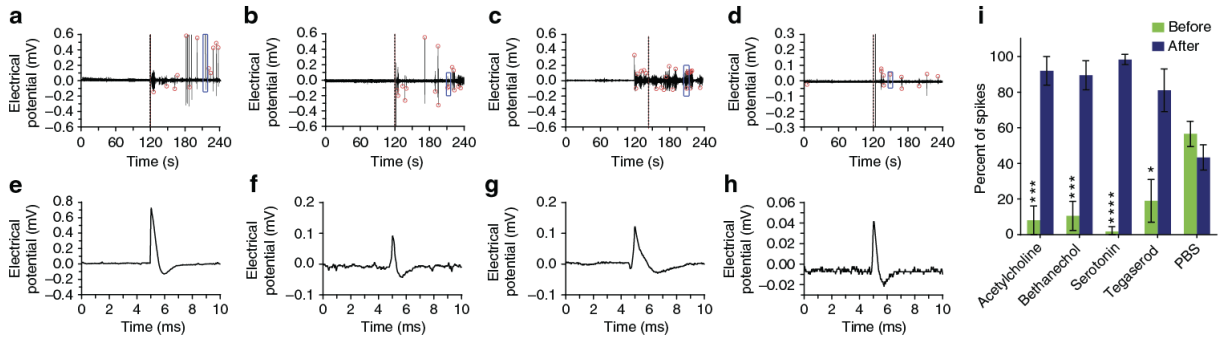

Figure 6.4 Electrical response to chemical stimuli *in vivo*. (a–d) Neural response to *in vivo* stimulation by (a) acetylcholine, (b) bethanechol, (c) serotonin and (d) tegaserod. Stimulus occurs at 120 s (red dashed line), and the electrical potential (black) and spikes (red circles) are plotted over time. (e–h) Waveforms of representative APs from above recordings (blue box) are shown at higher temporal resolution. (i) The effect of chemical stimulation is compared between acetylcholine, bethanechol, serotonin, tegaserod and a PBS control group. The average percentage of spikes that occur before stimulation (green) and the average percentage that occur after (blue) are plotted for each group (n=4; error bars show s.d.). All repeats consisted of recordings lasting 240 s, with stimulation at 120 s. Measurements of individual recordings used to calculate the average percentages are shown in Supplementary Fig. 6.7. *P<0.05; ***P<0.005; ****P<0.001, one sided t-test.

The transparent integrated device also enables us to take advantage of optogenetic technology. In optogenetic mice, light can be applied through the abdominal window and the transparent graphene sensor to stimulate light-gated ion channels, and subsequent ENS responses will be recorded by the graphene sensor.

For proof-of-principle, the device was surgically implanted in *Nos1-creER^{T2}:Chr2* mice. A 470-nm light stimulus was applied onto the small intestine through the abdominal window and transparent graphene sensor (Fig. 6.5a). In these mice, incident 470-nm light opens genetically modified Ca^{2+} channels, activating neuronal nitric oxide synthase (NOS)-positive GABAergic neurons, which produce nitric oxide that acts as a neurotransmitter to affect neurons, the interstitial cells of Cajal and muscle (Fig. 6.5b) [32, 33].

To demonstrate 470 nm light inhibition in the nitrergic neurons in the *NOS1-creER^{T2}:Chr2* animals, recordings were designed to have 5 min of unperturbed activity before a 15-s 470 nm light stimulation, followed by an additional 5 min of recording to observe post-stimulus activity. We found that stimulation at 470nm in Chr2-expressing mice reduced spontaneous activity in naturally active regions of the ENS by 83.66% (Fig. 6.5c, d, Supplementary Fig. 6.11 and Supplementary Table 6.2). In contrast, the same 470-nm incident light stimulation had little effect in wild-type mice, which do not express the genetically modified Ca^{2+} channels. Repeated 470-nm light stimulation ~6 min apart in chronically implanted *Nos1-creER^{T2}:Chr2* mice yielded a decrease in inhibition efficiency, as activities had not fully recovered from the previous stimulation (Supplementary Fig. 6.12). It should be noted that as NOS1-expressing neurons also commonly co-express other neurotransmitters, such as vasoactive intestinal peptide (VIP), further studies are

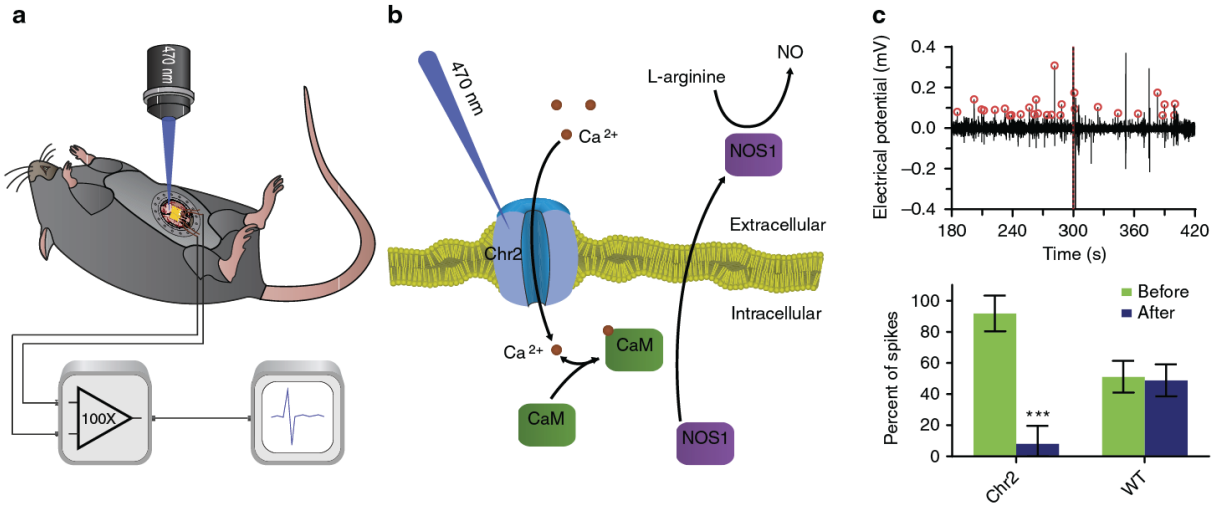

Figure 6.5 Optogenetic application of integrated graphene sensor and abdominal window. (a) A schematic for *in vivo* stimulation of *Nos1-creERT2:Chr2* mice with 470nm light. (b) Mechanistic schematic for 470nm inhibition in *Nos1-creERT2:Chr2* mice. (c) Representative in vivo recording with 470nm stimulation in Chr2-expressing mice. 470nm light stimulation occurs at 300 s (red dashed line). Electrical potential (black) is plotted over time. (d) The effect of in vivo 470nm light stimulation is compared between *Nos1-creERT2:Chr2* mice (Chr2) and wild-type mice (WT). The average percentage of spikes that occur before stimulation (green), and the average percentage that occur after (blue) are plotted for each group (n=4; error bars show s.d.). Only data 120 s before and after stimulation are analysed during repeats. ***P<0.005, one sided t-test.

needed to interpret the physiological basis of these results. Nevertheless, the experiments provide proof of principle for the ability to detect change in ENS activity by targeting specific cell type.

Collectively, we demonstrated simultaneous optical/electrical recording of the ENS in real time by developing an integrated abdominal implant device. The recording can be repeated in live animals carrying this device. Characterization of the ENS response to neurotransmitter/chemical stimuli and optogenetic manipulation was demonstrated. The device has the potential to aid our understanding of the ENS, its role in diseases and its interaction with infection, inflammation, microbiota and the gut–brain axis.

6.1.4 Methods

6.1.4.1 Ethics statement

All animal procedures were reviewed and approved by the Cornell University Institutional Care and Use Committee (protocol no. 2010-0100 and 2015-0029) and were conducted in strict accordance with the recommendations in the Guide for the Care and Use of Laboratory Animals, published by the National Institutes of Health.

6.1.4.2 Animal models

Pirt-GCaMP3 mice were generated previously [26]. The *Wnt1-cre:tdTomato* mice were generated by crossing *Tg(Wnt1-cre)11Rth Tg(Wnt1-GAL4)11Rth/J* (Jackson Laboratory: 003829) with *Ai14* (Jackson Laboratory: 007914). The *Nos1-creERT2:Chr2* mice were generated by crossing *B6:129S-Nos1tm1.1(cre/ERT2)Zjh/J* (Jackson Laboratory: 014541) with *Ai32* (Jackson

Laboratory: 012569). Gene expression was induced in *Nos1-creERT2:Chr2* mice by tamoxifen IP injection at 75 mg kg^{-1} daily for 5 days.

6.1.4.3 Graphene sensor manufacturing

Graphene was grown in a chemical vapor deposition system on copper substrate and transferred using poly(methyl methacrylate) to a quartz substrate [34]. The chip was then patterned with interconnects and a photoresist layer, using standard fabrication techniques at the Cornell NanoScale Science and Technology Facility. Gold interconnects are protected with a layer of photoresist, and they connect exposed contact pads to the exposed graphene electrodes (Supplementary Fig. 6.3a–d). The electrode array (Supplementary Fig. 6.3e) consists of nine graphene electrodes, ranging from 50 μm by 50 μm to 500 μm by 500 μm.

6.1.4.4 Graphene sensor and window integration

Eight via-holes (250 μm diameter) were cut through the borosilicate glass (10 mm diameter) using a laser (VersaLaser VLS3.50). The graphene device was mounted on the glass with transparent epoxy (Hardman Epoxy, 04004). Stranded copper wire (Cooner Wire, CZ1101-A) carry the signal off chip and through via-holes in the window. Copper wire was fixed to gold contact pads using conductive epoxy (MG Chemicals, 83302-21G). Finally, transparent epoxy was used to protect and insulate the copper–gold interface. The transparent epoxy was also used to seal the copper wire in via-holes to maintain separation between the internal and external environments during surgical implantation (Supplementary Fig. 6.4).

6.1.4.5 Recording from the graphene sensor

The electrical potential was recorded by two identical graphene electrodes of the array. From the copper wires, the signal was delivered to a differential AC amplifier (A-M Systems, 1,700) at a 20-kHz sampling rate, where it received a x100 gain and band-pass filter between 300 Hz and 5 kHz. Following amplification, the signal was processed using data acquisition board (NI, BNC-2110) and software (NI, Signal Express).

6.1.4.6 Chronic abdominal window surgery

We used adult mice ranging from 6 to12 weeks of age. Animals were anaesthetized with isoflurane (4% vol/vol induction with 2–3% maintenance) and eye ointment was applied. The abdomen was shaved and cleaned with povidone iodine and ethanol (70% (vol/vol) in water). After a local injection of bupivacaine (0.1% (wt/vol) in saline, 0.1 ml per mouse) and atropine sulfate (0.05 mg kg^{-1}), a circular incision (7 mm) was made into the skin over the mouse abdomen followed by a circular incision (4 mm radius) into the muscle wall, which was prepared inside of skin incision. During all procedures when the mouse was under anaesthesia, body temperature was maintained at 37.5 ºC by a thermostatically regulated heating pad, and 0.1 ml of glucose (5% (wt/vol) in physiological saline) was applied every hour. A sterile, 3D-printed insert was implanted into the surgical site. A portion of the intestine was moved on top of the insert. The insert was fixed in place with sutures attached to the abdominal muscle. The abdominal window was placed over the incision site, and the ring was attached to the surrounding skin by using instant adhesive (Loctite 406). For surgical procedures involving the sensor, the graphene chip had been adhered to the secured coverslip before the procedure. Once the adhesive had been secured, a 20-mm band

of self-adhering vet wrap (3M VetRap) was wrapped around the abdomen to prevent damage to the surgical site while the mouse is awake and to protect the wire connections. After the surgery, the animal was removed from anaesthesia and allowed to recover. Subcutaneous injections of dexamethasone sodium phosphate (0.2 mg kg^{-1}; American Regent, Inc.) and ketoprofen (5 mg kg^{-1}; Fort Dodge) were given every 24 h for 3 days following surgery.

6.1.4.7 *In vivo* multiphoton imaging

In vivo imaging was conducted on a Zeiss LSM880 confocal/multiphoton inverted microscope. Fluorescence emission was collected in two different channels: 505–545 nm wavelengths for FITC and green fluorescent protein detection, and 560–650 nm for tdTomato detection. Green fluorescent protein excitation wavelength was 900 nm, and simultaneous FITC and tdTomato excitation wavelengths were 1,000 nm. Excitation was performed by an InSight DeepSee laser. A x10/0.5 air EC Plan-Neofluar objective was used to visualize the cells in vivo. Mice were anaesthetized with isofluorane (4% (vol/vol) with 2–3% maintenance), and eye ointment was applied. Vet wrap was removed to expose the glass window, and the mice were placed on a 3D-printed imaging stage. To visualize the vasculature, 50 µl of FITC-Dextran dye (Sigma-Aldrich) was injected retro-orbitally. After the imaging was completed, mouse abdomens were rewrapped in fresh vet wrap to prevent scratching. Imaging was performed once every other day to allow the mouse time to recover between imaging sessions.

6.1.4.8 Chronic chemical and 470 nm light stimulations

Post-surgery, mice were anaesthetized with isofluorane (4% vol/vol with 2–3% maintenance), and eye ointment was applied. Vet wrap was removed to expose the graphene sensor and copper wires. The copper wires were connected to the amplifier. Chemical stimulation consisted of IP injection of either 100 μM acetylcholine (Sigma-Aldrich), 100 μM bethanechol (VWR), 10 μM serotonin (Fisher), 133 μM tegaserod (Santa Cruz Biotech), 1 μM Tetrodotoxin citrate (Abcam) or saline (Fisher), in 50 μl quantities. TTX was applied to three mice in a terminal procedure. For the oral drug treatment, mice were given 200 μl of 133 μM tegaserod (Santa Cruz Biotech) via oral gavage. Mice were not exposed to more than four chemical stimulations in a single procedure and stimulation procedures were done at least 2 days apart to allow the mouse to recover. Light stimulations were executed using an AURA light engine at 230 mW. Stimulation consisted of 470 nm light for 15 s through the abdominal window and graphene electrodes. Electrical recording consisted of 2 min of background activity, stimulation, followed by at least 2-min of post-stimulus activity. Oral gavage required a 3-min delay between the pre-stimulus and post-stimulus recording to allow for proper tegaserod administration via oral gavage. After the imaging was completed, mouse abdomens were rewrapped in fresh vet wrap to prevent irritation. Only one electrical recording session was performed every 2 days to allow the mouse torecover between procedures.

6.1.4.9 Statistics

Healthy mice, between 6 and 12 weeks of age, were selected at random for experiments. Each recording session (replicate) was conducted in a new animal each time, except for chronic recording. Recordings were repeated in four different animals for each chemical stimulation

(acetylcholine, bethanechol, serotonin or tegaserod), with a total of 20 recording sessions in distinct animals. Recordings with TTX application were repeated in three different animals. Chronic recordings were compared between responsive and non-responsive animals recorded on days 1, 3 and 5. 470 nm stimulation experiments were repeated in four *NOS1-creER^{T2}:Chr2* mice and four wild-type mice. P-values were determined using paired, one-sided t-tests.

6.1.4.10 Data analysis

Electrical data were analysed in MATLAB to identify spikes. For consistency between recordings, a lower threshold was determined using a minimum signal-to-noise ratio. An upper threshold was also used to filter out artefacts in the signal caused by violent perturbations because of stimulation. The code was not changed between analyses of experiments to maintain consistency and prevent bias. Once spikes had been identified, the effect of each stimulant was determined by calculating the percentage of spikes occurring before and after the stimulus in each recording. For consistency, the time window being analysed before the stimulus is the same length of time being analysed after the stimulus. This time window is at least 2-min for all recordings. Optical data were analysed in ImageJ software. Mean grey value was calculated for regions containing dynamic GCaMP fluorescence. The mean grey value, proportional to the amount of fluorescence, was used to determine the relative activity level during the optical recording.

6.1.4.11 Data availability

The data that support the findings of this study are available from the corresponding author upon request.

6.1.5 Acknowledgements

We thank Dr. Bruce Johnson and Dr. Bruce Land for technical discussion and assistance with the data collection. This work was supported by Award N66001-15-2-4059 from the DARPA Electrical Prescriptions (ElectRx) Program and by NIH R01GM114254. This graphene sensor was manufactured at the Cornell NanoScale Facility, a member of the National Nanotechnology Coordinated Infrastructure (NNCI), which is supported by the National Science Foundation (Grant ECCS-1542081).

6.1.6 Author contributions

N.R., B.B. and X.S. designed the experiments and wrote the manuscript. N.R. and B.B. performed the experiments and analysed the data. J.C., J.J., D.S., Y.-T.C. and N.N. helped design and contributed to the in vivo imaging experiments. N.L.M. and M.S. designed and manufactured the graphene chips. S.K. and P.P. provided transgenic animal models and contributed to imaging the enteric plexus and the optogenetic experiment. C.L. and X.D. provided the GCamp mice and contributed to imaging the action potentials in vivo. Y.C. and E.K. assisted with electrical recording and signal analysis.

6.1.7 Additional information

Supplementary materials are available upon request.

REFERENCES

[1] Gershon, M. D. The enteric nervous system: a second brain. Hosp Pract (1995) 34, 31–32 35-38, 41-32 passim (1999).

[2] Campbell, I. Gut motility and its control. Anaesth. Intensive Care Med. 13, 59–61 (2012).

[3] Matteoli, G. & Boeckxstaens, G. E. The vagal innervation of the gut and immune homeostasis. Gut 62, 1214–1222 (2013).

[4] Bouche, P., Le Forestier, N., Maisonobe, T., Fournier, E. & Willer, J. C. Electrophysiological diagnosis of motor neuron disease and pure motor neuropathy. J. Neurol. 246, 520–525 (1999).

[5] Jones, M. P., Dilley, J. B., Drossman, D. & Crowell, M. D. Brain-gut connections in functional GI disorders: anatomic and physiologic relationships. Neurogastroenterol. Motil. 18, 91–103 (2006).

[6] Grundy, D. et al. Fundamentals of neurogastroenterology: basic science. Gastroenterology 130, 1391–1411 (2006).

[7] Gershon, M. D. & Tack, J. The serotonin signaling system: from basic understanding to drug development for functional GI disorders. Gastroenterology 132, 397–414 (2007).

[8] Digestive Diseases Statistics for the United States Report No. 13-3873 (National Digestive Diseases Information Clearinghouse, National Institutes of Health, Bethesda, MD, 2013).

[9] Mayer, E. A. Gut feelings: the emerging biology of gut-brain communication. Nat. Rev. Neurosci. 12, 453–466 (2011).

[10] Chandrasekharan, B. & Srinivasan, S. Diabetes and the enteric nervous system. Neurogastroenterol. Motil. 19, 951–960 (2007).

[11] Phillips, R. J., Walter, G. C., Wilder, S. L., Baronowsky, E. A. & Powley, T. L. Alpha-synuclein-immunopositive myenteric neurons and vagal preganglionic terminals: autonomic pathway implicated in Parkinson's disease? Neuroscience 153, 733–750 (2008).

[12] Chey, W. D., Kurlander, J. & Eswaran, S. Irritable bowel syndrome: a clinical review. JAMA 313, 949–958 (2015).

[13] Rogler, G. Where are we heading to in pharmacological IBD therapy? Pharmacol Res. 100, 220–227 (2015).

[14] Canales, A. et al. Multifunctional fibers for simultaneous optical, electrical and chemical interrogation of neural circuits in vivo. Nature Biotechnol. 33, 277–284 (2015).

[15] Cianchetti, F. A., Kim, D. H., Dimiduk, S., Nishimura, N. & Schaffer, C. B. Stimulus-evoked calcium transients in somatosensory cortex are temporarily inhibited by a nearby microhemorrhage. PLoS ONE 8, e65663 (2013).

[16] Farrar, M. J. et al. Chronic in vivo imaging in the mouse spinal cord using an implanted chamber. Nat. Methods 9, 297–302 (2012).

[17] Warden, M. R., Cardin, J. A. & Deisseroth, K. Optical neural interfaces. Annu. Rev. Biomed. Eng. 16, 103–129 (2014).

[18] Carson, M. J., Doose, J. M., Melchior, B., Schmid, C. D. & Ploix, C. C. CNS immune privilege: hiding in plain sight. Immunol. Rev. 213, 48–65 (2006).

[19] Khodagholy, D. et al. Highly conformable conducting polymer electrodes for in vivo recordings. Adv. Mater. 23, H268–H272 (2011).
[20] Goto, K. et al. In vivo imaging of enteric neurogenesis in the deep tissue of mouse small intestine. PLoS ONE 8, e54814 (2013).
[21] Ritsma, L. et al. Intestinal crypt homeostasis revealed at single-stem-cell level by in vivo live imaging. Nature 507, 362–365 (2014).
[22] Becker, L., Kulkarni, S., Tiwari, G., Micci, M. A. & Pasricha, P. J. Divergent fate and origin of neurosphere-like bodies from different layers of the gut. Am. J. Physiol. Gastrointest. Liver Physiol. 302, G958–G965 (2012).
[23] Hao, M. M. et al. Early emergence of neural activity in the developing mouse enteric nervous system. J. Neurosci. 31, 15352–15361 (2011).
[24] Stankovich, S. et al. Graphene-based composite materials. Nature 442, 282–286 (2006).
[25] Yang, K., Feng, L., Shi, X. & Liu, Z. Nano-graphene in biomedicine: theranostic applications. Chem. Soc. Rev. 42, 530–547 (2013).
[26] Kim, Y. S. et al. Central terminal sensitization of TRPV1 by descending serotonergic facilitation modulates chronic pain. Neuron 81, 873–887 (2014).
[27] Berger, M., Gray, J. A. & Roth, B. L. The expanded biology of serotonin. Annu. Rev. Med. 60, 355–366 (2009).
[28] Kendig, D. M. & Grider, J. R. Serotonin and colonic motility. Neurogastroenterol. Motil. 27, 899–905 (2015).
[29] Bryant, B. D. & Knights, K. M. Pharmacology for Health Professionals 3rd edn (Elsiever Australia, 2011).
[30] Abrams, P. et al. Muscarinic receptors: their distribution and function in body systems, and the implications for treating overactive bladder. Br. J. Pharmacol. 148, 565–578 (2006).
[31] Camilleri, M. Review article: tegaserod. Aliment Pharmacol. Ther. 15, 277–289 (2001).
[32] Bornstein, J. C., Marks, K. A., Foong, J. P., Gwynne, R. M. & Wang, Z. H. Nitric oxide enhances inhibitory synaptic transmission and neuronal excitability in Guinea-pig submucous plexus. Front. Neurosci. 4, 30 (2010).
[33] Grider, J. R. & Murthy, K. S. Autoinhibition of endothelial nitric oxide synthase (eNOS) in gut smooth muscle by nitric oxide. Regul. Pept. 151, 75–79 (2008).
[34] Mun˜oz, N. Design, Fabrication And Geometric Optimization Of Graphene Electrodes For Electrochemical Detection (Cornell University, 2014).

CHAPTER SEVEN

APPLICATION OF ABDOMINAL IMAGING WINDOW 2: *IN VIVO* IMAGING OF COLORECTAL CANCER

The second example of the use of the abdominal imaging window is in the study of colon cancer. This chapter consists of largely unpublish data, with the exception of some data that went into the supplement of Chen, et al. We demonstrated importance of *in vivo* imaging technology to study tumor growth by showing data in different mouse models of tumors. I also discuss current directions of a tumor study using imaging windows at the end of the chapter.

7.1 Introduction

Tumorigenesis is an extremely complicated process which involves a variety of cell types. In order to understand each step comprehensively, we need a technique to visualize the tumor-microenvironment and to monitor cellular interactions during tumor development. *In vivo* imaging provides novel insight on various questions that cannot be addressed otherwise. For example, we can monitor the moment that tumor cells invade to metastasize, we can capture the interaction of tumor-stromal cells, and we can also investigate roles of immune cells in tumorigenesis. Therefore, using *in vivo* imaging technology which can provide information with high spatial and temporal resolution could be advantageous over or complementary to other methods which only provide information at a fixed time point.

Colorectal cancer (CRC) is a third most common cancer worldwide [1]. CRC has a high survival rate if caught in its early stage. However, the prognosis for 5-year survival rate drops to 10% with detection in the late stage [2]. Therefore, understanding changes in the tumor microenvironment during transitions from primary to metastatic stage is critical [3]. Our collaborator, Dr. Chen from the Shen lab, developed an orthotopic CRC animal model which manipulates the metastatic potential of CRC based on the expression level of chemokine receptor 9 (CCR9) receptor [4]. They found that CCR9 is upregulated in primary tumors from early-stage CRC patients, but downregulated in late-stage CRCs. Sustained expression of the CCR9 gene attracted CRC cells to the colorectum and intestine, while deletion of CCR9 induced aggressive metastasis to liver [4]. The goal of our collaboration was to visualize the different colonization behaviors of CRC cells depending on CCR9 gene expression. Although this work was successful,

we realized that there was a need to improve methods for imaging tumors, leading us to seek new methods for imaging tumor models *in vivo*.

7.2 Results

7.2.1 Chronic abdominal window to capture tumor growth preserve critical elements of tumor microenvironment

Our first studies with the Shen lab used an acute imaging platform, which externalized a portion of intestine and positioned it under the microscope objective (Figure 7.1). We used an orthotopic mouse model in which tumors were seeded by systemic tumor cell injection via the tail vein, which made the use of chronic window impractical since we could not predict the location of tumor formation. Externalizing the intestine allowed us to inspect a large area and made finding the tumor locations possible. We captured images of different colonization of CRC cells in the intestine and the liver, which validated the efficiency of their mouse model. This acute system seemed to work for one-time imaging, but we noticed that there were remarkable structural difference in the intestine between acute and chronic window (Figure 7.2). The vasculature showed increased permeability in the acute method which could cause significant problems for repeated imaging and indicated altered physiology. In order to study changes in tumor microenvironment in early stage of CRC, we needed to adapt the chronic window methods and adjust the tumor model to enable tumor growth in a particular location.

To monitor tumor growth in a primary site without the disruptions caused by externalizing the intestine, we adapted the permanently implanted, abdominal imaging window previously shown in Chapter 4 to the tumor model studies. Switching to the new model had the advantage of

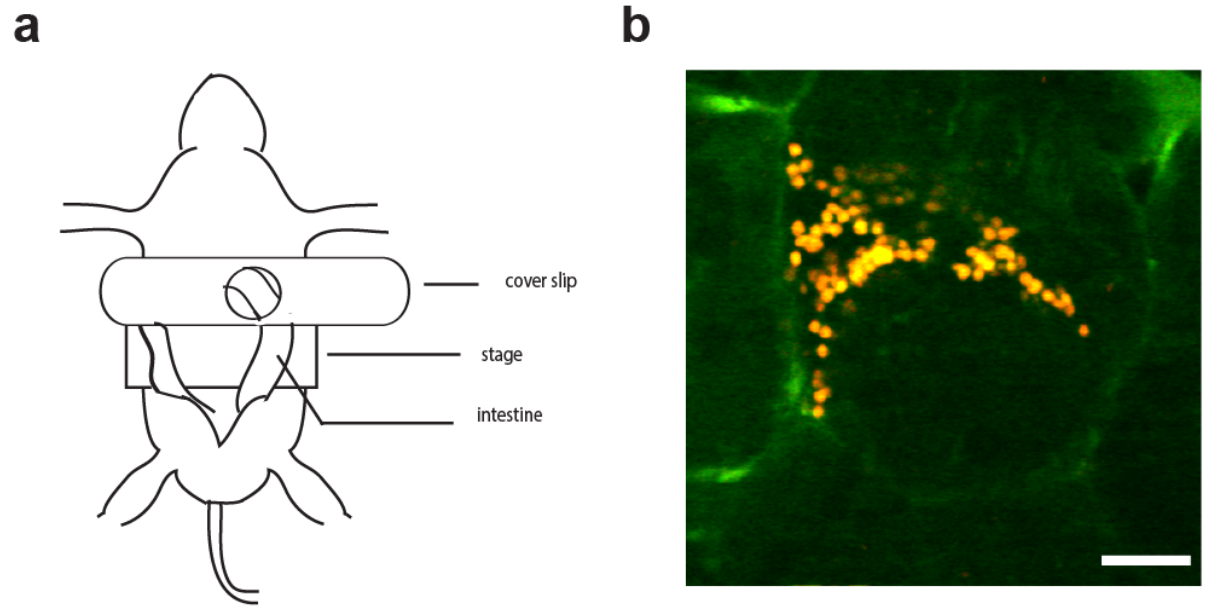

Figure 7.1 Acute imaging platform to visualize CRC *in vivo*. (a) Schematic to describe animal model for *in vivo* imaging with acute setup. A part of the intestine was externalized on to a stage and secured under a cover slip mounted in a frame. (b) CRC cells colonized the intestine. $CCR9^{+}$ RFP CRC cells (red) were captured under two-photon microscopy. FITC-dextran was injected i.v. to label vasculature. Scale bar: 50 μm.

enabling repeated imaging for time-lapse studies, but we needed to develop protocols which enabled successful tumor implantation in a predefined location. There were some challenges in generating a small, localized tumor with direct injection into the window region since inflammation occurred during window implantation and tumor cell injection appeared to prevent solid tumor formation. To overcome these challenges, we tried several different routes to introduce tumor cells. We first implanted tumor cells into an immunocompromised mouse via I.P. injection. To capture early growth of tumor colonies, we implanted the abdominal window a few days after the injection of the tumor cells and imaged it under two-photon microscopy. After 2 weeks from injection, we found several tumor colonies in the small intestine surrounded with vasculature (Figure 7.3).

7.2.2 Cecum injection model with abdominal window

Although I.P. injection model showed promise as a tumor model, it required a long time to form a solid tumor that could be located for imaging. Because the model did not use direct implantation of tumor cells into the tissue, there was also a substantial amount of tumor formation elsewhere which was not desirable. By the time a colony was detectable under two-photon microscopy, the animal's health was often already compromised by the presence of tumors located outside the field of view. We therefore developed another tumor model with direct injection of tumor cells into the cecum wall. Dennis Nyanyo, an undergraduate student who worked with me for four years, performed experiments to develop cecum injection model [5]. To hold the cecum under the window, we modified the 3D-insert from Chapter four by removing the center protrusion (Figure 7.4a). Window implantation and tumor cell injection were performed

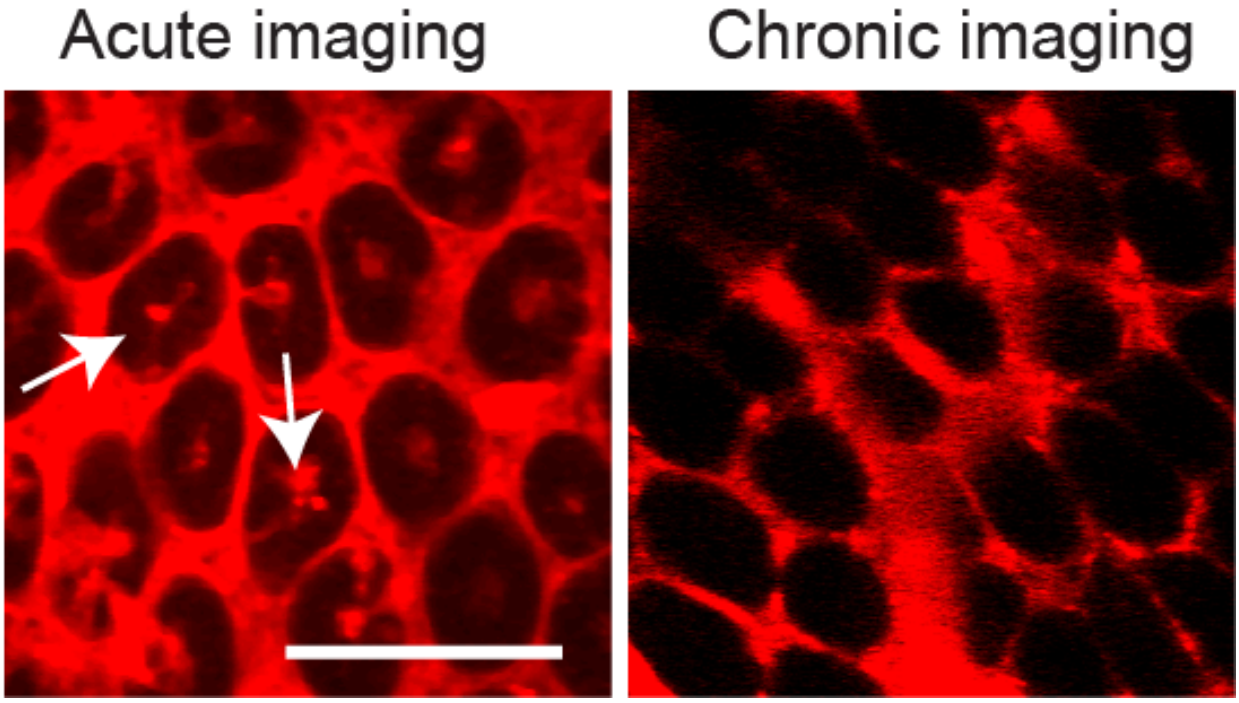

Figure 7.2 Comparison between acute preparation image and chronic window image. With the acute preparation (left), we observed leakage of fluorescent dye into the crypt (white arrows) and extensive dye leaked into the spaces between the crypts. The crypts imaged in a chronic, closed window (right) did not show the same phenomenon. Scale bar: 100 μm

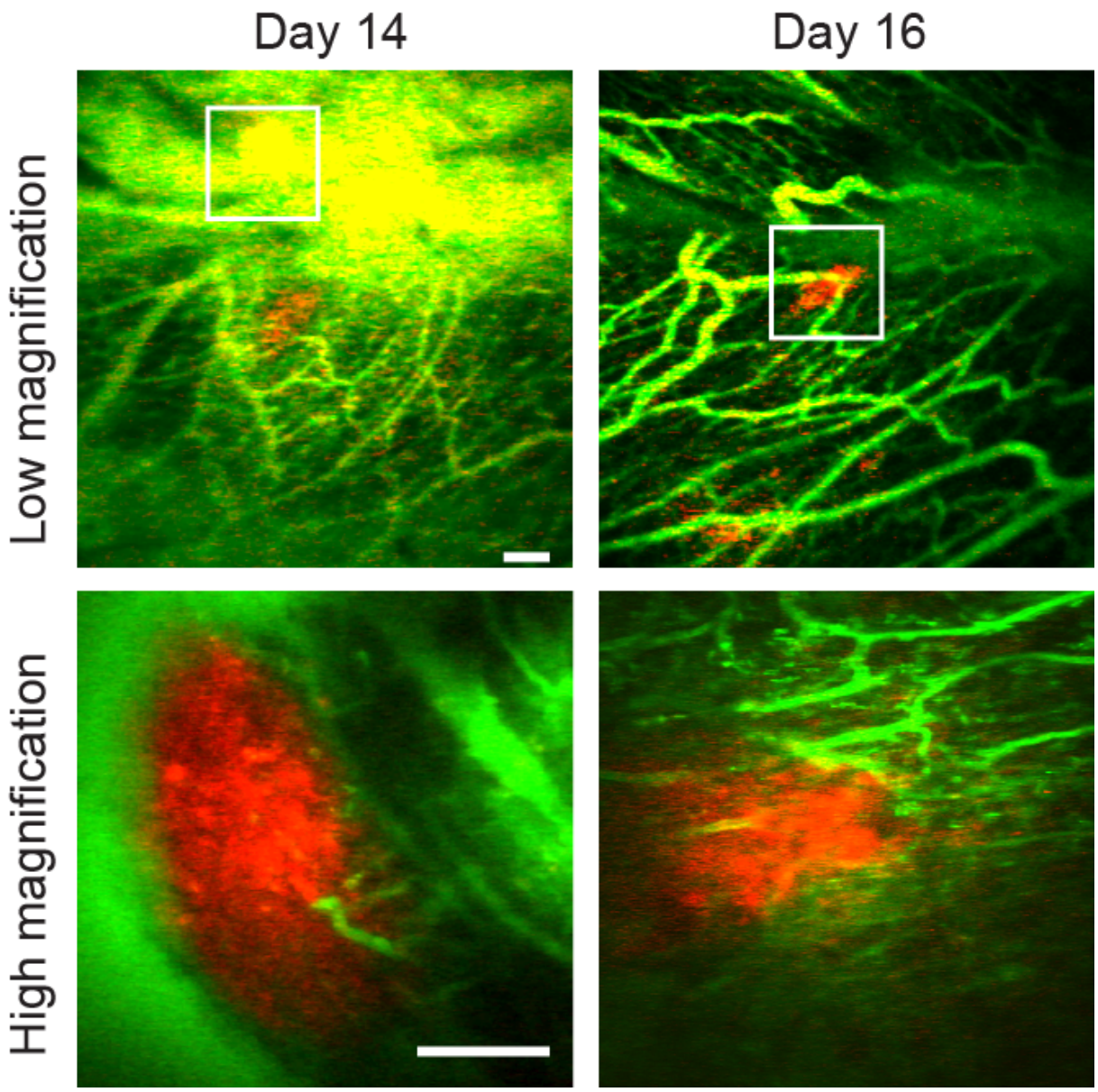

Figure 7.3 Time-lapse images CRC after i.p. injection. Capturing of tumor colonies after injection of CRC. HT116-RFP CRC cells were injected intra peritoneally. FITC-dextran was injected into retro orbital to label vessels. Scale bar: 100 μm.

simultaneously which allowed us to track the location of injection site which was a critical advantage over the other injection model. At 4 days post injection, we found notable changes in vasculature near the tumor injection site, which showed characteristics of tumor vasculature such as increased tortuosity and loss of directionality, while the area away from the injection site still showed normal vasculature (Figure 7.4b). The cecum injection model is a practical model for studying early tumor growth because it significantly reduced time for colonization and the success rate of the combined window and tumor implantation.

After 6 days of tumor injection, we captured images of tumor cells flowing in the blood stream, supposedly circulating tumor cells (CTCs), which showed the possibility that we could capture initiation of tumor metastasis with our tumor model (Figure 7.4c).

7.3 Discussion

We have developed tumor mouse models combined with imaging window for real-time monitoring of tumor growth. Different injection methods changed the dynamics of tumor formation drastically. For example, i.p. injection of tumor cells took about 2 weeks to show a visible tumor mass on average, while cecum injection needed about a week. Early localization of micro-tumors enables us to monitor changes in tumor-microenvironment in early stage of tumor and provides an opportunity to observe initiation of tumor metastasis along with tumor growth. Currently, we are in a process of developing tumor mouse models using immunocompetent mice to investigate interactions between tumor and immune cells more comprehensively. We expect that adding the capability to visualize immune and inflammatory cells within the imaging window

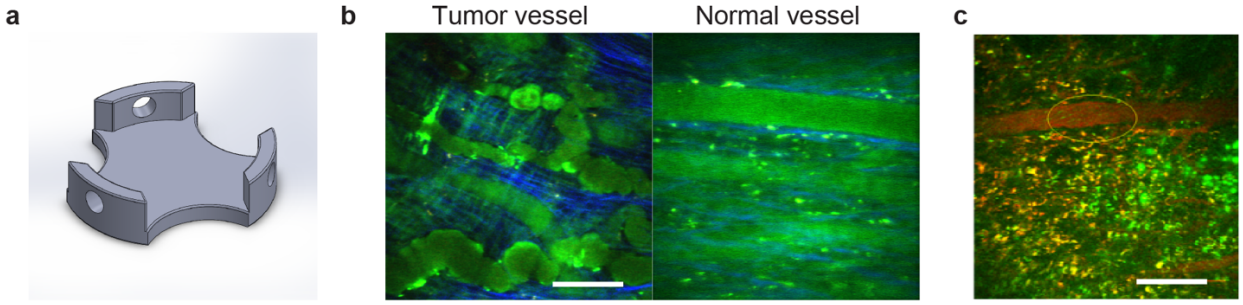

Figure 7.4 *In vivo* images of cecum injection model. (a) 3D-insert modified for tumor model. We edited design of 3D-insert to be used for cecum injection. (b) Vascular changes after tumor injection at the cecum wall. Vessels adjacent to the injection site showed structural changes after 4 days while vessels in the area away from the injection site did not show obvious changes yet. Vessels were visualized with FITC-dextran. (c) Image showing cancer cell shedding into major vein 6 days post injection. SW480 cells expressing GFP were injected into the cecum. Texas Red was injected to image vessels. Yellow circle emphasizes cancer cells intravasated into blood stream. Adapted from reference [5]. Scale bar: 100 μm.

by using transgenic mice that expresses fluorescent reporters in these cells will fill in the details of the tumorigenic and metastatic processes.

There are still challenges that we need to overcome with the tumor window. The biggest problem is that the window becomes cloudy easily due to inflammation. Compared to the normal abdominal window, we saw tumor window showed much faster accumulation of mucus under the glass even in immunocompromised mice. The current procedure is to implant a window and tumor cells at a same time but implanting window a few days after injection may reduce accumulation of mucus and provide a clearer window.

7.4 Methods

7.4.1 Cancer cell culture

SW480-GFP cells and HT116-RFP cells were cultured in RPMI 1640 medium supplemented with 10% fetal bovine serum and 1% Pen-Strep antibiotics. Cells were passaged every 2-3 days at 90% confluency.

7.4.2 Cancer cell injection with window implant

Mice were anesthetized using 4% isoflurane in oxygen and reduced to 2% for duration of surgery. 0.005mg/100g of atropine was injected subcutaneously to prevent fluid build-up in the lungs. 5% glucose solution in saline was injected to prevent dehydration. Abdomen was shaved and wiped with 70% ethanol and betadine solutions respectively. A circular incision was made around the midline of the abdomen to accommodate a titanium window with 12 mm inner diameter. The peritoneal cavity was opened to expose the cecum and the caecum is placed over a custom

insert to hold it in place. The insert is sutured to the skin. 50 µl of tumor cells in PBS is injected into the cecum wall and a glass window is placed over the caecum in the titanium window. An enforcement ring was placed over glass to keep it in place.

7.4.3 Modulation of CCR9 expression in an animal model

Cells were infected with the CCR9-inducible expression lentivirus and followed with blasticidin selection and RFP FACS purification. TetR expression lentivirus in high-titer was then used to infect the inducible CCR9 lines. The CCR9 expression can be induced by 1–2 mg/ml (*in vivo*) doxycycline (Sigma, St Louis, MO) administered in 5% sucrose-containing drinking water. The efficiency of CCR9-inducible expression in these variant colorectal lines was verified by western blotting using anti-human CCR9 antibody (Abcam cat. no. ab38564) or anti-mouse Ccr9 antibody (Thermo Scientific. PA1-21618) and the software of Quantity One (Bio-Rad) was used to semi-quantify protein levels.

7.4.4 *In vivo* imaging with acute imaging preparation

Mice were kept under isoflurane anesthesia and a portion of the large intestine was exter-nalized to be placed in a saline-filled, temperature-controlled chamber. The portion to image was covered with a glass coverslip and agarose for stability and imaged with a custom-built multi-photon microscope optimized for *in vivo* imaging. 50 mg/ml FITC-Dextran (FD2000S; Sigma-Aldrich, St. Louis, MO) was retro-orbitally injected in mice (0.25 ml/kg) and this dose allowed vasculature imaging for 1–2 h. Simultaneous excitation with 900 nm and 1,040 nm femtosecond laser light enabled imaging of GFP (FITC-Dextran) and RFP (human CRC cells) at the same time.

7.4.5 *In vivo* imaging with chronic abdominal window

Animals with abdominal window were imaged using a custom-built 2PEF microscope. All animals were anesthetized with isoflurane (1-2% in medical air) which was adjusted to maintain constant breathing rate during imaging time. To visualize vasculature, 50 µl of 2.5% Texas Red dextran (Molecular weight: 70,000; Thermo Fisher Scientific, NY) in saline was injected retro-orbitally. Images were acquired using a Ti:Sapphire laser (Chameleon; Coherent, Santa Clara, CA) with wavelength centered at 880 nm. A 20x, 1.0-NA (Zeiss, Thornwood, NY) was used for imaging and ablation. A 4X, 0.28-NA objective lens (Zeiss, Thornwood, NY) was used for low-resolution mapping. A 494-nm bandpass filter with 41-nm bandwidth and a 641-nm bandpass filter with a 75-nm bandwidth were used for GFP and RFP respectively.

REFERENCES

[1] M.K. Choong, G. Tsafnat, Genetic and epigenetic biomarkers of colorectal cancer, Clin Gastroenterol Hepatol 10(1) (2012) 9-15.

[2] H. Uchida, K. Yamazaki, M. Fukuma, T. Yamada, T. Hayashida, H. Hasegawa, M. Kitajima, Y. Kitagawa, M. Sakamoto, Overexpression of leucine-rich repeat-containing G protein-coupled receptor 5 in colorectal cancer, Cancer Sci 101(7) (2010) 1731-7.

[3] J. Ferlay, I. Soerjomataram, R. Dikshit, S. Eser, C. Mathers, M. Rebelo, D.M. Parkin, D. Forman, F. Bray, Cancer incidence and mortality worldwide: sources, methods and major patterns in GLOBOCAN 2012, Int J Cancer 136(5) (2015) E359-86.

[4] H.J. Chen, R. Edwards, S. Tucci, P. Bu, J. Milsom, S. Lee, W. Edelmann, Z.H. Gumus, X. Shen, S. Lipkin, Chemokine 25-induced signaling suppresses colon cancer invasion and metastasis, J Clin Invest 122(9) (2012) 3184-96.

[5] Nyanyo, D. Development of methods for in vivo investigation of tumor cells, interactions with innate immune cells and metastasis, BA Thesis. Cornell University 2018.

CHAPTER EIGHT

CONCLUSION AND FUTURE DIRECTION

In this chapter, I will summarize several key findings and technical accomplishments, as well as suggest future research directions. I have presented the abdominal imaging window, and how the use of the window has overcome disadvantages of previous versions, enabling novel time lapse imaging studies of the same region over many days, which have allowed the discovery of a new type of stem cell behavior after small injury.

To address the question of how important the alternating crypt cell pattern is to maintaining homeostasis, we used laser ablation to disrupt niche pattern by inducing the death of a few cells. We found that disruption of the alternating pattern triggered a rapid migration and rearrangement of niche cells at the base of the crypt, which restored the alternating pattern within two hours. In addition, rearrangement of base cells facilitated the removal of cell debris from the crypt base toward the crypt lumen, and removal of cellular debris from the crypt lumen was facilitated by peristaltic motion of cells at upper layer, suggesting that the coordination of these two motions work to recover pattern disruption and the clearance of damage. Peristaltic motion by cells that are not muscle or vascular cells is a novel finding, and the mechanism underlying this motion will need further investigation.

Stem cells must be carefully protected over an organism's entire life. Our finding suggests that stem cells play a specialized and active role in the maintenance of the stem cell niche. Pharmacological inhibition of these specialized cell motions results in incomplete damage

clearance and deficient restoration of the unique alternating pattern. We further demonstrated that the natural process of aging impairs cell motility, thereby contributing to an attenuation of the stem cell niche recovery process. These results indicate that the impaired ability to restore small levels of damage to the stem cell niche can harm epithelial integrity and possibly initiate an inflammatory response. Constant exposure to external pathogens would deteriorate the integrity of the intestinal epithelium, which can initiate pathological conditions. Further investigation into the inflammatory response would help demonstrate whether a small, confined injury is enough to trigger a chronic inflammatory response.

These findings open various opportunities to pursue diverse aspects of the physiology of the small intestine stem cell niche. First, we are examining the interactions between immune cells, particularly resident macrophages, and cells of the crypts during the recovery process. Our preliminary data suggested that macrophages do not play a role in the elimination of damaged cells. Resident macrophages often provide specialized phagocytotic functions, but the intestinal crypt seems to have an alternative defensive mechanism conducted by niche cells rather than recruiting macrophages to eliminate damage.

A mechanistic understanding is needed to fully understand the recovery process of the intestinal stem cell niche. We demonstrated that activation of ROCK protein signaling is required to initiate the recovery process. Inhibition of YAP/TAZ activity by blocking its translocation, caused a similar result achieved with ROCK inhibition, suggesting that YAP/TAZ is a downstream protein of ROCK in modulating the stem cell motility during recovery process. We will continue to work on the pathways involved in the recovery processes. A comprehensive understanding of the recovery process will provide a better perspective on how the integrity of small intestinal

epithelium is maintained and what specific molecule could be a therapeutic target if this process is attenuated.

We introduced a couple examples that have successfully adapted the abdominal window to applications other than the study of stem cells. Chapter six presented the application of the abdominal window to monitor activity of enteric neuron system. In collaborative work with the Shen lab, the abdominal window was combined with a graphene chip that detects electrical signals, demonstrating that the window can be used to record both optical and electrical activities simultaneously. The enteric nervous system has not been studied well *in vivo*, although it plays a fundamental role in gastrointestinal physiology such as digestion of food and communication with the immune system. By applying *in vivo* imaging window to ENS studies, we demonstrated the advantage of using window to study physiology of ENS and suggested possible critical questions that could be addressed with using *in vivo* technology. The abdominal window has also been applied to monitor tumor growth *in vivo* and is described in chapter seven. The existing tumor model were improved by modifying injection routes to allow the observation of the early establishment of tumor mass following cecum injection. Current tumor studies using the abdominal window probe the interactions between cells in the tumor-microenvironment in immunocompetent mice. Figure 7.4 shows robust changes in vasculature a few days after tumor cell injection, which emphasizes that the chronic abdominal window can provide information on early events in tumor microenvironment often missed by older *in vivo* techniques. Furthermore, imaging of circulating tumor cells suggests that our window provides high spatial and temporal resolution at the cellular level to enable study of pathological processes including metastasis. The current aim of our tumor studies is to obtain time lapse imaging over multiple days at the injection

site to observe tumor growth and regression after implantation. The abdominal window has also been adapted to other tumor sites, such as the mammary fat pad to study growth of breast cancer.

This thesis has presented and discussed the advantages of the abdominal imaging window for *in vivo* biological and pathological conditions. By using *in vivo* imaging and manipulation techniques, we demonstrated the ability to discover novel insight into a previously hidden biological process – removal of cell damage within the adult stem cell niche. This further emphasizes the strength of *in vivo* imaging as a tool to understand biological questions, especially for those problems which require a way to monitor the real-time responses at a cellular level. We discovered a novel defensive mechanism in the intestinal crypts that reveals an efficient way to maintain epithelial function after small injuries. Impairment could lead to a pathological condition. Understanding the detailed mechanism of this process will provide insights on how intestinal epithelium maintains homeostasis.